Simplicial vs. Continuum String Theory and Loop Equations¶

E. T. Akhmedov

Institute of Theoretical and Experimental Physics, Moscow, 117218 Russia
Max Planck Institut für Gravitationsphysik, Albert Einstein Institut, 14476 Golm, Germany
e-mail: akhmedov@itep.ru
Received February 2, 2005

We derive loop equations in a scalar matrix field theory. We discuss their solutions in terms of simplicial string theory—the theory describing embeddings of two-dimensional simplicial complexes into the spacetime of the matrix field theory. This relation between the loop equations and the simplicial string theory gives further arguments that favor one of the statements of the paper hep-th/0407018. The statement is that there is an equivalence between the partition function of the simplicial string theory and the functional integral in a continuum string theory—the theory describing embeddings of smooth two-dimensional world-sheets into the spacetime of the matrix field theory in question. © 2005 Pleiades Publishing, Inc.

PACS numbers: 11.10.–z, 11.15.Bt, 11.25.Tq

1. In this short note we give further arguments supporting the observations made in [1]. Here, we consider matrix scalar field theory in the D-dimensional Euclidian space:

$$Z = \int D\hat{\Phi}(x) D\hat{\bar{\Phi}}(x) \exp\left\{-\int d^D x N \mathrm{Tr}\left[\frac{1}{2}|\partial_\mu \hat{\Phi}|^2\right.\right.$$

$$\left.\left. + \frac{m^2}{2}|\hat{\Phi}|^2 + \frac{\lambda}{3}\hat{\Phi}^3 + \text{c.c.}\right]\right\}, \tag{1}$$

where $\mu = 1, \ldots, D$, and $\hat{\Phi}$ is an $N \times N$ matrix field in the adjoint representation of $U(N)$ group: Φ^{ij}, $i, j = 1, \ldots, N$. We choose this theory due to its simplicity (for our purposes) in comparison with gauge and matrix theories with more involved potentials. The problems of this theory due to the sign indefiniteness of its potential are irrelevant for our considerations: we consider this functional integral as a formal series expansion over λ. All our considerations can be easily generalized to the other matrix scalar and gauge theories. In fact, one can always make a theory with cubic interactions out of a theory with more involved interactions via insertions of integrations over additional fields into the functional integral.

The functional integral (1) can be transformed into the summation over the closed two-dimensional simplicial complexes[1] [1]:

$$\log Z = \sum_{g=0}^{\infty} N^{\chi(g)} \sum_{V=0}^{\infty} \lambda^V \sum_{\text{graph; V, g fixed}} C'_{\text{graph}}(V, g)$$

$$\times \left|\int_0^{+\infty} \prod_{n=1}^{L} \frac{d\alpha_n}{\alpha_n^{gD}} e^{-\frac{\alpha_n m^2}{2}} \int \prod_{a=1}^{F} d^D \mathbf{x}_a \right. \tag{2}$$

$$\times \left. \exp\left\{-\sum_{l=1}^{L} \frac{\alpha_l}{2}(\Delta_l \mathbf{x})^2\right\}\right|_{\text{graph}},$$

where $C'_{\text{graph}}(V, g)$ are some combinatoric constants defined in [1], F is the number of faces of the fat Feynman graph, L is the number of links, V is the number of vertices, and g is the genus of the Feynman diagram.

The summation in Eq. (2) is taken over the graphs that are dual to the Feynman diagrams [1]. These graphs represent triangulations of Riemann surfaces. In [1], we interpret the expression (2) as the partition function of the closed simplicial string theory—the theory describing embeddings of two-dimensional simplicial complexes into the spacetime of the matrix field theory. In the context, α values are related to the components of the two-dimensional metric [1].

Furthermore, in [1], we argue that there is no need to take a continuum limit in Eq. (2): there should be a continuum string theory[2] whose functional integral is equal to Eq. (2). In this paper, we give further arguments supporting this idea. We propose equations that are solved via the simplicial open string theory "functional integral." On the other hand, these equations have

---

¶ This article was submitted by the author in English.

[1] A similar transformation was performed in [2] to establish a relation between the no-gravity limit of the Ponzano–Regge theory and a noncommutative field theory.

[2] It is a theory describing embeddings of the smooth two-dimensional world-sheets into the spacetime of the matrix field theory in question.

a natural interpretation as constraint equations in a two-dimensional field theory containing gravity.

To present the idea of our argument, let us consider the case of the relativistic particle. The path integral for the latter solves the following equation [3]:

$$(-\Delta + m^2)G(\mathbf{x}, \mathbf{x}') = \delta(\mathbf{x} - \mathbf{x}'). \tag{3}$$

One can also obtain a simplicial integral solution to this equation [1] as follows. The solution of Eq. (3) can be represented as

$$G(\mathbf{x}, \mathbf{x}') = \int d^D \mathbf{p} e^{i\mathbf{p}(\mathbf{x}-\mathbf{x}')} \frac{1}{\mathbf{p}^2 + m^2}$$

$$= \frac{1}{\Lambda} \int d^D \mathbf{p} e^{i\mathbf{p}(\mathbf{x}-\mathbf{x}')} e^{-\log \frac{\mathbf{p}^2 + m^2}{\Lambda}}$$

$$= \frac{1}{\Lambda} \sum_{L=0}^{\infty} \frac{(-1)^L}{L!} \int d^D \mathbf{p} e^{i\mathbf{p}(\mathbf{x}-\mathbf{x}')} \left[\log \frac{\mathbf{p}^2 + m^2}{\Lambda} \right]^L \tag{4}$$

$$= \frac{1}{\Lambda} \sum_{L=0}^{\infty} \frac{(-1)^L}{L!} \int d^D \mathbf{p} e^{i\mathbf{p}(\mathbf{x}-\mathbf{x}')}$$

$$\times \prod_{l=1}^{L} \int_0^{+\infty} \frac{de_l}{e_l} \left(e^{-\frac{\mathbf{p}^2 + m^2}{2} e_l} - e^{-\frac{\Lambda}{2} e_l} \right),$$

where Λ is the cutoff. If we drop all the terms containing $\exp\{-\Lambda e/2\}$ in Eq. (4), we obtain the divergent expression, which can be represented in the following form [1]:

$$G_{\mathrm{div}}(\mathbf{x}, \mathbf{x}') \propto \sum_{L=0}^{\infty} \frac{(-1)^L C_L}{L!} \int_0^{+\infty} \prod_{n=1}^{L} \frac{de_n}{e_n^{D/2+1}}$$

$$\times \int \prod_{i=1}^{L} d^D \mathbf{y}_i \exp\left\{ -\frac{1}{2} \sum_{l=0}^{L} \left[\frac{(\Delta_l \mathbf{y})^2}{e_l} + m^2 e_l \right] \right\}. \tag{5}$$

In each member of the sum, here $\mathbf{y}_0 = \mathbf{x}$, $\mathbf{y}_{L+1} = \mathbf{x}'$, and C_L are easily computable constants dependent on L.

The formula (5) contains the summation over the one-dimensional geometries. In fact, it contains the summation over all discretizations/triangulations (L) of the world trajectory and the integration over all one-dimensional distances (e's) between the vertices (y's). The summation over the embeddings of the simplicial complexes is represented by the summation over the number of vertices (L) and the integration over all their possible positions, i.e., over y's.

Thus, Eq. (5) is, so to say, a simplicial particle theory "path integral" which formally solves Eq. (3) but demands a regularization. At the same time, Eq. (4) suggests a natural regularization of the simplicial partition function (5) and rigorously relates it to the differential Eq. (3).

Moreover, as we see, one does not have to take a continuum limit in Eq. (5) and this "simplicial path integral" after the regularization is equivalent to the regularized standard path integral for the relativistic particle.

Below, we argue that the same thing should happen in the case of simplicial string theory and, possibly, for the higher dimensional simplicial brane theories. To obtain a proper theory of the latter kind, one should both sum over the (multidimensional) triangulations and integrate over the sizes of the links. This procedure gives the summation over all the internal geometries, which in usual functional integrals is represented by the integration over all metrics divided by the volume of the group of diffeomorphisms.

2. Once the relation between Eq. (1) and Eq. (2) is established, one of the natural generalizations of Eq. (3) to two dimensions can be represented by the loop equations [4] in the matrix field theory. In this section, we derive the loop equations for the theory (1) and discuss their obvious solution in terms of the simplicial open string theory. Such a string theory follows from the expansion in Feynman diagrams of an analog of Wilson's loop correlation function [1]. As we will see, these loop equations have a natural interpretation as constrained equations on the functional integral for a continuum string theory. Obviously, the latter should be equivalent to the simplicial string theory partition function in the same way as in the case of the relativistic particle.

Thus, we would like to consider Ward type identities for the correlation function of the Wilson loop operator:

$$W(C) = \mathrm{TrP}\exp\left\{ -\oint_C ds \sqrt{\dot{\mathbf{x}}^2(s)} \hat{\Phi}[x(s)] \right\}, \tag{6}$$

where C is a loop in the spacetime, which is represented by the map $x(s)$. However, one can obtain closed[3] loop equations for such an operator only in the theory with the Lagrangian [5]

$$L = \frac{1}{2}\mathrm{Tr}\left| \partial_\mu \hat{\Phi} \right|^2 \tag{7}$$

or with the Lagrangians following from the reduction of the Yang–Mills theory. To obtain closed loop equations for the theory (1), we suggest considering the loop operator as follows

$$W(C, e) = \mathrm{TrP}\exp\left\{ -\oint_C ds e(s) \hat{\Phi}[x(s)] \right\}. \tag{8}$$

As well, there is the operator $\overline{W}(C, e)$ which depends on $\overline{\Phi}$ and the same e—the real-valued square root of the one-dimensional internal metric on the interval of s.

---

[3] Means equations, which include no other kinds of operators except the loop ones.

Let us define the loop space Laplace operator as in [3]:

$$\frac{\partial^2}{\partial x^2(s)} = \int\limits_{s-0}^{s+0} ds' \frac{\delta^2}{\delta x_\mu(s)\delta x_\mu(s')}. \qquad (9)$$

Then, it is straightforward to see that [3, 4] leads to the following:

$$\left(-\frac{\partial^2}{\partial x^2(s)} + m^2 e(s)\frac{\partial}{\partial e(s)}\right)W(C, e)$$

$$+ \lambda e(s)\frac{\partial^2}{\partial e^2(s)}\overline{W}(C, e)$$

$$= e(s)\mathrm{TrP}\left\{(-\partial_\mu^2\hat{\Phi} + m^2\hat{\Phi} + \lambda\hat{\overline{\Phi}}^2)\right.$$

$$\left.\times \exp\left\{-\oint\limits_C ds e(s)\hat{\Phi}[x(s)]\right\}\right\}. \qquad (10)$$

Similarly one has the complex conjugate equation. To find the right hand side of this expression (after the averaging over all the field configurations), let us consider the equality[4]

$$0 = \int D\hat{\Phi}(x)D\hat{\overline{\Phi}}(x)\frac{\delta}{\delta\overline{\Phi}^a}$$

$$\times \left(\exp\left\{-\int d^D x N \mathrm{Tr}\left[\frac{1}{2}|\partial_\mu\hat{\Phi}|^2\right.\right.\right.$$

$$\left.\left.+ \frac{m^2}{2}|\hat{\Phi}|^2 + \frac{\lambda}{3}\hat{\Phi}^3 + \mathrm{c.c.}\right]\right\} \qquad (11)$$

$$\left.\times \mathrm{TrP}\exp\left\{-\oint\limits_C ds e(s)\hat{\overline{\Phi}}[x(s)]\right\}\right).$$

From this we obtain

$$\left\langle (-\partial_y^2\Phi^a(y) + m^2\Phi^a(y) + \lambda[\overline{\Phi}^2]^a(y))\right.$$

$$\left.\times \exp\left\{-\oint\limits_C ds e(s)\hat{\Phi}[x(s)]\right\}\right\rangle$$

$$= -\left\langle\oint ds e(s)\delta[y - x(s)]P\right. \qquad (12)$$

^{4} Here $\hat{\Phi} = \Phi^a T^a$ and T^a, $a = 1, ..., N^2$ are the generators of $U(N)$.

$$\times \exp\left\{-\int\limits_x^y dt e(t)\hat{\overline{\Phi}}[x(t)]\right\}T^a$$

$$\left.\times \exp\left\{-\int\limits_y^x dt e(t)\hat{\overline{\Phi}}[x(t)]\right\}\right\rangle.$$

Here, the left hand side appears from the variation over $\overline{\Phi}^a$ of the exponent of the action and the right hand side appears from the variation of $\overline{W}(C, e)$.

Hence, we obtain

$$\left(-\frac{1}{e(s)}\frac{\partial^2}{\partial x^2(s)} + m^2\frac{\partial}{\partial e(s)}\right)\langle W(C, e)\rangle$$

$$+ \lambda\frac{\partial^2}{\partial e^2(s)}\langle\overline{W}(C, e)\rangle$$

$$= \oint ds' e(s')\delta[x(s) - x(s')] \qquad (13)$$

$$\times \langle\overline{W}(C_{xx'}, e)\overline{W}(C_{x'x}, e)\rangle$$

and the complex conjugate equation. In Eq. (13), we use

$$\sum_a T_{ij}^a T_{mn}^a = \delta_{in}\delta_{jm} \qquad (14)$$

and $C_{x'x'}^{xx} = C_{x'x} \cup C_{xx'}$. The right hand side of Eq. (13) does not vanish if the contour $C_{x'x'}^{xx}$ (which is just C with two designated points $x = x(s)$ and $x' = x(s')$) has self-intersection at $x = x'$ [3, 4].

The solution of Eq. (13) via the expansion in powers of λ of the correlation function $\langle W(C, e)\rangle$ looks as follows:

$$\log\langle W(C, e)\rangle$$

$$= \sum_{E=2}^\infty \int\limits_0^{2\pi} ds_1 e(s_1)... \int\limits_0^{s_{E-1}} ds_E e(s_E)$$

$$\times \sum_{g=0}^\infty N^{\chi(g)}\sum_{V=0}^\infty \lambda^V \sum_{\text{graph; } V, g, E \text{ fixed}} C_{\text{graph}}(E, V, g) \qquad (15)$$

$$\times \left|\int\limits_0^{+\infty}\prod_{n=1}^L d\alpha_n\int\prod_{i=1}^V d^D\mathbf{y}_i\int\prod_{m=1}^L d^D\mathbf{p}_m\right.$$

$$\left.\times \exp\left\{-\sum_{l=1}^L\left[\frac{\alpha_l(\mathbf{p}_l^2 + m^2)}{2} - i\mathbf{p}_l(\Delta_l\mathbf{y})\right]\right\}\right|_{\text{graph}},$$

where $C_{\text{graph}}(E, V, g)$ are some combinatoric constants, and, in the exponent on the right hand side among the y's, there are $y(s_1), ..., y(s_E)$ over which the integration

is not taken and they are sitting on the contour C. The first sum on the right hand side is taken over their number. The summation over the "graph" in Eq. (15) means the summation over the Feynman diagram contributions to the correlation function in question. Accordingly, V is the number of interaction vertices, L is the number of propagators, y's are positions of the vertices, p's are momenta running over the propagators, α's are Schwinger parameters, and g is the genus of the fat Feynman diagram.

Performing the transformation of [1], we obtain

$$
\begin{aligned}
\log\langle W(C,e)\rangle &= \sum_{E=2}^{\infty} \int_0^{2\pi} ds_1 e(s_1) \dots \int_0^{s_{E-1}} ds_E e(s_E) \\
&\times \sum_{g=0}^{\infty} N^{\chi(g)} \sum_{V=0}^{\infty} \lambda^V \sum_{\text{graph; } V,\,g,\,E\text{ fixed}} C'_{\text{graph}}(E,V,g) \\
&\times \left| \int_0^{+\infty} \prod_{n=1}^{L} \frac{d\alpha_n}{\alpha_n^{(2g+1)D/2}} e^{-\frac{m^2\alpha_n}{2}} \int \prod_{a=1}^{F} d^D\mathbf{x}_a \right. \qquad (16) \\
&\times \exp\left\{ -\sum_{l=1}^{L} \frac{\alpha_l}{2}(\Delta_l\mathbf{x})^2 - \sum_{f=1}^{E} \frac{\mathbf{y}^2(s_f)}{2} \right. \\
&\left.\left. \times \sum_{s,s'=1}^{2g+1} \omega_f^{(s)} \frac{1}{\displaystyle\sum_{l=1}^{L} \alpha_l \omega_l^{(s)} \omega_l^{(s')}} \omega_f^{(s')} + \mathbf{i}\sum_{f=1}^{E} \Delta_f \mathbf{x}\mathbf{y}(s_f) \right\} \right|_{\text{graph}} .
\end{aligned}
$$

Here, $\omega_l^{(s)}$, $s = 1, \dots, 2g+1$ are the values on the lth link of the closed (but not exact) one forms on the genus g simplicial complex with one boundary. These simplicial complexes are defined by the dual graphs to the Feynman diagrams. Now, the sum in Eq. (16) is taken over these dual graphs rather than the Feynman diagrams themselves. C'_{graph} is different from C_{graph} by a factor of the determinant of some matrix [1].

The main difference between Eq. (13) and Eq. (3) is that the former one is a nonlinear equation. However, dropping the right hand side of Eq. (13) (and putting the functional δ function instead), we obtain the standard linear Wheeler–DeWitt equation in a two-dimensional gravity theory coupled to the matter fields (x). Both loop and Wheeler–DeWitt equations are not well defined due to their divergences [3]. As a result, the solution of such equations in terms of a two-dimensional functional integral is not known.

Note that the UV divergences of the quantum field theory in Eq. (1) acquires a clear interpretation in the simplicial string theory description (16). These divergences are just due to the boundaries in the space of all

metrics, i.e., when some of the α values vanish, which corresponds to the situations in which some of the triangles in the dual graph to the Feynman diagram degenerate into links [1]. The natural regularization of Eq. (16) is analogous to the one presented in Eq. (4) for the case of particles. It is nothing but the regularization that follows from the insertion of the integration over the ghost Pauli–Villars fields into the functional integral of the matrix field theory. The addition of these fields sets an obvious regularization of the loop equations, but one needs a renormalized version of these equations rather than just their regularization [3]. This is a subject for another work (see [6] for the attempts at understanding this point).

3. We have considered nonstandard loop variables in the scalar matrix field theory. These loop variables depend on both loops in the target space and internal one-dimensional metrics and obey loop equations. The equations represent a nonlinear generalization of the Wheeler–DeWitt equations in a two-dimensional gravity theory interacting with matter. There is an obvious solution to these equations in terms of the partition function of an open simplicial string theory. We argue that there should be a continuum string theory solution to the same equations, which is exactly equivalent to the simplicial one. The only obstacle which can appear in formulating such a continuum string theory is that, for generic values of λ, it can happen that its functional integral will contain an integration measure for the metrics, which does not follow from a local norm.

REFERENCES

1. E. T. Akhmedov, Pis'ma Zh. Éksp. Teor. Fiz. **80**, 247 (2004) [JETP Lett. **80**, 218 (2004)]; hep-th/0407018.
2. L. Freidel and E. R. Livine, hep-th/0502106.
3. A. M. Polyakov, *Gauge Fields and Strings* (Harwood Academic, Chur, Switzerland, 1987).
4. Y. Makeenko and A. A. Migdal, Nucl. Phys. B **188**, 269 (1981); Sov. J. Nucl. Phys. **32**, 431 (1980).
5. Y. M. Makeenko, Phys. Lett. B **212**, 221 (1988).
6. E. T. Akhmedov, Phys. Lett. B **442**, 152 (1998); hep-th/9806217; hep-th/0202055.

Hunting for the Alpha: $B \to \rho\rho, B \to \pi\pi, B \to \pi\rho$¶

G. G. Ovanesyan[1] and M. I. Vysotsky[2]

[1] Institute of Physics and Technologies, Moscow, 141700 Russia
e-mail: ovanesyn@itep.ru
[2] Institute of Theoretical and Experimental Physics, Moscow, 117218 Russia
e-mail: vysotsky@itep.ru
Received March 11, 2005

The hypothesis of the smallness of penguin contributions to charmless strangeless $B_d(\bar{B}_d)$ decays allows one to determine with high accuracy the value of the angle α from the currently available $B \to \rho\rho, B \to \pi\pi$, and $B \to \pi\rho$ decay data. © 2005 Pleiades Publishing, Inc.

PACS numbers: 12.15.Hh, 13.25.Hw

1. Introduction. Measurement of CP asymmetries in $B_d(\bar{B}_d) \to J/\psi K^0$ decays by BaBar and Belle collaborations determines the angle β of CKM unitarity triangles with high accuracy [1]:

$$\sin 2\beta = 0.724 \pm 0.040, \quad \beta = 23° \pm 2°. \quad (1)$$

The next task is to measure the angles α and γ with comparable accuracy in order to determine if New Physics contributes to CP violation in B decays. For precise determination of the value of the angle γ, one should study B_s decays and this should wait until the LHC(b) era. The purpose of this Letter is to stress that (maybe) angle α is already known with an accuracy comparable to that achieved in β.

2. $B \to \rho\rho$. Let us start from $B_d(\bar{B}_d) \to \rho\rho$ decays, where the smallness of the QCD penguin contribution directly follows from the experimental data on the relative smallness of the branching ratio of $B_d(\bar{B}_d) \to \rho^0\rho^0$ decays [2]. Here are the experimental data; all the branchings are in units of 10^{-6}

$$Br(\rho^+\rho^-) \equiv B_{+-} = 30 \pm 5 \pm 4 \quad [3],$$

$$Br(\rho^\pm\rho^0) \equiv B_{\pm 0} = 22.5 \pm 5 \pm 6 \quad [4],$$
$$Br(\rho^\pm\rho^0) \equiv B_{\pm 0} = 31.7 \pm 7 \pm 5 \quad [5], \quad (2)$$

$$Br(\rho^0\rho^0) \equiv B_{00} < 1.1 (90\% \text{ C.L.}) \quad [6].$$

In order to prove the smallness of the penguin contribution, let us write the amplitudes of $B_d(\bar{B}_d) \to$ $\rho^0\rho^0$ decays as the sum of tree and penguin contributions:

$$A_{\rho^0\rho^0} = T_{\rho^0\rho^0} e^{i\gamma} + P_{\rho^0\rho^0} e^{i\delta_{00}},$$
$$\bar{A}_{\rho^0\rho^0} = T_{\rho^0\rho^0} e^{-i\gamma} + P_{\rho^0\rho^0} e^{i\delta_{00}}, \quad (3)$$

where γ is the angle of a unitarity triangle and δ_{00} is the difference of phases of the final state strong interaction amplitudes induced by the penguin and tree quark diagrams. (We use the so-called c convention in defining the penguin amplitude: a penguin with an intermediate t quark is subtracted, while a penguin with an intermediate u quark is included into the tree amplitude.)

For widths we obtain:

$$\Gamma_{\rho^0\rho^0} = T_{\rho^0\rho^0}^2 + P_{\rho^0\rho^0}^2 + 2T_{\rho^0\rho^0}P_{\rho^0\rho^0}\cos(\delta_{00} - \gamma),$$
$$\bar{\Gamma}_{\rho^0\rho^0} = T_{\rho^0\rho^0}^2 + P_{\rho^0\rho^0}^2 + 2T_{\rho^0\rho^0}P_{\rho^0\rho^0}\cos(\delta_{00} + \gamma), \quad (4)$$

and

$$\frac{1}{2}(\Gamma_{\rho^0\rho^0} + \bar{\Gamma}_{\rho^0\rho^0}) = T_{\rho^0\rho^0}^2 + P_{\rho^0\rho^0}^2$$
$$+ 2T_{\rho^0\rho^0}P_{\rho^0\rho^0}\cos\gamma\cos\delta_{00} \geq P_{\rho^0\rho^0}^2(1 - \cos^2\gamma). \quad (5)$$

Since, from the global fit of CKM matrix parameters, we know that $\gamma \geq 45°$ [7–9], one observes that the compensation of $P_{\rho^0\rho^0}$ by $T_{\rho^0\rho^0}$ is not possible and both of them are small in comparison with the amplitudes of B decays into $\rho^\pm\rho^0$, $\rho^+\rho^-$-states.

Two ρ-mesons produced in B-decays should be in $I = 0$ or $I = 2$ states, and, since the QCD penguin amplitude has $\Delta I = 1/2$, it contributes only to the $I = 0$ state. That is why $P_{\rho^\pm\rho^0} = 0$, while $P_{\rho^+\rho^-} = \sqrt{2} P_{\rho^0\rho^0} \ll T_{\rho^+\rho^-}$. The tree level $b \to u\bar{u}d$ amplitude having both $\Delta I =$

¶ This article was submitted by the authors in English.

1/2 and $\Delta I = 3/2$ parts produces both $I = 0$ and $I = 2$ states of two ρ-mesons, and one can easily organize compensation of these two amplitudes in $B_d(\bar{B}_d) \longrightarrow \rho^0\rho^0$ decays that still satisfactorily describe the $B_d(\bar{B}_d) \longrightarrow \rho^+\rho^-$ and $B_u(\bar{B}_u) \longrightarrow \rho^\pm\rho^0$ branching ratios.

Let us show how it works:

$$T_{\rho^0\rho^0} = \frac{1}{\sqrt{6}}A_0 - \frac{1}{\sqrt{3}}A_2 e^{i\delta}, \qquad (6)$$

where δ is the difference of the phases of the final state interaction (FSI) amplitudes of the ρ-mesons in $I = 2$ and $I = 0$ states, and, in order for these two terms to compensate for each other, δ should be small. Let us suppose that $\delta = 0$, so that we can write:

$$\frac{1}{\sqrt{6}}A_0 = \frac{1}{\sqrt{3}}A_2 \pm \sqrt{B_{00}}. \qquad (7)$$

We should extract the value of A_2 from the $B_u(\bar{B}_u) \longrightarrow \rho^\pm\rho^0$ decay branching ratio:

$$T_{\rho^\pm\rho^0} = \frac{\sqrt{3}}{2}A_2, \quad A_2 = \frac{2}{\sqrt{3}}\sqrt{B_{\pm0}k}, \qquad (8)$$

where $k = \tau_{B^0}/\tau_{B^+} = 0.92$.

Finally we get:

$$T_{\rho^+\rho^-} = \frac{1}{\sqrt{3}}A_0 + \frac{1}{\sqrt{6}}A_2$$

$$= \sqrt{\frac{2}{3}}A_2 \pm \sqrt{2B_{00}} + \frac{1}{\sqrt{6}}A_2 = \sqrt{2B_{\pm0}k} \pm \sqrt{2B_{00}}, \qquad (9)$$

and, choosing a negative sign and the upper experimental bound on B_{00} as well as an average experimental result for $B_{\pm0}$, we obtain for $Br(\rho^+\rho^-)$ the result which coincides with the central value from (2).

Turning to our main subject—determination of the value of the angle alpha—we should look at CP asymmetries measured in $B_d(\bar{B}_d) \longrightarrow \rho^+\rho^-$ decays:[1]

$$\frac{\dfrac{dN(\bar{B}_d^0 \longrightarrow \rho^+\rho^-)}{dt} - \dfrac{dN(B_d^0 \longrightarrow \rho^+\rho^-)}{dt}}{\dfrac{dN(\bar{B}_d^0 \longrightarrow \rho^+\rho^-)}{dt} + \dfrac{dN(B_d^0 \longrightarrow \rho^+\rho^-)}{dt}} \qquad (10)$$

$$= -C_{\rho\rho}\cos(\Delta m \Delta t) + S_{\rho\rho}\sin(\Delta m \Delta t),$$

where

$$C = \frac{1 - |\lambda|^2}{1 + |\lambda|^2}, \quad S = \frac{2Im\lambda}{1 + |\lambda|^2}, \quad \lambda = \frac{q}{p}\frac{\bar{A}_{\rho^+\rho^-}}{A_{\rho^+\rho^-}}, \quad (11)$$

[1] This simple formula is valid only for the decays to longitudinally polarized ρ-mesons; fortunately $f_L = 0.99 \pm 0.03 \pm 0.03$.

and the factor $q/p = e^{-2i\beta}$ appears from $B_d - \bar{B}_d$ mixing. Here are the experimental data [6]:

$$C_{\rho^+\rho^-} = -0.23 \pm 0.24 \pm 0.14,$$
$$S_{\rho^+\rho^-} = -0.19 \pm 0.33 \pm 0.11. \qquad (12)$$

The smallness of the penguin contribution is manifested in the smallness of the $C_{\rho^+\rho^-}$ value in comparison with 1, and we see that even the value $C_{\rho^+\rho^-} = 0$ (and $P/T = 0$) does not contradict the data. Neglecting the penguin amplitude

$$S_{\rho^+\rho^-} = \sin 2\alpha = -0.19 \pm 0.35, \quad \alpha = 95° \pm 10°, \quad (13)$$

where the theoretical systematic uncertainty due to the nonzero P/T ratio is omitted.

3. $B \longrightarrow \pi\pi$. As it was demonstrated in paper [10] from the experimental data on the averaged branching ratios and asymmetries of $B_d(\bar{B}_d) \longrightarrow \pi^+\pi^-$, $\pi^0\pi^0$ and $B_u \longrightarrow \pi^+\pi^0$ decays, one can extract the angle α relying only on isospin relations for decay amplitudes. However, as it was noticed in the same paper, one should expect large experimental uncertainties in the parameters describing the decays to the pair of neutral pions, which will prevent direct determination of α with good accuracy. This really happens. Unfortunately, unlike in the case of $\rho\rho$ decays, the branching ratio of $B_d(\bar{B}_d) \longrightarrow \pi^0\pi^0$ is comparable to those charged modes preventing bounding of the penguin contributions to $B \longrightarrow \pi\pi$ decays. Let us note that the data of Belle and BaBar on $\pi^+\pi^-$ and $\pi^\pm\pi^0$ branching ratios well agree, while their difference in the $\pi^0\pi^0$ branching ratio is within two standard deviations. However, the considerable $B_d(\bar{B}_d) \longrightarrow \pi^0\pi^0$ branching ratio did not necessary mean that the penguin contribution is comparable to a tree one. In order to investigate how large it is, let us look at experimental data on $C_{\pi^+\pi^-}$ and $S_{\pi^+\pi^-}$. Here the data of Belle and BaBar are in disagreement [11]:

	BaBar	Belle	
$C_{\pi^+\pi^-}$	-0.09 ± 0.16	-0.56 ± 0.14	(14)
$S_{\pi^+\pi^-}$	-0.30 ± 0.17	-0.67 ± 0.17	

According to BaBar, the data on the tree amplitude dominates in the decay to $\pi^+\pi^-$ ($C_{\pi^+\pi^-} \approx 0$), while, according to Belle, this is not so ($C_{\pi^+\pi^-}$ differs from zero by four sigmas). That is why two data analyzing strategies were used: the Belle and BaBar data were either averaged (see for example [12]) or disregarded.

We do not want to average data that contradict each other, neither do we want to disregard them. Instead, we suppose that BaBar's data are correct, not Belle's. As an argument in favor of this statement, we can suggest the

results of paper [13], where the contributions of QCD penguin diagrams to $B \longrightarrow \rho\rho, \rho\pi, \pi\pi$ decays were found to be small. Neglecting them, from BaBar's measurement of $S_{\pi^+\pi^-}$, we obtain

$$\sin 2\alpha = S_{\pi^+\pi^-} = -0.30 \pm 0.17, \quad \alpha = 99° \pm 5°. \quad (15)$$

4. $B \longrightarrow \rho\pi$. The time dependence of these decays is given by the following formula [14]:

$$\frac{dN(B_d(\bar{B}_d) \longrightarrow \rho^{\pm}\pi^{\mp})}{d\Delta t} = (1 \pm A_{CP}^{\rho\pi})e^{-\Delta t/\tau}$$

$$\times [1 - q(C_{\rho\pi} \pm \Delta C_{\rho\pi})\cos(\Delta m \Delta t) \quad (16)$$

$$+ q(S_{\rho\pi} \pm \Delta S_{\rho\pi})\sin(\Delta m \Delta t)],$$

where $q = -1$ describes the B_d decay probability dependence on Δt (at $\Delta t = 0$, $\bar{B}_d$ decays) and $q = 1$ corresponds to the $\bar{B}_d$ decay probability dependence on Δt (at $\Delta t = 0$, B_d decays);

$$A_{CP}^{\rho\pi} = \frac{|A^{+-}|^2 - |\bar{A}^{-+}|^2 + |\bar{A}^{+-}|^2 - |A^{-+}|^2}{|A^{+-}|^2 + |\bar{A}^{-+}|^2 + |\bar{A}^{+-}|^2 + |A^{-+}|^2},$$

$$C_{\rho\pi} \pm \Delta C_{\rho\pi} = \frac{|A^{\pm\mp}|^2 - |\bar{A}^{\pm\mp}|^2}{|A^{\pm\mp}|^2 + |\bar{A}^{\pm\mp}|^2}, \quad (17)$$

$$S_{\rho\pi} \pm \Delta S_{\rho\pi} = \frac{2\mathrm{Im}\left(\frac{q}{p}\frac{\bar{A}^{\pm\mp}}{A^{\pm\mp}}\right)}{1 + \left|\frac{\bar{A}^{\pm\mp}}{A^{\pm\mp}}\right|^2}.$$

The amplitudes $A^{\pm\mp}$ describe B_d decays, $\bar{A}^{\pm\mp} - \bar{B}_d$ decays, and the first sign is that of the produced ρ meson (for example A^{+-} is the amplitude of $B_d \longrightarrow \rho^+\pi^-$ decay). It is convenient to write the amplitudes of $B \longrightarrow \rho\pi$ decays as sums of tree and penguin contributions:

$$A^{+-} = A_1 e^{i\delta_1} e^{i\gamma} + P_1 e^{i\delta_{P_1}},$$

$$A^{-+} = A_2 e^{i\delta_2} e^{i\gamma} + P_2 e^{i\delta_{P_2}},$$

$$\bar{A}^{-+} = A_1 e^{i\delta_1} e^{-i\gamma} + P_1 e^{i\delta_{P_1}}, \quad (18)$$

$$\bar{A}^{+-} = A_2 e^{i\delta_2} e^{-i\gamma} + P_2 e^{i\delta_{P_2}},$$

where the amplitude A_1 corresponds to ρ-mesons produced from W-bosons ($b \longrightarrow u\rho^-$, $\bar{b} \longrightarrow \bar{u}\rho^+$) and the amplitude A_2 describes the π-meson produced from the W-boson ($b \longrightarrow u\pi^-$, $\bar{b} \longrightarrow \bar{u}\pi^+$). Amplitude P_1 corresponds to a penguin diagram in which a spectator quark is involved in π-meson production, while P_2 corre-

sponds to participation of a spectator quark in ρ-meson production.

If one can neglect the penguin amplitudes, then the formulas for the physical observables are as follows:

$$A_{CP}^{\rho\pi} = C_{\rho\pi} = 0, \quad \Delta C_{\rho\pi} = \frac{A_1^2 - A_2^2}{A_1^2 + A_2^2},$$

$$\Delta S_{\rho\pi} = \frac{2A_1 A_2}{A_1^2 + A_2^2}\sin(\delta_2 - \delta_1)\cos 2\alpha, \quad (19)$$

$$S_{\rho\pi} = \frac{2A_1 A_2}{A_1^2 + A_2^2}\cos(\delta_2 - \delta_1)\sin 2\alpha.$$

We use the results of fits of the Δt distributions obtained by Belle [15] and BaBar [16].

Let us start from the experimental measurements of the parameter $C_{\rho\pi}$:

$$C_{\rho\pi} = \begin{array}{ll} 0.25 \pm 0.17, & \text{Belle,} \\ 0.34 \pm 0.12, & \text{BaBar,} \end{array} \quad (20)$$

and we see that while Belle's result is compatible with the hypothesis that $P/T \ll 1$, BaBar's result almost contradicts it. Waiting for more precise data let us go on supposing that the penguin contribution is negligible. By the way, the data on the A_{CP} confirms the smallness of the penguin amplitude:

$$A_{CP}^{\rho\pi} = \begin{array}{ll} -0.16 \pm 0.10, & \text{Belle,} \\ -0.088 \pm 0.051, & \text{BaBar.} \end{array} \quad (21)$$

For $\Delta C_{\rho\pi}$, the result is

$$\Delta C_{\rho\pi} = \begin{array}{ll} 0.38 \pm 0.18, & \text{Belle,} \\ 0.15 \pm 0.12, & \text{BaBar,} \end{array} \quad (22)$$
$$(\Delta C_{\rho\pi})_{\text{average}} = 0.22 \pm 0.10$$

and it means that $A_1 \approx 1.3 A_2$.

For $\Delta S_{\rho\pi}$, we have

$$\Delta S_{\rho\pi} = \begin{array}{ll} -0.30 \pm 0.25, & \text{Belle,} \\ 0.22 \pm 0.15, & \text{BaBar,} \end{array} \quad (23)$$
$$(\Delta S_{\rho\pi})_{\text{average}} = 0.08 \pm 0.13$$

and its smallness means that $\sin(\delta_1 - \delta_2) \approx 0$ (another solution, $\cos 2\alpha \approx 0$, is unacceptable). It means that both δ_1 and δ_2 are small or that they are close to each other. Substituting $\cos(\delta_1 - \delta_2) = 1$ into the expression for $S_{\rho\pi}$, we obtain

$$S_{\rho\pi} = \sqrt{1 - (\Delta C_{\rho\pi})^2}\sin 2\alpha, \quad (24)$$

while the experimental results are

$$S_{\rho\pi} = \begin{array}{l} -0.28 \pm 0.25, \quad \text{Belle}, \\ -0.10 \pm 0.15, \quad \text{BaBar}, \end{array} \qquad (25)$$

$$(S_{\rho\pi})_{\text{average}} = -0.15 \pm 0.13$$

From (22), (24), and (25), we obtain

$$\alpha = 94° \pm 4°. \qquad (26)$$

5. Conclusions. Averaging the results for α presented in Eqs. (13), (15), and (26), we obtain

$$\alpha = 96° \pm 3°, \qquad (27)$$

where only the experimental error is taken into account, while the theoretical uncertainty coming from the penguin diagrams is neglected. Let us note that result (27) is in good agreement with the global CKM fit results:

$$\alpha_{\text{UTfit}}^{[7]} = 94° \pm 8°, \quad \alpha_{\text{CKMfitter}}^{[8]} = 94° \pm 10°, \qquad (28)$$

$$\alpha_{\text{AOV}}^{[9]} = 100° \pm 5°.$$

How large can penguin contributions be in comparison with tree ones?

Strong interaction renormalization for beauty hadron weak decays is much smaller than for strange particles, because the masses of beauty hadrons are much closer to M_W in the logarithmic scale. Here are the results of NLO calculations from Table 1 of paper [17], where we take numbers which correspond to the modern value of $\alpha_s(M_Z) = 0.12$ ($\Lambda_4 = 280$ MeV):

$$c_2 = 1.14, \quad c_1 = -0.31, \quad c_3 = 0.016,$$

$$c_5 = 0.010, \quad c_4 = -0.036, \qquad (29)$$

$$c_6 = -0.045$$

and we observe that the renormalization coefficients of the penguin operators ($O_3 - O_6$) do not exceed 4% of that for tree-level operator (O_2). Concerning the matrix elements, one can definitely state that a large enhancement factor $m_\pi^2/(m_u + m_d)m_s \approx 10$, which makes penguins so important in explaining the $\Delta I = 1/2$ rule in nonleptonic weak decays of strange particles, is absent in beauty hadron decays, being substituted by $m_\pi^2/(m_u + m_d)m_b \approx 1/2$.

A grain of salt comes from the CKM matrix elements, which enhance the penguin amplitude with respect to the tree one by a factor of $(\rho^2 + \eta^2)^{-0.5} \approx 2$.[2]

It follows that the theoretical uncertainty in (27) coming from the penguin diagrams can be close to the experimental one.

REFERENCES

1. K. Abe *et al.* (Belle Collab.), hep-ex/0408111; B. Aubert *et al.* (BaBar Collab.), hep-ex/0408127 (2004).

2. Y. Grossman and H. R. Quinn, Phys. Rev. D **58**, 017 504 (1998).

3. B. Aubert *et al.* (BaBar Collab.), Phys. Rev. Lett. **93**, 231 801 (2004).

4. B. Aubert *et al.* (BaBar Collab.), Phys. Rev. Lett. **91**, 171 802 (2003).

5. K. Abe *et al.* (Belle Collab.), Phys. Rev. Lett. **91**, 221 801 (2003).

6. B. Aubert *et al.* (BaBar Collab.), hep-ex/0407051 (2004).

7. J. Charles *et al.* (The CKMfitter Group), hep-ph/0406184 (2004).

8. M. Bona *et al.* (UTfit Collab.), hep-ph/0501199 (2005).

9. E. A. Andriyash, G. G. Ovanesyan, and M. I. Vysotsky, hep-ph/0502111 (2005).

10. M. Gronau and D. London, Phys. Rev. Lett. **65**, 3381 (1990).

11. B. Aubert *et al.* (BaBar Collab.), hep-ex/0501071 (2005); K. Abe *et al.* (Belle Collab.), hep-ex/0502035 (2005).

12. A. Ali, E. Lunghi, and A. Ya. Parkhomenko, Eur. Phys. J. C **36**, 183 (2004); A. Ya. Parkhomenko, hep-ph/0411061 (2004); M. Gronau, hep-ph/0407316 (2004).

13. R. Aleksan *et al.*, Phys. Lett. B **356**, 95 (1995).

14. M. Gronau, Phys. Lett. B **233**, 479 (1989).

15. C. C. Wang *et al.* (Belle Collab.), hep-ex/0408003 (2004).

16. B. Aubert *et al.* (BaBar Collab.), hep-ex/0408099 (2004).

17. A. J. Buras, M. Jamin, M. E. Lautenbacher, and P. H. Weisz, Nucl. Phys. B **370**, 69 (1992).

_____

[2] We are grateful to P.N. Pakhlov for this remark.

Search for Solar Axions Emitted in an *M*1 Transition in ⁷Li* Nuclei

A. V. Derbin, A. I. Egorov, I. A. Mitropolsky, and V. N. Muratova

Petersburg Nuclear Physics Institute, Russian Academy of Sciences, Gatchina, 188300 Russia
e-mail: derbin@mail.pnpi.spb.ru
Received March 16, 2005

The resonance absorption of solar axions by ⁷Li nuclei, which is accompanied by the excitation of the first nuclear level of lithium $a + {}^7\text{Li} \longrightarrow {}^7\text{Li}^* \longrightarrow {}^7\text{Li} + \gamma$, is sought. To this end, the energy spectrum has been measured by an HPGe detector that is surrounded by a LiOH layer. A new upper limit $m_a \leq 16$ keV (at 90% C.L.) has been determined for the mass of the hadron axion. © *2005 Pleiades Publishing, Inc.*

PACS numbers: 14.80.Mz

1. INTRODUCTION

The solution to the problem of the *CP* violation in strong interactions was proposed by Peccei and Quinn on the basis of new global chiral symmetry [1]. The spontaneous breaking of this symmetry at energy f_a compensates the *CP* breaking term in the QCD Lagrangian and it implies the existence of the axion, i.e., a neutral pseudoscalar particle with mass $m_a \sim (140 \text{ MeV})^2/f_a$ [2, 3]. It is assumed in the initial model that the symmetry is broken at the weak-interaction scale $f_a \sim (\sqrt{2}\, G_F)^{-1/2} = 247$ GeV. The existence of this "standard" axion with mass in the range 0.1–1.0 MeV was certainly excluded by a number of experiments that were carried out with radioactive sources [4, 5] at reactors [6, 7] and accelerators [8, 9] in order to detect decays of the axion into two photons or decays of heavy quarkonia with the emission of the axion.

In two classes of new theoretical models of an invisible axion, the axion remains in the form that is necessary for solving the problem of *CP* conservation in strong interactions, and its interaction with photons ($g_{a\gamma\gamma}$), leptons (g_{aee}), and hadrons (g_{aNN}) is suppressed. These are models of hadron or KSVZ axion [10, 11] and GUT or DFSZ axion [12, 13]. The symmetry breaking scale f_a in them is arbitrary and it can be continued to the Planck mass. Since the amplitude of the interaction of the axion with hadrons and leptons is proportional to the axion mass, the interaction of the invisible axion with matter is correspondingly suppressed. Owing to this circumstance, it is reasonable to continue experiments on search for a pseudoscalar particle that weakly interacts with matter and whose mass may be from 10^{-12} eV to several tens of keV. Detailed theoretical and experimental reviews were given by the Particle Data Group [14].

The considerable difference of the hadron axion from the DFSZ axion is that it does not directly interact with leptons, and its interaction with photons may be strongly suppressed [15]. As a result, the laboratory experiments on search for both the conversion of the axion into the photon in a magnetic field [16–23] or an electric field of a crystal [24–26] and the emission of the axion in nuclear magnetic transitions [27, 28], as well as astrophysical data [29, 30], do not exclude the possibility of the existence of the hadron axion with a mass of several tens of electronvolts [31, 32].

If the axion exists, the Sun is an intense source of these particles. The axion can be efficiently produced in the Sun due to the Primakov effect that leads to the transformation of photons into axions in the plasma electromagnetic field. Axions can be also produced in magnetic transitions in nuclei (⁵⁷Fe, ⁵⁵Mn, ²³Na, etc.) whose low-lying levels are excited due to high temperature [33]. These axions can be detected through resonance absorption in nuclei [34–37]. The probability of emission and subsequent absorption of the axion in a magnetic transition is determined only by the parameter g_{aNN}.

Another possible source of axions is presented by solar cycle reactions. Figure 1 shows the scheme of the electron capture ${}^7\text{Be} + e \longrightarrow {}^7\text{Li}({}^7\text{Li}^*) + \nu_e$ [38]. With a probability of ≈0.1, the electron capture is accompanied by the excitation of the $1/2^-$ ⁷Li state, which is deexcited through an *M*1 transition with the emission of a γ-ray photon. The expected flux of axions that are emitted in this transition is directly related to the flux of ⁷Be neutrinos, which is equal to 4.8×10^9 ν/(cm² s) on the ground and is comparable with axion fluxes from a nuclear reactor or artificial radioactive sources. An attempt to detect such axions was made in [36].

In the long-wavelength approximation, the ratio of the probabilities ω_γ and ω_a of nuclear electromagnetic
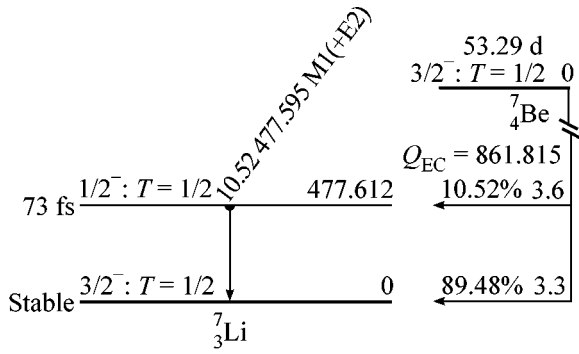
Fig. 1. Scheme of the electron capture $^7\text{Be} + e \longrightarrow$ $^7\text{Li}(^7\text{Li}^*) + \nu_e$ [38].
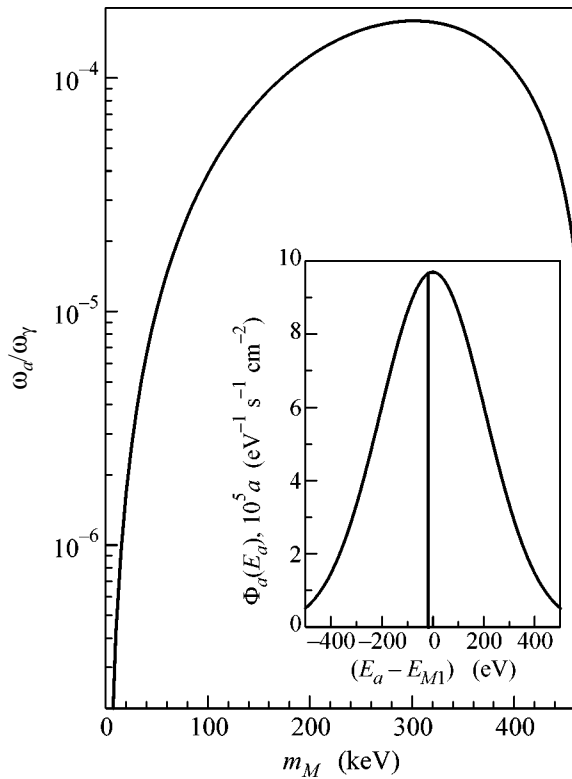

Fig. 2. Ratio of the probabilities of axion and magnetic transitions. The inset shows the expected spectrum of solar axions that are emitted in the $M1$ transition from $^7\text{Li}^*$ for $\omega_a/\omega_\gamma = 1$. The vertical straight line indicates the axion energy shift due to the recoil of the ^7Li nucleus.

and axion transitions, respectively, is given by the expression [5]

$$\frac{\omega_a}{\omega_\gamma} = \frac{1}{2\pi\alpha}\frac{1}{1+\delta^2}\left[\frac{g^0_{aNN}\beta + g^3_{aNN}}{(\mu_0 - 0.5)\beta + \mu_3 - \eta}\right]^2\left(\frac{k_a}{k_\gamma}\right)^3. \quad (1)$$

Here, k_γ and k_a are the momenta of the photon and axion, respectively; $\delta = E2/M1 \approx 0$ is the ratio of the

probabilities of the $E2$ and $M1$ transitions; $\alpha \approx 1/137$ is the fine structure constant; $\mu_0 \approx 0.88$ and $\mu_3 \approx 4.71$ are the isoscalar and isovector magnetic moments, respectively; and $\beta \approx 1$ and $\eta \approx 0.5$ are the parameters depending on nuclear matrix elements. The isoscalar (g^0_{aNN}) and isovector (g^3_{aNN}) coupling constants of the KSVZ axion with nucleons can be expressed in terms of the axion mass measured in electronvolts [15, 36, 39]:

$$g_0 = -3.51 \times 10^{-8} m_a, \quad g_3 = -2.80 \times 10^{-8} m_a. \quad (2)$$

Then, the ratio ω_a/ω_γ is expressed in terms of the axion mass as (see Fig. 2)

$$\omega_a/\omega_\gamma = 4.12 \times 10^{-15} m_a^2 (k_a/k_\gamma)^3. \quad (3)$$

Owing to the Doppler broadening, the energy spectrum of axions is a Gaussian with the standard deviation $\sigma_S(T) = E_\gamma(kT/M_{7\text{Li}})$, where T is the temperature at the point where the axion is produced and $M_{7\text{Li}}$ is the mass of the ^7Li nucleus. The temperature $T = 1.5 \times 10^7$ K at the center of the Sun corresponds to the linewidth $\sigma_S(T) = 210$ eV. The expected energy spectrum of axions $\Phi_a(E_a)$, which is calculated taking into account the dependence of the temperature and number of $e +$ $^7\text{Be} \longrightarrow {}^7\text{Li} + \nu$ events on the Sun radius [40], is shown in the inset in Fig. 2. It is seen that FWHM $= 2.36\sigma_s \approx$ 500 eV. The lifetime of the first excited ^7Li level is equal to 105 fs, and the corresponding natural width of the level is $\Gamma = 0.0063$ eV (Fig. 1). The electron conversion coefficient for the transition to the ground state is negligibly small. The Doppler broadening of the line for the temperature $T = 300$ K at the point of the location of the target nuclei is equal to 0.95 eV. The natural width and Doppler broadening, as well as the axion energy shift due to the recoil energy of the ^7Li nucleus (17 eV), are much less than the axion spectrum width. Thus, the fraction of axions that can be resonantly absorbed is $\sim\Gamma/\sigma_S$.

The cross section for the resonance absorption of axions with energy E_a is given by the following expression, which is similar to that for the resonance absorption of γ rays corrected to the ratio ω_a/ω_γ:

$$\sigma(E_a) = \sqrt{\pi}\sigma_{0\gamma}\exp\left[-\frac{4(E_a - E_{M1})^2}{\Gamma^2}\right]\left(\frac{\omega_a}{\omega_\gamma}\right). \quad (4)$$

Here, the maximum cross section for the resonance absorption of $\sigma_{0\gamma}$ rays is given by the expression

$$\sigma_{0\gamma} = \frac{2I_1 + 1}{2I_0 + 1}\frac{2\pi\lambda^2}{1 + \alpha}, \quad (5)$$

where I_0 and I_1 are the spins of the ground and excited states of the ^7Li nucleus, respectively; $\lambda = \hbar c/E_{M1}$ is the reduced length of the γ rays; and $\alpha \approx 0$ is the electron conversion factor for this transition. The cross section

σ_0 for axions is twice as large as the value for photons due to the difference between the spins of the axion and photon, $\sigma_{0a} = 2\sigma_{0\gamma}$ [34].

In order to obtain the total cross section, expression (4) should be integrated over the axion spectrum. The integration of narrow Gaussian (4) over a wide axion spectrum yields a value close to $\Phi(E_1)$, which is indicated by the vertical straight line in Fig. 2. The rate of the absorption of solar axions by the ^{7}Li nucleus is given by the expression

$$R_a \cong \pi\sigma_{0a}\Gamma\Phi_a(E_{M1})(\omega_a/\omega_\gamma). \qquad (6)$$

Using the dependence of $\Phi_a(E_a)$ and $\sigma_a(E_a)$ on ω_a/ω_γ, as well as the dependence of ω_a/ω_γ on m_a, one can calculate the expected number of axion absorption events in a target, where the number of ^{7}Li nuclei is equal to $N_{7\text{Li}}$, for measurement time t:

$$R = N_{7\text{Li}}tR_a = N_{7\text{Li}}t1.74 \times 10^{-45}(m_a)^4. \qquad (7)$$

The number of detected γ-ray photons that are emitted after the axion absorption is determined by the efficiency of the detector, and the probability of observing the 477.6-keV peak is determined by the background level in the experimental setup.

2. EXPERIMENTAL SETUP

To detect 477.6-keV γ rays, we use a 160-cm^3 cylindrical coaxial HPGe detector 60 mm in diameter and 60 mm in length. It was surrounded by 3.9 kg of LiOH, which was pressed to a density of $\approx$0.6 g/cm^3. A LiOH target had the form of a sleeve 210 mm in length with walls 60 mm thick and a bottom 70 mm in thickness. It was closely put on the vacuum valve of a Ge detector. The passive shielding consisted of a copper shell 10 mm thick, which covered the LiOH sample under investigation, a Bi$_2$O$_3$ layer 20 g/cm^2 thick, and a 50-mm lead layer.

The setup was placed on the ground. In order to suppress the cosmic ray background, we used an active shielding consisting of five $500 \times 500 \times 120$-mm plastic scintillators. The total loading with the active shielding was equal to 600 pulse/s, which resulted in 7% dead time for a blanking pulse duration of 120 μs. Measuring the signal spectrum of the Ge detector in coincidence with the active shielding, one can determine the probability of exciting the first ^{7}Li level by the nuclear active component and cosmic ray muons.

The Ge detector had two spectrometer channels with different amplification factors for the soft (up to 1.5 MeV) and harder (up to 5 MeV) parts of the spectrum. This property made it possible to monitor the background level over the entire range of natural radioactivity and to detect photons with energy corresponding to the second excited state of the ^{7}Li nucleus. The spectrometric channel included a preamplifier with resistive feedback, an amplifier, and a 12-digit analog-
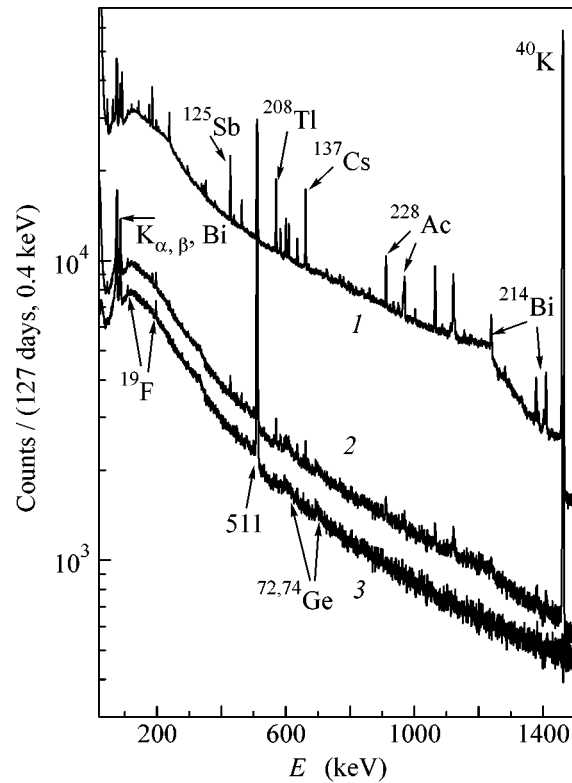

Fig. 3. Energy spectrum measured by the Ge detector for 126.5 days: (*1*) signals that have not been detected by the active shielding, (*2*) signals in coincidence with the active shielding, and (*3*) signals in coincidence with the active shielding taking into account accidental coincidences whose number is determined from the intensity of the ^{40}K peak in spectrum *2*.

to-digital converter. The channel scale was equal to 0.4 and 1.2 keV for the first and second analog-to-digital converters, respectively. Four 4096 channel spectra in two energy intervals in coincidence and anticoincidence with an active-shielding signal were accumulated in a computer memory.

The efficiency of the detection of 477.6-keV photons was determined using a standard ^{152}Eu source with 411.1- and 444.0-keV γ lines. The latter line is close to the desired 478-keV ^{7}Li line. The difference between the energies of the first and second lines of the source enabled us to introduce necessary corrections to the efficiency of the detection of the 478-keV line. The ^{152}Eu source was sequentially placed at different points inside the LiOH volume. The efficiency was determined taking into account the experimental dependence of the probability of the scattering and absorption of γ rays on the thickness of the LiOH layer. The efficiency thus determined for the detection of 478-keV photons that were uniformly distributed over the LiOH volume was equal to (0.92 ± 0.1)%.
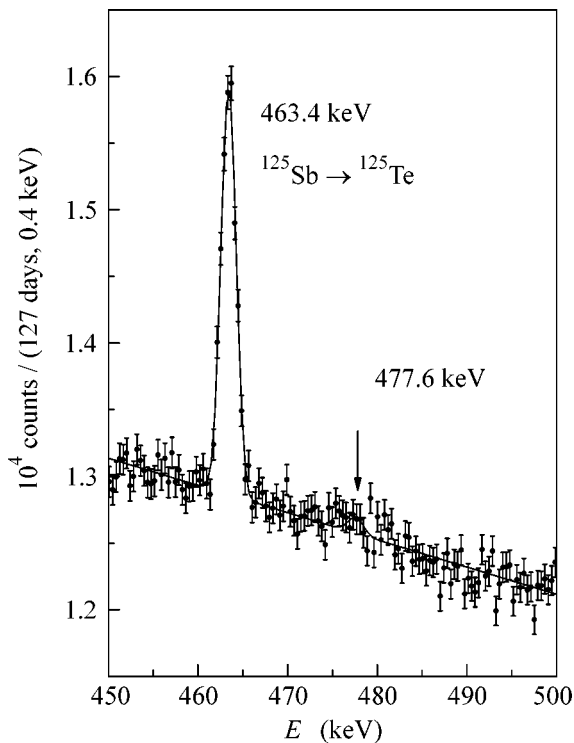
Fig. 4. Fit to the spectrum of signals that were detected in anticoincidence with the active shielding (spectrum *1* in Fig. 3) in the range 450–500 keV. The upper limit on the number of events in the 477.6-keV peak is equal to 1040 events for 90% C.L.

Fig. 5. Fit to the spectrum of signals that were detected in coincidence with the active-shielding signal (spectrum *2* in Fig. 3) in the range 450–500 keV. The number of events in the 477.6-keV peak is equal to 840 ± 170. The 463.4-keV peak is attributed to accidental coincidences.

3. RESULTS

Measurements continued for 126.5 days in the form of runs with a duration of ~1 day. Figure 3 shows the measured energy spectra up to 1.5 MeV. The spectrum of all signals that were detected by the Ge detector and that did not coincide with a signal from the active shielding is marked as *1*. In this spectrum, 40 pronounced peaks are identified, which are associated with the activity of uranium and thorium families, ^{40}K, ^{125}Sb, and ^{207}Bi. The ^{40}K peak appeared to be most intense and its activity makes the basic contribution to the detector background for energies below 1.4 MeV. Its intensity was equal to 5100 events per day and it was primarily associated with the insufficient passive shielding of the Ge detector. Another possible source of ^{40}K is the LiOH sample. For 0.1 wt % of natural potassium, the intensity of the ^{40}K peak is equal to ~2000 events per day.

The spectrum of signals that were detected in coincidence with a signal from the active shielding is marked as *2* in Fig. 3. This spectrum contains the 511-keV peak, which corresponds to the detection of annihilation photons, and peaks of the characteristic x-ray radiation of bismuth and lead (the lead layer was covered the detector on the side of a cooling pipe). Since the total duration of the active-shielding signals is equal to 7% of the total measurement time, some sig-
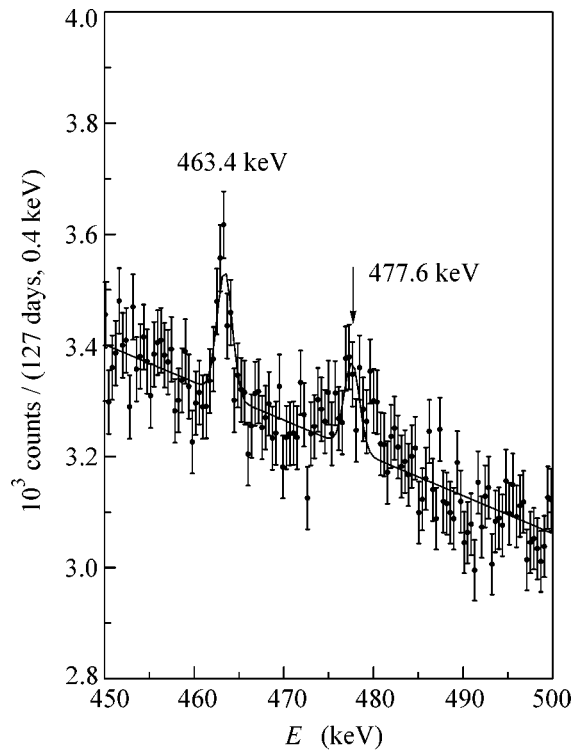
nals in spectrum *2* are attributed to accidental coincidences. Taking into account the intensity of the ^{40}K peak associated with accidental coincidences, one can obtain the spectrum of signals that really coincide with an active-shielding signal (spectrum *3*). This spectrum contains peaks that correspond to the excitation of low-lying ^{19}F levels (109 and 197 keV) from Teflon, which was used in the container for LiOH, and peaks that are associated with the excitation of nuclear levels of Ge isotopes (692 keV from ^{72}Ge, 596 keV from ^{74}Ge, etc.). The latter peaks are significantly broadened due to the kinetic energy gained when exciting Ge nuclei.

Figures 4 and 5 show spectra *1* and *2*, respectively, in the energy range 450–500 keV. The energy resolution that was determined for the 463-keV γ line ($^{125}Sb \longrightarrow {}^{125}Te$ beta decay), which was manifested in measurements, was equal to 1.9 keV.

In order to determine the intensity of the 477.6-keV peak, the maximum likelihood method was used. The likelihood function was determined under the assumption that the number of counts in each channel has a normal distribution and it is the sum of the linear function, which is taken for describing the continuous background, and two Gaussians. The first Gaussian describes the 463.4-keV peak and it includes three free parameters: area (S_1), position (E_1), and standard devi-

ation (σ_1). The second Gaussian was characterized by the fixed position ($E_2 = 477.6$ keV), the standard deviation that was equal to the peak FWHM 463.4 keV ($\sigma_2 = \sigma_1$), and the peak area S_2 as a free parameter. Thus, there were six free parameters: two parameters described the linear background, three parameters corresponded to the 463.4-keV peak, and one parameter described the 477.6-keV peak. The total number of degrees of freedom in the interval 450–500 keV was equal to 125.

Figure 4 shows the fit to spectrum 1 that corresponds to the minimum $\chi^2 = 129.2/125$. The area of the 477.6-keV peak was determined as 630 ± 320 events. The upper limit (at 90% C.L.) on the number of events in the peak was determined by the standard calculation: χ^2 was calculated for various fixed S_2 values by varying the other five free parameters. The upper limit thus obtained was equal to $S_{lim} = 1040$ events.

The most probable processes that are responsible for the excitation of the first nuclear ^{7}Li level and that are not accompanied by a signal from the active shielding are the inelastic scattering of fast neutrons ($\sigma \approx 0.15$ b for $E_n \approx 1$ MeV) [41], the radiative capture of thermal neutrons ^{6}Li$(n, \gamma)^7$Li* ($\sigma = 38$ b), the inelastic scattering of α particles produced in the process ^{6}Li$(n, \alpha)^3$H ($\sigma = 945$ b, $E_\alpha = 2$ MeV) $\longrightarrow$ ^{7}Li$(\alpha, \alpha')^7$Li* ($\sigma = 100$ mb) of the capture of thermal neutrons by ^{6}Li nuclei, and the process ^{10}B$(n, \alpha)^7$Li* ($\sigma = 3800$ b) of the capture of neutrons by the ^{10}B isotope if it is present in the LiOH sample.

According to Eq. (7), for the number $N_{^7Li} = 9.02 \times 10^{25}$ of ^{7}Li nuclei in the target, the measurement time $t = 1.09 \times 10^7$ s, and the detection efficiency $\varepsilon = 0.92$, the upper limit on the axion mass is $m_a \leq 16.0$ keV. This result is twice as stringent as that obtained in [36] and it nearly closes the window of possible axion masses to the next possible intense source of monochromatic solar axions, which is the 14.4-keV M1 transition in the ^{57}Fe nucleus [34].

Similar analysis was performed for the spectrum of signals detected in coincidence with the active shielding (Fig. 5). The position and width of the 463.4-keV peak were taken from the fit of spectrum 1. The area of the peak was determined as (1200 ± 180) events, which is consistent with the 7% probability of accidental coincidences of signals from the Ge detector and active shielding. The intensity of the 477.6-keV peak was determined as 840 ± 170.

The sensitivity of the procedure is limited on the ground primarily by the flux of neutrons that enter the setup with energies above 0.5 MeV ($\sim 10^{-3}$ n/cm^2 s) [42] and that are not detected by the active shielding and have the maximum cross section (~ 0.1 b [41]) of inelastic scattering ^{7}Li$(n, n')^7$Li* that is accompanied by the excitation of the 478-keV level.

4. CONCLUSIONS

The resonance absorption of solar axions by ^{7}Li nuclei, which is accompanied by the excitation of the first nuclear level of lithium: $a + {}^7\text{Li} \longrightarrow {}^7\text{Li*} \longrightarrow {}^7\text{Li} + \gamma$, is sought. To detect this reaction, the HPGe detector that was surrounded by the 3.9-kg LiOH layer was used. The detector and target were placed inside the low-background setup equipped with the passive and active shieldings. In the energy spectrum that were measured by the HPGe detector for 126.5 days, the intensity of the 477.6-keV peak, which corresponds to the first excited level of ^{7}Li, was equal to (5.0 ± 2.6) count/day. This intensity provides a new upper limit $m_a \leq 16$ keV (at 90% C.L.) for the mass of the hadron axion. This result nearly closes the window of possible axion masses to the energy 14.4 keV of the M1 transition in the ^{57}Fe nucleus.

REFERENCES

1. R. D. Peccei and H. Quinn, Phys. Rev. Lett. **38**, 1440 (1977); Phys. Rev. D **16**, 1791 (1977).
2. S. Weinberg, Phys. Rev. Lett. **40**, 223 (1978).
3. F. Wilczek, Phys. Rev. Lett. **40**, 279 (1978).
4. A. Zender, Phys. Lett. B **104**, 498 (1981).
5. F. T. Avignone, C. Baktash, W. C. Barker, et al., Phys. Rev. D **37**, 618 (1988).
6. J. L. Vuilleumier, F. Boehm, A. A. Hahn, et al., Phys. Lett. B **101**, 341 (1981).
7. S. N. Ketov, Yu. V. Klimov, S. V. Nikolaev, et al., Pis'ma Zh. Éksp. Teor. Fiz. **44**, 114 (1986) [JETP Lett. **44**, 146 (1986)].
8. H. Faissner, E. Frenzel, W. Heinrigs, et al., Phys. Lett. B **96**, 201 (1980).
9. M. J. Savage, B. W. Filippone, W. K. Kellogg, et al., Phys. Rev. D **37**, 1134 (1988).
10. J. E. Kim, Phys. Rev. Lett. **43**, 103 (1979).
11. M. A. Shifman, A. I. Vainstein, and V. I. Zakharov, Nucl. Phys. B **166**, 493 (1980).
12. A. R. Zhitnitskiĭ, Yad. Fiz. **31**, 497 (1980) [Sov. J. Nucl. Phys. **31**, 260 (1980)].
13. M. Dine, F. Fishler, and M. Srednicki, Phys. Lett. B **104**, 199 (1981).
14. S. Eidelman, K. G. Hayes, K. A. Olive, et al. (Particle Data Group), Phys. Lett. B **592**, 1 (2004).
15. D. B. Kaplan, Nucl. Phys. B **260**, 215 (1985).
16. P. Sikivie, Phys. Rev. Lett. **51**, 1415 (1983); Phys. Rev. D **32**, 2988 (1985).
17. L. Krauss, J. Moody, F. Wilczek, et al., Phys. Rev. Lett. **55**, 1797 (1985).
18. W. Wuensch, S. De Panfilis-Wuensch, Y. K. Semertzidis, et al., Phys. Rev. D **40**, 3153 (1989).
19. C. Hagmann, D. Kinion, W. Stoeffl, et al., Phys. Rev. Lett. **80**, 2043 (1998).
20. M. Muck, J. B. Kycia, and J. Clarke, Appl. Phys. Lett. **78**, 967 (2001).

21. D. Lazarus, G. Smith, R. Cameron, *et al.*, Phys. Rev. Lett. **69**, 2333 (1992).

22. Y. Inoue, T. Namba, S. Moriyama, *et al.*, Phys. Lett. B **536**, 18 (2002).

23. S. Anriamonie *et al.*, hep-ex/0411033 (2004).

24. A. Morales *et al.,* Astropart. Phys. **16**, 325 (2002).

25. F. T. Avignone *et al.*, Nucl. Phys. (Proc. Suppl.) **72**, 176 (1999).

26. R. Bernabei, P. Belli, R. Cerulli, *et al.*, Phys. Lett. B **515**, 6 (2001).

27. M. Minowa, Y. Inoue, T. Asanuma, *et al.*, Phys. Rev. Lett. **71**, 4120 (1993).

28. A. V. Derbin, A. I. Egorov, I. A. Mitropol'skiĭ, *et al.*, Pis'ma Zh. Éksp. Teor. Fiz. **65**, 576 (1997) [JETP Lett. **65**, 605 (1997)]; Yad. Fiz. **65**, 1335 (2002) [Phys. At. Nucl. **65**, 1302 (2002)].

29. M. S. Turner, Phys. Rep. **67**, 197 (1990).

30. G. G. Raffelt, Phys. Rep. **198**, 1 (1990).

31. G. G. Raffelt, *Stars as Laboratories for Fundamental Physics* (Univ. of Chicago Press, Chicago, 1996).

32. T. Moroi and H. Murayama, Phys. Lett. B **440**, 69 (1998).

33. W. C. Haxton and K. Y. Lee, Phys. Rev. Lett. **66**, 2557 (1991).

34. S. Mariyama, Phys. Rev. Lett. **75**, 3222 (1995).

35. M. Krcmar, Z. Krecak, M. Stipcevi, *et al.*, Phys. Lett. B **442**, 38 (1998).

36. M. Krcmar, Z. Krecak, A. Ljubicic, *et al.*, Phys. Rev. D **64**, 115016 (2001).

37. K. Jakovcic, Z. Krecak, M. Krcmar, *et al.*, nucl-ex/0402016 (2004).

38. *Table of Isotopes*, Ed. by C. M. Lederer and V. S. Shirley, 7th ed. (Wiley, New York, 1978).

39. M. Srednicki, Nucl. Phys. B **260**, 689 (1985).

40. J. N. Bahcall, M. H. Pinsonneault, and S. Basu, Astrophys. J. **555**, 990 (2001).

41. I. V. Gordeev, D. A. Kardashev, and A. V. Malyshev, *Nuclear Physical Constants* (Gosatomizdat, Moscow, 1963) [in Russian].

42. G. V. Gorshkov *et al.*, *Natural Neutron Background of the Atmosphere and Earth's Crust* (Atomizdat, Moscow, 1966) [in Russian].

Translated by R. Tyapaev

Determination of Rovibronic Term Values of a Diatomic Molecule from Experimental Data on the Wavenumbers of Spectral Lines

B. P. Lavrov and M. S. Ryazanov

Faculty of Physics, St. Petersburg State University, Peterhof, St. Petersburg, 198904 Russia
e-mail: lavrov@pobox.spbu.ru
Received January 11, 2005; in final form, March 10, 2005

It has been shown that, if experimental data are available on the lines of the rovibronic spectrum of a diatomic molecule that pairwise couple *three or more* vibronic states, then there is a relation between the wavenumbers measured for the lines and the absolute values of all corresponding rovibronic term values. A method is proposed for determining the optimal set of rovibronic term values with error estimations by varying the desired values of the rovibronic term values so as to minimize the weighted standard deviation of the wavenumbers that are calculated according to the Rydberg–Ritz combination principle from the wavenumbers measured for a sufficiently large number of rovibronic spectral lines of various systems of bands. It is substantial that this method does not require *any* assumptions on the molecular structure. The new method is applied to determine the rovibronic term values of 12 singlet electronic states of the isotopomer $^{11}B^1H$ of the boron hydride molecule, which have already been studied experimentally, with the use of all available experimental data for 15 systems of bands, which are obtained in 10 works. Thus, the energy spectrum of the diatomic molecule has been determined from the experimental data on the wavenumbers of rovibronic spectral lines without any assumption on its structure. © *2005 Pleiades Publishing, Inc.*

PACS numbers: 33.15.Mt, 33.20.–t

We point to the following contradiction. On the one hand, the basic energy characteristic of a diatomic molecule in quantum mechanics is the energy spectrum of stationary states, i.e., a set of rovibronic term values. On the other hand, sets of molecular constants are used as the basic energy characteristics in molecular spectroscopy [1–3]. The set of rovibronic term values is an actual characteristic of a molecule, whereas the physical meaning of molecular constants is rather uncertain. Empirical values of the constants depend on a theoretical model used to analyze the spectrum, on a particular procedure for processing wavenumbers, and even on the amount of experimental data and their distribution over vibrational and rotational levels [4]. For this reason, the available methods for determining the energy characteristics of molecules from measured rovibronic spectra allow certain subjectivity of a researcher.

The second feature of the standard approach is that so-called combination differences $\Delta_2(J)$, which are the differences between the wavenumbers of pairs of spectral lines that correspond to the common lower or common upper rovibronic level, are used both to identify spectra and to determine the molecular constants. These differences are obviously equal to the differences between the corresponding rovibronic term values of only upper, $\Delta_2'(J)$, or only lower, $\Delta_2''(J)$, vibronic states. As an example, Fig. 1 shows a fragment of the rotational structure of the $v'–v''$ band of the $^1\Lambda^\pm–^1\Sigma^+$ elec-

tronic transition. It is seen that the differences between the wavenumbers of the corresponding pairs of lines of the R and P branches are equal to the differences between rovibronic term values with the rotational quantum numbers $J + 1$ and $J – 1$.

However, following this way, it is impossible to find a relation between levels with even and odd J values. According to the Laporte selection rule, electric dipole transitions are possible only between rovibronic levels with opposite parities (+ and –). Therefore, if a pair of lines corresponds to one common level, two other levels, the differences between the term values of which are combination differences, have the same parity. At the same time, neighboring rotational levels have opposite parities.

As a result, the set of desired rovibronic term values is divided into two groups that are coupled by optical transitions with only even or only odd rotational levels of the lower electronic state (see Fig. 1).[1] This is the known problem (see [5, 6]) arising from the rotational level sets that correspond to even and odd J values and that are not coupled with each other. We emphasize that their mutual arrangement cannot be determined using only the Rydberg–Ritz combination principle if rovibronic spectral lines of only one band system are used.

---

[1] Note that the existence of lines of the Q branches ($J'' = J'$) does not help, because the rovibronic levels ($^1\Lambda^+$, v', J') and ($^1\Lambda^-$, v', J') do not coincide with each other (Λ-doubling effect).
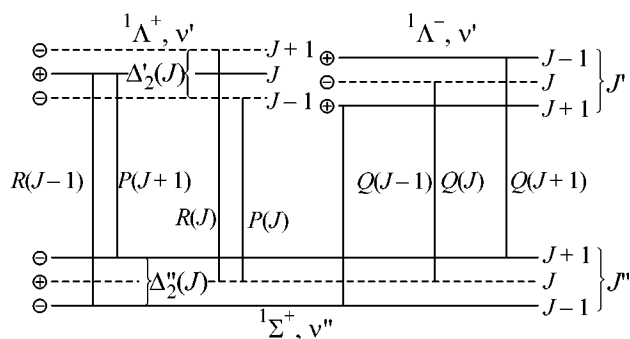
Fig. 1. Grotrian diagram that illustrates a fragment of the rotational structure of the $^{1}\Lambda^{\pm}$, v'–$^{1}\Sigma^{+}$, v'' band, combination differences $\Delta_2''(J)$ and $\Delta_2'(J)$, and the existence of (solid and dashed straight lines) two groups of rovibronic levels whose relative position cannot be determined from the wavenumbers of the rovibronic lines of a given band system.

To solve this problem, one has to use not only the Rydberg–Ritz combination principle but also additional assumptions [7, 8].

The third feature of the standard approach is that the sets of molecular constants for each electronic state are determined sequentially at several stages. First, the rotational structure of each band is analyzed and rotational constants $\{B_v, D_v, \ldots\}$ for each vibronic state are obtained by approximating the $\Delta_2'(J)$ and $\Delta_2''(J)$ dependences. The v dependences of these constants are used to determine the constants $\{B_e, \alpha_e, D_e, \ldots\}$. Then, the v' and v'' progressions of the bands are analyzed and, using the rotational constants, the vibrational constants $\{\omega_e, \omega_e x_e, \ldots\}$ are obtained. Finally, the electronic component T_e is determined using the vibrational–rotational constants. Such a multistage procedure provides a nonoptimal set of the constants. Moreover, when the combination differences $\Delta_2'(J)$ and $\Delta_2''(J)$ are used, measurement errors for the wavenumbers of both lines completely appear in the term-difference error that enters twice: first, only for the lower vibronic state and, then, only for the upper state. In an appropriate procedure, this error should be divided between the errors of the upper and lower combining term values.

In view of these circumstances, a procedure for simultaneously determining the molecular constants for the upper and lower electronic states of the band system was developed in [4, 6]. This procedure reduces to solving an overdetermined system of equations that relate term values to wavenumbers (Rydberg–Ritz combination principle) and that are written for all rovibronic lines under investigation after the replacement of rovibronic term values in the equations by series that include the desired molecular constants of the upper and lower electronic states.

In works that were summarized in [5], rovibronic term values were proposed to be determined on the basis of the combination principle by solving the over-

determined system of equations on a computer. This method is one-step, but only one band system could be processed in view of limited computer capabilities at that time. As a result, the author of those works did not notice that, when transitions between many vibronic states were used, a relation between wavenumbers and absolute values of all rovibronic term values could appear in the system of equations (see below). For this reason, to determine the relative position of level groups that were uncoupled owing to the above-indicated cause, a polynomial approximation of the dependences of rovibronic term values on the rotational quantum number was again used in [5]. We emphasize that an attempt to directly obtain rovibronic term values in [5] was inconsistent from the very beginning. The rovibronic term values were treated as intermediate molecular parameters, and the procedure of their calculation was only one of the stages on the way from determining the positions of spectral lines on a photoplate to the set of the vibrational–rotational constants of various electronic states. In more recent work [9], Åslund left his initial position in favor of the "direct approach" [6].

Owing to the above disadvantages and difficulties of the actual realization of the combination difference method, this method is currently used only to interpret an unidentified spectrum, and then the sets of molecular constants are determined, which are used as the basic energy characteristics of diatomic molecules [2, 10]. An exception is presented by the rovibronic term values of the light molecules H_2 [7] and D_2 [8], which were obtained by jointly using combination differences and molecular constants.

The aim of this work is to develop a method for determining the optimal set of rovibronic term values from the wavenumbers measured for rovibronic spectral lines. This method does not require any assumptions about the properties of a molecule and it is based *only* on the Rydberg–Ritz combination principle whose validity and generality are out of doubt.

The main idea of the new method is that, if experimental data for all systems of bands are jointly used, the system of equations that, according to Rydberg–Ritz combination principle, relates wavenumbers to term values involves information on the absolute values of all rovibronic term values. Unfortunately, we cannot prove this statement in the general form. For this reason, we will demonstrate the existence of such a relation for an example that is illustrated in Fig. 2. As is seen, if it is possible to use experimental data on rovibronic lines that pairwise couple *three or more* vibronic states, then the combination differences can be constructed for triples of rovibronic spectral lines rather than for pairs of them, as is done in the standard approach [1]. In particular, the triples of spectral lines of the R and P branches that are shown in Fig. 2 make it possible to determine the differences between two neighboring rotational term values of the lower vibronic state. Thus, the above problem of the existence

of uncoupled level sets with even and odd rotational quantum numbers J disappears.

In the method proposed here, the weighted standard deviation of wavenumbers that are calculated using the Rydberg–Ritz combination principle from the wavenumbers measured for a sufficiently large number of rovibronic spectral lines of various systems of bands is minimized by varying the desired rovibronic term values. If the measurement errors for the wavenumbers are random and deviations have a normal distribution, the solution that is obtained in this way corresponds to the maximum likelihood principle [11]. Since the equations used in this method are linear, this optimization problem reduces to solving a system of linear algebraic equations.

According to the above consideration, the new method has the following differences from the available methods. First, no assumptions on the molecular structure are required. Second, this method does not involve intermediate parameters such as the molecular constants that are used in traditional methods [1, 4, 6, 9]. Third, all available experimental data that are obtained for different systems of bands by different authors in different works can be used in the one-step optimization procedure. Fourth, this method enables one to rationally select experimental data in the interactive mode, to exclude gross errors, to correct mistakes in identifying rovibronic lines, and to analyze the consistency of different data sets. Fifth, the distribution of experimental errors can be independently estimated. Sixth, this method provides not only the optimal values for rovibronic term values, but also accuracies of their determination that are caused only by the amount and quality of the available experimental data.

A necessary condition for the application of this method is the preidentification of rovibronic spectral lines, i.e., the determination of the correspondence between the observed rovibronic lines and particular rovibronic transitions. Hence, the standard methods for analyzing molecular spectra remain necessary. For this reason, the method proposed here is complimentary for the standard methods. However, since the new method is objective, any identification of an rovibronic spectrum is preliminary until it is not corroborated by the conclusion that rovibronic term values obtained by this method do not contradict the Rydberg–Ritz combination principle.

This method has an interesting feature that distinguishes it from methods using molecular constants. This feature refers to the situation where the wavenumbers of spectral lines from higher vibrational or rotational levels are measured after the spectrum has been analyzed and the final result has been obtained in the form of a set of the rovibronic term values or a set of the molecular constants of a certain electronic state.[2] Such expansion of
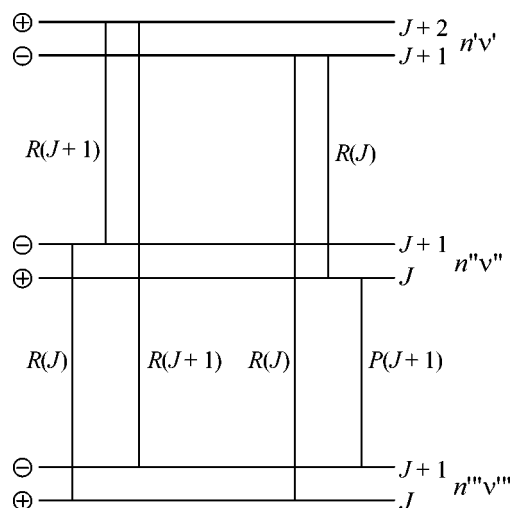
Fig. 2. Grotrian diagram that illustrates the possibility of determining the difference between two neighboring rotational term values by using the combination differences between the wavenumbers of triples of rovibronic spectral lines of the R and P branches. These lines correspond to transitions between the singlet states of a heteronuclear molecule; n', n'', and n''' denote electronic states; v', v'', and v''' are the vibrational quantum numbers; and the total angular momentum J is the rotational quantum number.

experimental data does not change the rovibronic term values that have been previously obtained by the method proposed in this work. This expansion only adds new, previously unknown term values. In this situation for traditional methods, the entire set of molecular constants should be recalculated.

For the sake of simplicity, Fig. 2 shows the case of singlet levels of a heteronuclear molecule. The consideration is evidently applicable to multiplet term values, but one more quantum number appears in the classification of energy levels and the corresponding selection rules appear for radiative transitions. A difficulty arises only in the absence of studied transitions between levels of different multiple orders, because the corresponding term sets are uncoupled with each other; i.e., they have different reference points.

For homonuclear molecules, a fundamental problem arises, because rotational levels with different parities have different symmetries with respect to the permutation of nuclei. Transitions between states with different nuclear symmetries are forbidden; hence, the set of rovibronic term values is divided into two independent sets (e.g., levels of ortho- and parahydrogen). If the difference between at least two term values with different symmetries cannot be determined experimentally, it is necessary to use some additional assumptions similar to those used in [5, 8].

At first glance, a disadvantage of the method proposed here is the relatively large amount of output data (hundreds or thousands of rovibronic term values instead of tens or hundreds of molecular constants in the standard approach). However, it is an insignificant

---

[2] We assume here that the lines corresponding to the transitions from lower levels have been previously measured with a sufficiently high accuracy. It is clear that, if new measurements indicate errors in previous measurements, both molecular constants and rovibronic term values should be recalculated.

demerit for two reasons. First, in any case, the number of calculated rovibronic term values is no more (usually several times less) than the number of the input wavenumbers of spectral lines whose tables are usually published in original papers. Second, at the current status of computers, databases, and networks, both transfer and processing of such information amounts are not difficult. At the same time, the output data provided by the new method carry all available information on rovibronic term values and any reduction in the data amount leads to loss of a certain part of this information.

This method has been applied to determine all rovibronic term values of all singlet electronic states of isotopomer $^{11}B^1H$ of the boron hydride molecule that have been already studied experimentally. They are $X^1\Sigma^+$, $A^1\Pi$, $C'^1\Delta$, $B^1\Sigma^+$, $C^1\Sigma^+$, $D^1\Pi$, $E^1\Sigma^+$, $F^1\Sigma^+$, $G^1\Pi$, $H^1\Delta$, $I^1\Sigma^+$, and $J^1\Sigma^+$. We used all available experimental data on the wavenumbers of rovibronic spectral lines belonging to 15 systems of bands. These experimental data were obtained in ten different works [12–21]. Analysis of these data showed that the results of different works agree fairly well with each other, excluding early works [12, 14], where systematic errors of about $0.05–0.10$ cm^{-1} have been revealed. All data from those two works were excluded from further analysis. Among the remaining 1410 wavenumbers, 32 wavenumbers were excluded as erroneous according to the 3σ rule. As a result, 529 values have been obtained for rovibronic term values of 12 electronic states of the BH molecule. The rovibronic term values with standard deviation were presented in [22], and the detailed description of this application of the method is beyond the scope of this report.

In conclusion, we emphasize that the new method enables one to empirically determine the set of rovibronic term values. This set is not associated with any concept of the molecular structure and it is optimal (the best among possible) in term values of both the maximum likelihood principle and the available experimental data. The values that are obtained for term values and their standard deviations are completely determined by the amount of available experimental data and measurement accuracy. Hence, the values that are obtained for rovibronic term values can be treated as secondary experimental data.

The most accurate experimental determination of the energy spectrum of diatomic molecules (rovibronic term set) is of interest both for molecular quantum mechanics (construction of model Hamiltonians, the possibility of the direct comparison of *ab initio* calculations with experimental data, etc.)[3] and for the spectroscopy of hot gases and plasma for the comparison of observed spectra with those simulated in the framework of certain models of physical processes of the excitation and deexcitation of rovibronic levels.

REFERENCES

1. G. Herzberg, *Molecular Spectra and Molecular Structure*, Vol. 1: *Spectra of Diatomic Molecules* (Van Nostrand, New York, 1959).

2. K. P. Huber and G. Herzberg, *Molecular Spectra and Molecular Structure*, Vol. 4: *Constants of Diatomic Molecules* (Van Nostrand Reinhold, New York, 1979; Mir, Moscow, 1984).

3. http://webbook.nist.gov/chemistry.

4. B. P. Lavrov, V. P. Prosikhin, and V. I. Ustimov, Izv. Vyssh. Uchebn. Zaved. **29** (2), 66 (1986).

5. N. Åslund, Ark. Fys. **30** (25), 377 (1965).

6. D. L. Albriton, W. J. Harrop, A. L. Schmeltekopf, *et al.*, J. Mol. Spectrosc. **46**, 67 (1973).

7. G. H. Dieke, J. Mol. Spectrosc. **2**, 494 (1958).

8. R. S. Freund, J. A. Schiavone, and H. M. Crosswhite, J. Phys. Chem. Ref. Data **14**, 235 (1985).

9. N. Åslund, J. Mol. Spectrosc. **50**, 424 (1974).

10. A. A. Radtsig and B. M. Smirnov, *Reference Data on Atoms, Molecules, and Ions* (Atomizdat, Moscow, 1980; Springer, Berlin, 1985).

11. D. J. Hudson, *Statistics. Lectures on Elementary Statistics and Probability* (Geneva, 1964; Mir, Moscow, 1970).

12. W. Lochte-Holtgreven and E. S. van der Vleugel, Z. Phys. **70**, 188 (1931).

13. S. F. Thunberg, Z. Phys. **100**, 471 (1936).

14. G. M. Almy and R. B. Horsfall, Phys. Rev. **51**, 491 (1937).

15. A. E. Douglas, Can. J. Res., Sect. A **19**, 27 (1941).

16. S. H. Bauer, G. Herzberg, and J. W. Johns, J. Mol. Spectrosc. **13**, 256 (1964).

17. J. W. Johns, F. A. Grimm, and R. F. Porter, J. Mol. Spectrosc. **22**, 435 (1967).

18. J. W. Johns and D. W. Lepard, J. Mol. Spectrosc. **55**, 374 (1975).

19. F. S. Pianalto, L. C. O'Brien, P. C. Keller, and P. F. Bernath, J. Mol. Spectrosc. **129**, 348 (1988).

20. W. T. M. L. Fernando and P. P. Bernath, J. Mol. Spectrosc. **145**, 329 (1991).

21. J. Clark, M. Konopka, L.-M. Zhang, and E. R. Grant, Chem. Phys. Lett. **340**, 45 (2001).

22. B. P. Lavrov and M. S. Ryazanov, physics/0504044.

23. A. I. Drachev, B. P. Lavrov, V. P. Prosikhin, and V. I. Ustimov, Khim. Fiz. **4**, 1011 (1985).

---

[3] At present, *ab initio* calculations are usually compared either with potential curves obtained semiempirically or with individual molecular constants, primarily with T_e, ω_e, and B_e. Such comparisons cannot be recognized as direct or complete, because methods of semiempirical determination of potential curves [23] are subjective and molecular constants are conventional [4].

Translated by R. Tyapaev

Topological Response of Inhomogeneous, Elliptically Polarized, Light Fields to Controlled Anisotropic Perturbations

R. I. Egorov*, V. G. Denisenko, and M. S. Soskin

Institute of Physics, National Academy of Sciences of Ukraine, pr. Nauki 144, Kiev, 03028 Ukraine
* e-mail: vbtar@iop.kiev.ua
Received March 21, 2005

The effect of controlled anisotropic losses on the topological structure of complex, elliptically polarized, light fields has been investigated. It has been shown that they can either initiate topological reactions with the appearance/disappearance of C points, saddle points, etc., or induce only their slight shift. Both strong and slight topological responses can be realized in the same field at sections with different inhomogeneity degrees of the polarization parameters of the field. © *2005 Pleiades Publishing, Inc.*

PACS numbers: 02.40.–k, 42.25.Ja, 42.30.Ma

Singular optics is a rapidly developing section of modern optics. It analyzes the properties of fields with optical singularities, i.e., points where one of the field parameters is degenerate [1]. Optical (phase) vortices of linearly polarized fields, where the amplitude is equal to zero and the phase is indefinite, are of particular interest. In this case, the wave front has the shape of a helicoid [2] and light beams have a number of new properties (see, e.g., [3, 4]). For elliptically polarized fields, the amplitude is never equal to zero, and singularities are polarized and occur at points where one of the polarization-ellipse parameters is degenerate. Among these points are C points, where the polarization is circular and the azimuth is indefinite, and L points, where the polarization is linear and the ellipticity sign (direction of rotation for the vector **E**) is indefinite. In a section of a beam, points with linear polarization form L lines, which separate field regions with right and left polarizations. The above-listed singularities, along with the extrema and saddle points of the azimuth distribution (intersection points of equiazimuth bifurcation lines) [5], form topological lattices representing the polarization structure of the wave front. Such topological lattices were measured for actual, elliptically polarized, speckle fields [6] by means of the advanced method of Stokes polarimetry [7]. By means of this method, all the morphological forms of the neighborhood of C points were measured [8]. These forms were predicted by theory [9].

In this work, using an example of topological lattices of speckle fields with inhomogeneous polarization, the stability of realized structures, which is one of the key problems of the topology of singular light fields [2], is experimentally analyzed.

Polarization singularities are defined as the geometrically limiting forms of the ellipse, i.e., the circle and straight-line segment. In this case, as was theoretically argued by Freund [10], any ellipse can be transformed into a circle or strength-line segment by means of oblique projection. A simple physical analogue of such a transformation is the weakening of one of the linear components in the basis of polarization ellipse decomposition. For an initial field with inhomogeneous polarization, such a transformation leads to various distortions of the polarization in its various points. Analysis of this distorted field can provide an estimate of the stability of its structure and the effect of distortions on different types of polarizations presented in it.

We study the elliptically polarized speckle field that is obtained after a multimode photon-crystal fiber [6]. The polarization structure of the field is analyzed by the modified method of Stokes polarimetry. In order to introduce controlled distortions of polarization, the setup is equipped with a thin glass plane–parallel plate that can be turned at a given angle to the beam axis. The experimental scheme is shown in Fig. 1.
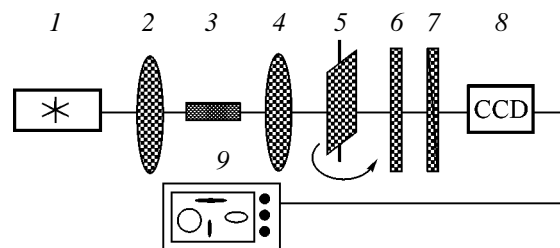

Fig. 1. Experimental setup layout: (*1*) the He–Ne laser ($\lambda = 633$ nm), (*2*) the lens focusing the beam on an object producing the speckle field, (*3* and *4*) the collimating lenses, (*5*) the plane–parallel glass plate, (*6*) the $\lambda/4$ phase plate, (*7*) the polarizer, (*8*) the CCD camera, and (*9*) the computer.
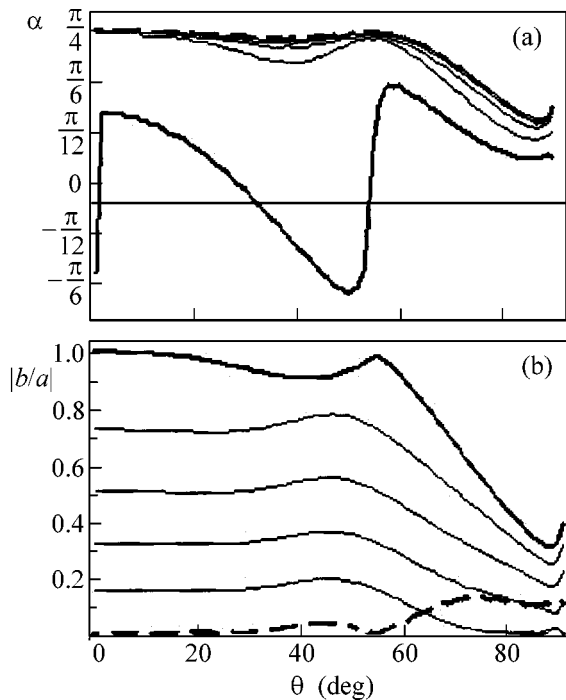
Fig. 2. (a) Azimuth α and (b) ellipticity |**b**/**a**| of the polarization of passing light vs. the plate inclination angle. The curves correspond to the input polarizations from (thick solid line) circular to (thick dashed line) linear with ellipticity values of 0, 0.16, 0.33, 0.51, 0.73, and 1 and an azimuth of π/4.

When the beam is incident on the glass plate, the polarization components parallel and perpendicular to the incidence plane, according to the Fresnel formulas, are reflected and transmitted differently [11]. The action of the plate on a homogeneously polarized beam is trivial: its polarization changes in a known manner.

However, since the incident beam has inhomogeneous polarization, $E_\parallel$ and $E_\perp$ are different at different points of its section. Therefore, distortions at these points are different, although the plate is uniform. Correspondingly, the polarizations at different points in the beam section change differently.

Figure 2 illustrates the effect of the rotation of the plate on different polarizations presented in the field under investigation. The passage of light through the plate is simulated with the inclusion of single reflection inside the plate and interference between the passed and reflected rays. This effect significantly affects the polarization of the resulting beam.

As is seen in the plots, changes in the polarization azimuth are maximal at beam points with circular polarization. Distortions of the azimuth at points with the elliptic polarization are comparatively small. The angular dependence of ellipticity indicates that, as the rotation angle of the plate increases, the circularly and linearly polarized points become elliptically polarized. The dependences of the polarization parameters are

substantially nonmonotonic. For certain angles of incidence, the incident beams with circular (linear) polarization again become circularly (linearly) polarized.

The polarization structure in the section of the inhomogeneously polarized beam can be well represented in terms of the topological lattice of the field [7]. Figure 3a shows a fragment of such a lattice. It consists of C points of different types [8] and equiazimuth bifurcation lines passing through saddle points. The white–grey background is the distribution of clockwise and anticlockwise rotating polarizations. According to the loop rule [5, 6], the extrema of the azimuth distribution are located within the loops of bifurcation lines.

In a coherent field, neighboring points are phase correlated. Therefore, field distortion that changes one element of the lattice leads to its complete rearrangement.

Changes that are induced in the topological lattice by the inclination of the plate clearly demonstrate changes in the polarization structure of the passed beam. Such changes are considered as the topological response of the field to introduced distortions. Experimental results are shown in Fig. 3.

According to Fig. 3, the topological response of the field to introduced distortions can be of two types. The first type is strong and it is accompanied by the rearrangement of the lattice due to topological reactions with the disappearance of certain elements or appearance of new elements. In particular, as is seen in Figs. 3a, 3b, and 3c, the number of extrema (inside loops) and saddle points of the azimuthal distribution changes from (a) 1/1 in the initial field to (b) 2/2 and, finally, to (c) their complete annihilation. In all the reactions, the total Poincaré–Hopf index is conserved. This index for extrema, saddle points, and C points is equal to [2, 5]

$$\eta_{extr} = +1, \quad \eta_{sad} = -1, \quad \eta_C = \pm\frac{1}{2};$$

respectively. The second type of the topological response is slight and it is accompanied only by a small shift of the elements of the lattice without a change in their number and types.

Both types of the response can be realized in different sections of the same field. The response type at each point is determined by the inhomogeneity degree of the initial-field polarization at this point.

According to the plate-effect model shown in Fig. 2, distortion is calculated for the initial field experimentally obtained for various inclination angles of the plate. The simulation results closely correlate with the experimental distributions.

In conclusion, we note that the effect of controlled perturbations on the topological structure of inhomogeneous, elliptically polarized light fields has been investigated. The mathematical-model prediction that different polarizations have different sensitivities to introduced distortions is experimentally corroborated.
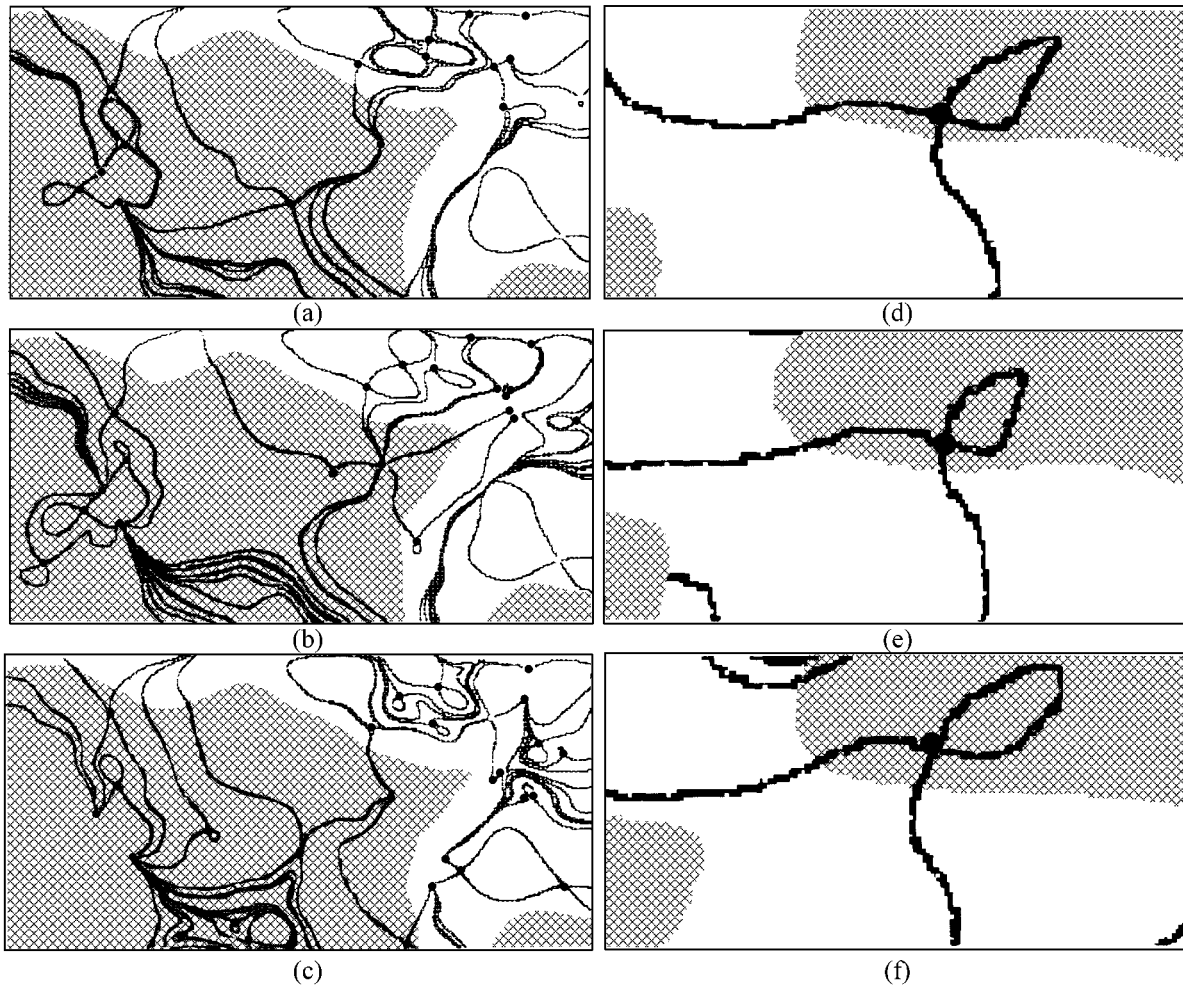
Fig. 3. Distortions that are induced in the polarization structure of an inhomogeneously polarized field by the inclination of the refracting plate: (a), (b), and (c) are the topological lattices for the field region with a strong topological response to distortion and (d), (e), and (f) are the topological lattices for the field region with a slight topological response (for inclination angles of 0°, 10°, and 20°, respectively, for different scales). The grey and dark grey background regions show the distribution of the right and left polarizations, respectively, and the boundary between them is an L line. The open asterisks, diamonds, and triangles are C points of different types, and the open squares are saddle points of the azimuthal distribution. The black lines are equiazimuth bifurcation lines.

C points are most sensitive to these distortions in the region of plate-inclination angles that are smaller than the Brewster angle. Then, sensitivity decreases with ellipticity.

We are grateful to Prof. I. Freund (Bar-Ilan University, Israel) for stimulating discussions.

REFERENCES

1. M. S. Soskin and M. V. Vasnetsov, Prog. Opt. **41**, 219 (2001).

2. J. F. Nye, *Natural Focusing and the Fine Structure of Light* (Inst. of Physics, Bristol, 1999).

3. M. V. Berry and J. H. Hannay, J. Phys. A: Math. Gen. **10**, 1809 (1977).

4. *Horizons in World Physics*, Vol. 228: *Optical Vortices*, Ed. by M. Vasnetsov and K. Staliunas (Nova Sci., Huntington, 1999).

5. I. Freund, M. Soskin, and A. Mokhun, Opt. Commun. **208**, 223 (2002).

6. M. Soskin, V. Denisenko, and R. Egorov, J. Opt. A: Pure Appl. Opt. **6**, S281 (2004).

7. M. Soskin, V. Denisenko, and I. Freund, Opt. Lett. **28**, 1475 (2003).

8. V. G. Denisenko, R. I. Egorov, and M. S. Soskin, Pis'ma Zh. Éksp. Teor. Fiz. **80**, 21 (2004) [JETP Lett. **80**, 17 (2004)].

9. M. Dennis, Opt. Commun. **213**, 201 (2002).

10. I. Freund, Opt. Lett. **29**, 1715 (2004).

11. M. Born and E. Wolf, *Principles of Optics*, 6th ed. (Pergamon, New York, 1986; Nauka, Moscow, 1973).

Translated by R. Tyapaev

Study of the Energy Release Region of a Heavy-Ion Flux in Nanomaterials by X-ray Spectroscopy of Multicharged Ions

V. P. Efremov[1], S. A. Pikuz, Jr.[1], A. Ya. Faenov[2], O. Rosmej[3], I. Yu. Skobelev[2], A. V. Shutov[4], D. H. H. Hoffmann[3], and V. E. Fortov[1]

*[1] Joint Institute for High Temperatures Research, Russian Academy of Sciences,
Izhorskaya ul. 13/19, Moscow, 127412 Russia*
e-mail: pikuz@mem3.phys.msu.ru
[2] Multicharged Ion Spectra Data Center, NPO VNIIFTRI, Mendeleevo, Moscow region, 141570 Russia
[3] Gesellschaft für Schwerionenfoschung, D-64291 Darmstadt, Germany
*[4] Institute of Problems of Chemical Physics, Russian Academy of Sciences,
Chernogolovka, Moscow region, 142432 Russia*
Received March 15, 2005

X-ray spectroscopic data are reported on the state of a silicon aerogel medium (SiO_2) irradiated by a Ni ion flux with an energy of 4.7 MeV/nucleon. Radiation from the electron transitions to the K shell in multicharged Si ions is detected with spatial resolution along the direction of the beam propagation in the medium. Calculations performed for the ionization state and population of the levels excited in the silicon atoms of the target provide the estimate $T_e = 70$–120 eV for the medium electron temperature in the ion tack region. Two-dimensional hydrodynamic calculations provide the estimate $T_e = 60$–116 eV for the same conditions and densities of 0.5–2.5 g/cm^3 of the excited target medium. © 2005 Pleiades Publishing, Inc.

PACS numbers: 32.30.Rj, 52.25.–b, 52.50.Gj, 52.65.–y

1. The interaction of fast heavy ions with condensed matter leads to the formation of tracks in solids (see, e.g., reviews [1, 2]). The transverse size of a track is much larger than the diameter of an ion itself, which indicates the existence of high stress that exceeds the yield strength of the material even quite far from the track axis.

Numerical simulation that was performed in [3] showed that the velocity and energy release in a solid are so high that a plasma with a temperature of about several hundred electronvolts, a pressure of several tens of megabars, and solid density is formed in the interaction region in the first several femtoseconds after the passage of an ion. However, the available diagnostic methods cannot usually provide measurement of the thermophysical parameters in the energy release region immediately after the passage of heavy ions through matter, because all processes proceed in such a plasma with a very high rate and satellite electromagnetic noise is generated. Therefore, experimental information on the pressure, temperature, and charge state of the medium in the energy release region can significantly improve the determination of the parameters of perturbations generated in the target medium (these perturbations are usually thermal and shock waves that propagate in the target). Moreover, this information can assist in both the adequate theoretical description of the medium state at the initial instant of the track formation and calculation of the final sizes of the formed tracks in dependence on the parameters of incident ions and the target material.

In recent years, the action of pulsed energy fluxes (electron or ion beams and laser beams) on matter has been studied with porous (spatially inhomogeneous) targets consisting of solid particles (clusters) whose size can vary from several to several hundreds of nanometers [4–8]. Such porous media are absorbed energy only in high-density target regions. In this case, the length of the energy release region increases, which can be used for both detailed investigation of the particle free path and development of models of the behavior of the porous medium. The features of nanostructure targets can be completely manifested if the duration τ of the interacting energy flux (e.g., the duration of a femtosecond laser pulse or relativistic heavy ion beam) lies in the subpicosecond range and does not exceed the time of the gas-dynamic scattering of the nanoparticle. In other words, if the pulse duration τ in the irradiation process satisfies the condition $\tau \ll R/C(T)$, where $C(T)$ is the volume speed of sound and R is the radius of the nanoparticle, the isochoric heating of the nanoparticle occurs and a solid-density plasma is formed if the intensity of the radiation is sufficient [9, 10].

When using subrelativistic ion beams, the time of their interaction with dense objects (clusters) of the porous medium is much less than the time of the hydrodynamic scattering of such regions (the time of the passage of an ion through condensed matter—an aerogel

particle with a size of 1–10 nm—is equal to 0.05–0.5 fs). In other words, the unloaded target plasma arising after the passage of the ion has a solid density. If the total intensity of the incident beam is low, each subsequent ion of the beam interacts with the relaxed medium.

In this work, we study the plasma formed when a 4.7-MeV/nucleon nickel ion beam interacts with a porous SiO_2 target (aerogel). The method of x-ray spectroscopy with spatial resolution [11] provided the determination of the state of the aerogel target in the process of its interaction with Ni ions. A similar method was previously applied to identify the state of the ions of a beam propagating in a solid medium [12, 13].

2. Experiments were carried out at the UNILAC linear accelerator of heavy ions at GSI, Darmstadt, Germany. Figure 1a shows the layout of the experiment. The interaction of Ni^{+14} ions with SiO_2 aerogel targets with a density of 0.04 g/cm^3 in a vacuum chamber at a residual pressure of 10^{-6} mbar was studied. The aerogel target was a porous material that was formed by chains of SiO_2 grains each 4 nm in size. The total thickness of the target was taken from the condition of the complete stop of the ion beam in it. Ions with an energy of 4.7 MeV/nucleon ($v/c \approx 0.1$) were focused onto a spot 1–2 mm in diameter at the edge of the target whose position was controlled by an accurate manipulator. The beam intensity varied in the range 0.2–0.5 µA, and the exposition time was 2–3 h. A low average beam current statistically specifies the ion separation time ~10 ps. In this case, the probability of the hit of two ions into one grain in a time interval shorter than the plasma scattering time is negligibly small and the entire process can be treated as the heating of the grain by a single high-energy charged particle.

The x-ray spectra in the range 6.1–7.3 Å were detected by a spectrograph with a spherically bent quartz crystal $10(-1)0$ ($2d = 8.512$ Å) with the curvature radius $R = 100$ mm and a 10×28-mm working region. X-ray radiation was fixed on a DEF Kodak film. The film was protected from visible and ultraviolet radiation by two layers of a polypropylene film that is 1 µm thick and covered by a 0.2-µm aluminum layer. The dispersion scheme was adjusted for the work in the first and fourth reflection orders, which enabled one to simultaneously observe the He_α line and its dielectronic satellites (up to the K_α line of the neutral atom) of multicharged ions Si (target radiation) and Ni (incident heavy ions). The spectra were detected with one-dimensional resolution, and the direction of the propagation of the incident heavy-ion beam inside the target lied in the spatial resolution plane (see Fig. 1a).

Figure 1b shows typical radiation spectra from the SiO_2 aerogel target with a density of 0.04 g/cm^3 and Ni ions with an initial energy of 4.7 MeV/nucleon at various distances during the interaction of incident ions. The observed spectra contain dielectronic satellites of
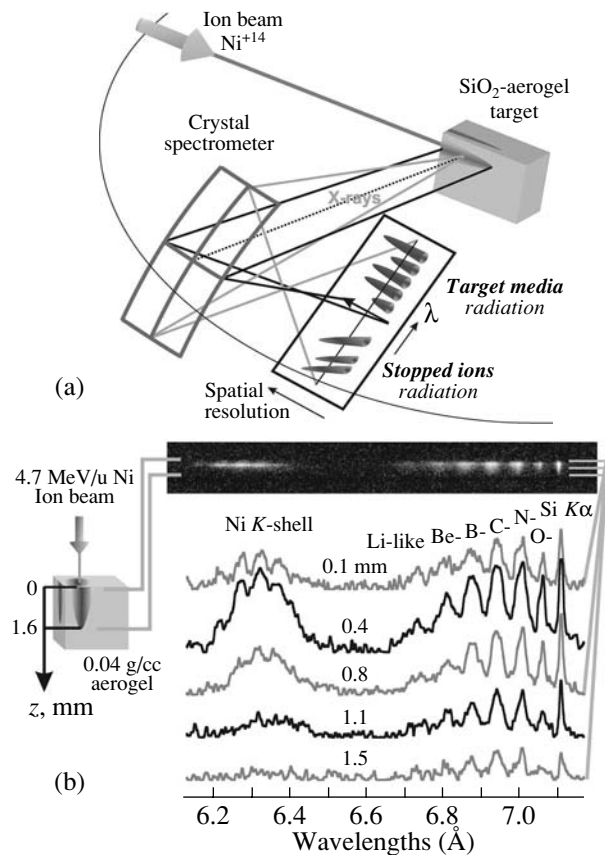

Fig. 1. (a) Layout of the experiment and (b) the spectrum of the radiation of the SiO_2 aerogel target with a density of 0.04 g/cm^3 and Ni ions with an initial energy of 4.7 MeV/nucleon.

the $2p–1s$ transition in Si ions with various ionization degrees. It is clearly seen that, although the energy fluxes of the incident ions are very low, the target radiation spectrum contains spectral lines corresponding to transitions in multicharged ions up to Li-like ions and the mean charge of Si ions in the formed plasma is equal to 9. As is seen in Fig. 1b, in addition to the spectra from target ions, the spectra of transitions to the K shell in the beam ions were detected and they were shifted toward longer wavelengths due to the Doppler effect (for more details, see [12, 13]). This circumstance allows the comparative analysis of the integral radiation intensity from ions of both the target and beam.

As is seen in Fig. 1b, the luminosity of the incident ions decreases faster than that of the excited medium. The ion content of the target changes significantly towards a higher ionization degree as the incident ion losses its energy (see Fig. 2). At the beginning of the target, where the Ni ion has the maximum energy (the energy release to the target is minimal), the concentration of more ionized Be-like Si ions is minimal compared to much less ionized O-like ions. As the Ni ion penetrating into the target losses its energy (the energy
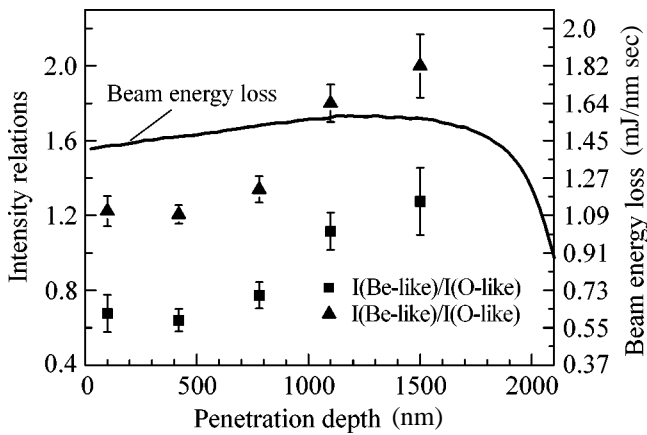
Fig. 2. Energy losses of the ion beam in the medium (calculated by the SRIM code) and measured ratios of the intensities of the spectral lines of the radiation of O-, C-, and Be-like ions of the Si target vs. the penetration depth of ions into the 0.04-g/cm^3 aerogel.
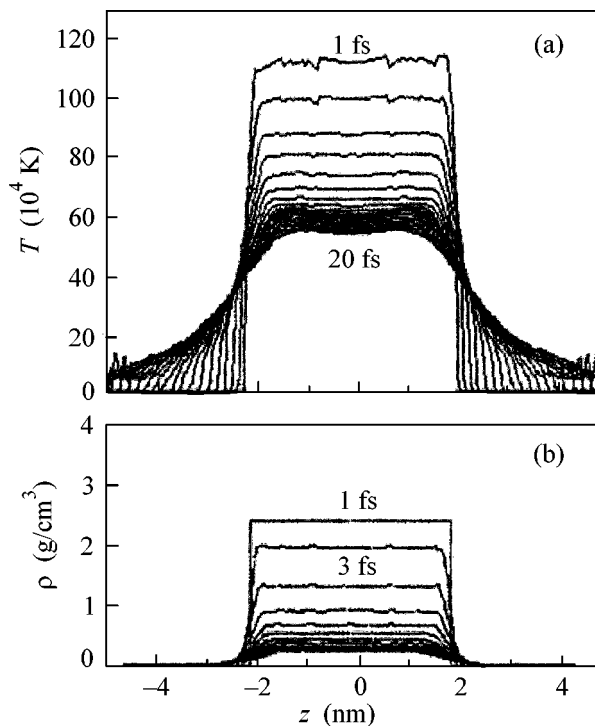

Fig. 3. (a) Electron temperature and (b) density that are calculated for the quartz aerogel target along the Ni-ion trajectory for first 20 fs after the ion passage with a step of 1 fs.

release to the target increases, see Fig. 2), this relation changes and the concentration of Be-like Si ions becomes higher than the concentration of O-like ions. As is seen in this figure, the concentration of C-like ions in the target changes similarly.

The energy losses of the beam penetrating into the target is calculated by the SRIM code (The Stopping and Range of Ions in Matter) [14] based on the Bethe–Bohr–Bloch equation

$$-\frac{dE}{dx} = \frac{4\rho Z_{\mathrm{eff}}^2 e^4}{m v^2} \frac{c c (Z - y)}{A m_A} (L_{\mathrm{be}} - \ln(1 - \beta^2) - \beta^2).$$

Here, m and e are the mass and charge of the electron, respectively; Z_{eff} and v are the effective charge number and velocity of the incident ion, respectively; $\beta = v/c$, where c is the speed of light; A, Z, and y are the mass number, atomic number, and ionization degree of the atoms of the medium, respectively; $Z - y$ is the number of bound electrons per atom of the medium; ρ is the volume density of the target; m_A is the atomic mass unit; and L_{be} is the Coulomb logarithm for bound electrons.

The comparative analysis of the above data provides the conclusion that an increase in the ionization degree of the target ions can be attributed to an increase in the energy release of the Ni ion per unit volume of the medium when its energy decreases from 4.7 to 1 MeV/nucleon. Below, the observed spectra will be treated in terms of the pulse energy excitation and relaxation of the nanometer region of the ion track in the medium in a characteristic time of several femtoseconds.

3. The entire process investigated in the experiments can be divided in time into the following elementary physical processes: the time of flight (~0.2 fs) of the ion (energy release time) through the particle of the aerogel ($d = 4$ nm); the K_α transition time (1 fs) for the Si ion of the target; the time (~50 fs) of the K_α-transition satellite in O-, N-, C-, B-, Be-, and Li-like Si ions of the target; the time (~20 fs) of the existence of ultrahigh pressure in the silicon particle; and the time (10 ps) between actions of single ions on the volume under investigation.

As is seen from the above data, each ion really interacts with an unchanged medium and the observed parameters of the radiation of the medium can be associated with the interaction of a single ion with solid sections of the target. Using the hydrodynamic code developed in [3], we performed two-dimensional calculations of the time evolution of the density and temperature for the interaction of the Ni ion with aerogel particles (SiO$_2$ balls 4 nm in diameter).

Figure 3 shows the results of these calculations. The energy losses of the incident beam ion in quartz was estimated by the SRIM code [14]. It was assumed [2] that the entire energy of the ion in quartz is instantaneously released in a small cylindrical region with radius R (nm) along the rectilinear trajectory of the ion that passes through the center of the target. In this case,

the power contribution W of the ion is distributed over the cylinder radius according to the Gaussian

$$W = \begin{cases} 0, & \text{for } R > 3, \\ W_{max}\left(\exp\left(-\dfrac{R^2}{2(0.15)^2}\right)\right), & \text{for } 0 < R < 3. \end{cases}$$

As is seen in Fig. 3, the electron temperature of the plasma at the initial time reaches 110 eV for the solid density of the formed plasma. This result was obtained under the assumptions that the entire energy of the incident ion is initially transferred to the electron ensemble and that the equilibrium temperature of the medium corresponds to the electron temperature.

It is seen that the sufficiently dense and hot plasma exists for several tens of femtoseconds. At the same time, according to the calculations, the maximum specific energy released in such an aerogel particle reaches giant values up to 8000 kJ/g, the maximum pressure reaches 6000 GPa, and the maximum velocity of the scattering of the ball-medium plasma along the ion trajectory reaches 170 km/s. These data indicate that the passage of a single heavy ion through the aerogel target is accompanied by the formation of a unique solid-state plasma whose parameters are comparable with the parameters of the plasma formed when an ultrahigh-power femtosecond laser pulse interacts with aerogel or cluster targets.

4. The comparison of spectra shown in Fig. 1b with the results of the simple model calculation enables one to estimate the temperature of the plasma formed when the ion beam interacts with solid grains of the aerogel. When SiO_2 molecules, whose concentration in the grains is equal to 2.23×10^{22} cm^{-3}, are ionized to the observed degrees, the electron concentration in the plasma reaches 4.7×10^{23} cm^{-3}. This concentration is sufficient to apply the Saha–Boltzmann distribution to describe the ionization state and populations of the excited states of ions in the plasma (see, e.g., [15–17]). In this case, the distribution of ions over the excited levels is a Boltzmann distribution, $N_k/N_0 = g_k/g_0\exp((E_0 - E_k)/kT_e)$. The multiplicity distribution is given by the Saha formula $N^{(Z+1)}/N^{(Z)} = g_{Z+1}/g_Z 2(mkT_e/2\pi\hbar^2)^{3/2}1/N_e\exp(-E_Z/kT_e)$, where N_k (N_0), g_k (g_0), and E_k (E_0) are the population, statistical weight, and energy of the kth excited (ground) level, respectively; kT_e is the electron temperature of the plasma; $N^{(Z)}$, g_Z, and E_Z are the population, statistical weight, and ionization energy of the ion Z; and N_e is the electron concentration. According to the above formulas, the spectrum emitted by the medium depends only on the electron temperature T_e of the plasma.

The spectra of the dielectric satellites that were calculated using the atomic constants [18] are shown in Fig. 4a for various T_e values and a natural linewidth of 7.7 mÅ. As is seen in this figure, the radiation spectrum
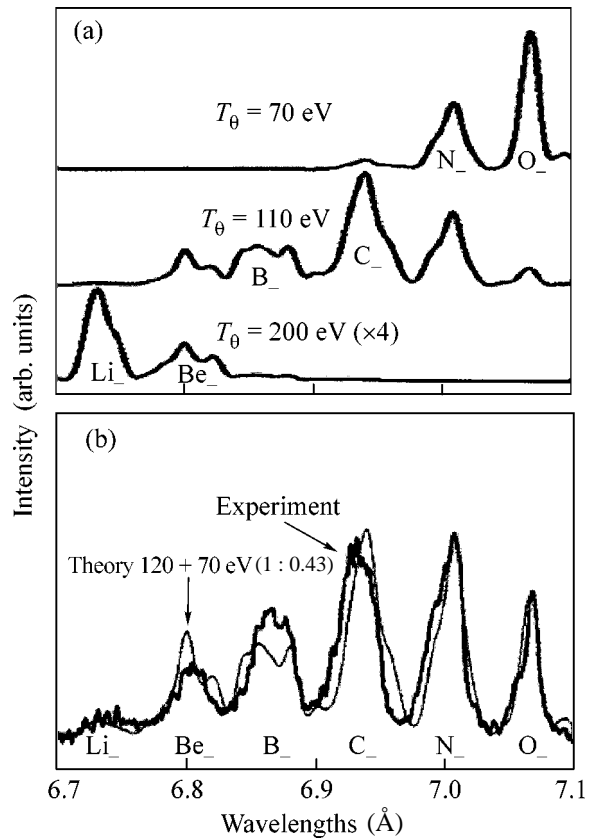

Fig. 4. (a) Spectra of the dielectronic satellites of Si ions as calculated for various T_e values and a natural linewidth of ~7.7 mÅ and (b) experimental and model spectra of the radiation of the aerogel-target plasma in the wavelength range 6.7–7.1 Å.

for temperatures below 100 eV consists primarily of the satellite lines associated with transitions in O-, C-, and N-like Si ions. At the same time, for $T_e > 150$ eV, the intensity is maximal for the Li- and Be-like satellites. In the real situation, the plasmas that are formed in different grains, where an incident ion interacts with their different parts, are expected to have different temperatures. Since the observed spectrum is the integral of the luminosity over the spectrometer detection ray, it is a superposition of several spectra calculated for various T_e values. The experimental spectra appear to be well reproduced by the two-temperature approximation. The experimental spectrum shown in Fig. 4b is well approximated by the sum of two spectra for the temperatures 120 and 70 eV and the weight factors 1 and 0.43. The small discrepancy for most highly charged Be- and B-like ions is likely explained by the fact that the ionization time 0.2 ps for the B-like Si ion at $T_e = 120$ eV and $N_e = 4.7 \times 10^{23}$ cm^{-3} is slightly larger than the decay time of the local plasma, and, as a result, the concentrations of Be- and B-like ions are slightly lower and higher, respectively, than the respective equilibrium values. The plasma parameters ($T_e = 120$ eV and

$N_e = 4.7 \times 10^{23}$ cm^{-3}) thus determined are certainly characteristic only for local aerogel-target regions, where heavy ions give rise to the formation of such extremal states of the medium with a relatively low total energy contribution. The conservation of the macrostructure of the aerogel for several hours of its interaction with the ion beam also indicates that the mean temperature of the medium is sufficiently low.

5. Thus, using the results of the above investigations, we propose the method for detecting the charge state of the condensed-target medium along the track of a heavy ion. The use of nanostructure media as targets allowed the detection of the evolution of the velocity and charged state of the ion along the track. The simultaneous detection of the K_α satellites of the target can both increase the reliability of the detection of the evolution of the incident ion and provide experimental information on the states of the near zone of the medium adjacent to the deceleration track of heavy ions at the first instants after such interaction. Two-dimensional calculations of the time evolution of the density and temperature of the target medium where the Ni ion interacts with aerogel particles (SiO$_2$ balls 4 nm in diameter) show that a solid plasma with a temperature of several tens of electronvolts is formed in first several femtoseconds after the passage of the ion through the target. These values are qualitatively consistent with the experimental data on the temperature that were obtained from the x-ray spectra of the target. However, further improvement is required for both the model for calculating the interaction of heavy ions with the medium and the models for describing the emission of x-ray spectra detected from the region of the interaction of heavy ions with the medium.

REFERENCES

1. A. M. Mitereev, Usp. Fiz. Nauk **172**, 1131 (2002) [Phys. Usp. **45**, 1019 (2002)].
2. F. F. Komarov, Usp. Fiz. Nauk **173**, 1287 (2003) [Phys. Usp. **46**, 1253 (2003)].
3. A. V. Shutov, V. E. Fortov, and I. V. Lomonosov, in *Physics of Extremal States of a Material* (Chernogolovka, 2004), p. 149 [in Russian].
4. T. Ditmire, J. Zweiback, V. P. Yanovsky, *et al.*, Nature **398**, 489 (1999).
5. V. V. Gavrilov, A. Yu. Gol'tsov, N. G. Koval'skiĭ, *et al.*, Kvantovaya Élektron. (Moscow) **31**, 1071 (2001).
6. I. Yu. Skobelev, A. Ya. Faenov, A. I. Magunov, *et al.*, Zh. Éksp. Teor. Fiz. **121**, 88 (2002) [JETP **94**, 73 (2002)].
7. Y. Fukuda, Y. Akahane, M. Aoyama, *et al.*, JETP Lett. **78**, 115 (2003).
8. K. B. Fournier, C. Constantin, J. Poco, *et al.*, Phys. Rev. Lett. **92**, 165005 (2004).
9. J. Abdallah, Jr., G. Csanak, Y. Fukuda, *et al.*, Phys. Rev. A **68**, 063201 (2003).
10. A. Ya. Faenov, T. A. Pikuz, I. Yu. Skobelev, *et al.*, Pis'ma Zh. Éksp. Teor. Fiz. **80**, 860 (2004) [JETP Lett. **80**, 730 (2004)].
11. O. N. Rosmej, J. Wieser, M. Geissel, *et al.*, Nucl. Instrum. Methods Phys. Res. A **495**, 29 (2002).
12. O. N. Rosmej, S. A. Pikuz, Jr., S. A. Magnitskii, *et al.*, JETP Lett. **78**, 374 (2003).
13. O. N. Rosmej, S. A. Pikuz, Jr., J. Wieser, *et al.*, Rev. Sci. Instrum. **74**, 5039 (2003).
14. http://www.srim.org.
15. E. E. Fill, Phys. Rev. Lett. **56**, 1687 (1986).
16. T. Fujimoto and R. W. P. McWhirter, Phys. Rev. A **42**, 6588 (1990).
17. Yu. A. Fadeev and D. Gillet, Astron. Astrophys. **354**, 349 (2000).
18. A. Ya. Faenov, S. A. Pikuz, and A. S. Shlyaptseva, Phys. Scr. **49**, 41 (1994).

Translated by R. Tyapaev

Instability of Interstitial Dislocation Loops in Electron-Irradiated Dielectrics

A. I. Ryazanov and A. V. Klaptsov

Russian Research Center Kurchatov Institute, pl. Akademika Kurchatova 1, Moscow, 123182 Russia
e-mail: ryazanoff@comail.ru
Received March 15, 2005

The experiments on electron irradiation of yttrium-stabilized zirconium oxide samples show the formation of strong elastic fields near interstitial dislocation loops. The fields increase with an increase in the loop radius and, when the loop radius reaches a certain critical value, the loops became unstable due to the beginning of plastic deformation and the formation of a dislocation network. The mechanism of the occurrence of this instability is suggested. It is based on the accumulation of charges at dislocation loops due to ionization processes in an electron-irradiated dielectric. It is shown that the accumulation of the electric charge at growing dislocation loops in dielectrics may be responsible for an increase in elastic stresses near dislocation loops and for their instability because of the beginning of plastic deformation near the loops when stresses at growing loops become close to the theoretical yield stress of the material. © 2005 Pleiades Publishing, Inc.

PACS numbers: 61.72.Cc, 61.80.Az, 61.82.Ms

Various ceramic materials are planned to be used as elements of the construction materials for the first wall of future thermonuclear reactors. Therefore, it is important to study the effect of high-energy radiation on their microstructure and the stability of their physical and mechanical properties. The radiation resistance of these materials is determined by the accumulation rate of radiation-induced point defects in the matrix and the kinetics of formation of clusters of point defects (dislocation loops, pores, etc.) and their subsequent growth in these materials. In distinction from irradiation of metals, irradiation of ceramic materials may give rise to the formation of charged states at point defects. The charges may considerably change the kinetics of the nucleation and growth of point-defect clusters in ceramic materials and, thus, change their physical and mechanical properties.

The previous experimental studies showed that yttrium-stabilized cubic zirconium oxide, which is a ceramic material, is highly radiation resistant especially to radiation swelling [1–3]. However, transmission electron microscopy [4–6] of yttrium-stabilized cubic zirconium oxide samples that were preliminarily irradiated with 100-keV He$^+$ and 300-keV O$^+$ ions and then irradiated with 100–1000-keV electrons at a flux of 1.5×10^{23} e/m^2 showed the anomalous formation of defect clusters and their subsequent growth. The regions around defect clusters showed considerable deformation contrasts indicating the existence of pronounced elastic stresses near these clusters. The deformation contrasts increased with the cluster size and was maximal at a critical cluster size of about 1.0–1.5 μm. Defect clusters that reached the critical size became unstable with respect to the initiation of plastic deformation and the formation of a dislocation network near these clusters (see figure).

Changes in the microstructure and the formation of point-defect clusters in the irradiated cubic zirconium oxide samples are determined by the generation rate of point defects (interstitial atoms and vacancies) and their diffusion mobility in the matrix. The overwhelming majority of point defects that are formed in cubic zirconium oxide irradiated with 0.1–1 MeV electrons are interstitial oxygen atoms and vacancies in the lattice. This circumstance is explained, first, by the considerable difference between the atomic masses of zirconium and oxygen and, second, by the fact that the energy $E_d^O = 20$ eV necessary for the displacement of light oxygen atoms from their sites in the lattice is lower than the corresponding energy $E_d^{Zr} = 40$ eV for zirconium atoms. Therefore, in the electron-irradiated cubic zirconium oxide samples, the cross section σ^O for the displacement of oxygen atoms due to elastic collisions with fast electrons is much larger that the corresponding cross section σ^{Zr} for zirconium atoms ($\sigma^O \gg \sigma^{Zr}$). In particular, the calculations show [7] that the cross section for the displacement of oxygen and zirconium atoms at an incident-electron energy of 1.09 MeV are equal to $\sigma^O = 36$ b and $\sigma^{Zr} = 4.23$ b, respectively. The effective charge of interstitial oxygen atoms in cubic zirconium oxide is equal to –2 [8]. At the same time, the interstitial atoms may loose some electrons in diffusion jumps and become neutral. As a result, neutral interstitial oxygen atoms are involved in the nucleation
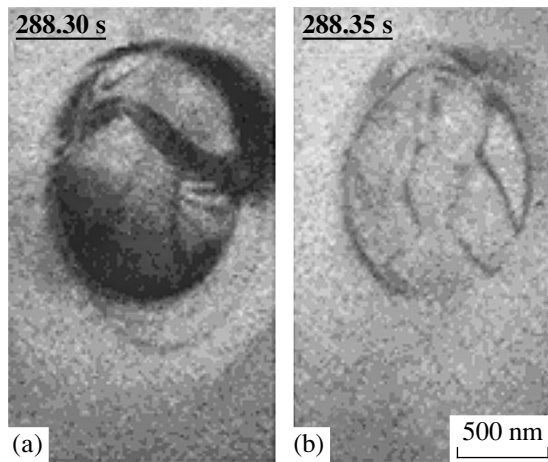
Fig. 1. Spontaneous transformation of (a) a charged dislocation loop with high elastic stresses into (b) a dislocation network owing to plastic deformation at the critical loop radius $R = 600$ nm in an yttrium-stabilized cubic zirconium oxide sample irradiated with 200-keV electrons at 470 K. The samples were preliminarily irradiated with 300-keV O^+ ions at a temperature of 470 K up to 5.1×10^{17} O^+/m^2 [6].

and growth of interstitial dislocation loops in yttrium-stabilized cubic zirconium oxide.

There is a reasonable question: what gives rise to such strong elastic stresses near dislocation loops during their growth and to the observed instability of these loops in the zirconium oxide samples. It was assumed in [4, 6] that pronounced deformations near dislocation loops were caused by the appearance of an electrostatic charge at these loops. Thus, the instability of the dislocation loops is explained by the accumulation of electric charge at these loops. This charge increases the elastic stresses in the vicinity of the loop owing to the material polarization until these stresses reach, e.g., the theoretical yield point σ_S, after which the plastic deformation near these loops becomes possible. Therefore, the instability of a dislocation loop may arise at the moment when the elastic stresses σ reach the value σ_S ($\sigma > \sigma_S$). At the same time, there is the question about the cause of the accumulation of the electrostatic charge Q at the dislocation loop in dielectrics irradiated with high-energy particles. Below, we suggest the mechanism of charge accumulation in electron-irradiated dielectrics owing to the knocking-out of electrons from the interstitial atoms of dislocation loops. It is shown that, even in the crudest approximation, the critical elastic stresses near dislocation loops ($\sigma \approx \sigma_S$) are reached even in a relatively low electron flux. Therefore, despite all possible relaxation processes, this mechanism may result in the instability of growing dislocation loops in electron-irradiated zirconium oxide samples.

The experimental results show that the dislocation loops in yttrium-stabilized zirconium oxide samples are

formed at the periphery of the electron beam, i.e., in the region where the electron flux is rather low and the temperature is moderate. Since, as was mentioned above, only oxygen atoms are mainly displaced in the crystal lattice, the irradiation-induced growth of dislocation loops proceeds only because of the diffusion-induced accumulation of interstitial oxygen atoms at these loops.

The incident electrons knock out electrons from both the matrix and interstitial atoms of the dislocation loops. Obviously, the holes thus formed in the irradiated matrix exist for the electron–hole recombination time, whereas ionized interstitial atoms exist for the electron diffusion time. The latter process is much more slower and results in the accumulation of a charge at dislocation loops. Now, we consider the extremal case where ionized interstitial atoms exist and create a certain charge at the loops for the characteristic times of dislocation-loop growth. An interstitial dislocation loop under an electron beam consists of N_n neutral and N_c charged interstitial atoms. Thus, the total number of interstitial atoms in the loops is

$$N_{tot} = \frac{\pi R^2}{a^2} = N_c + N_n. \tag{1}$$

The number of charged interstitial atoms in the dislocation loop increases because of the ionization of neutral atoms irradiated with fast electrons. If relaxation processes are ignored, the rate of charge accumulation at the dislocation loop may be written as

$$e\frac{dN_c}{dt} = \frac{dQ}{dt} = N_n \langle \sigma \rangle_I \Phi, \tag{2}$$

where R is the dislocation-loop radius, a is the lattice parameter, $\langle \sigma \rangle_I$ is the average cross section for the scattering of incident fast electrons with energies higher than the ionization energy by the electrons of interstitial atoms, Φ is the flux of incident electrons, and e is the elementary charge. The number of neutral interstitial atoms in the dislocation loop increases because of the diffusion of neutral interstitials from the matrix to the dislocation loop and it decreases owing to ionization processes caused by irradiation with fast electrons:

$$\frac{dN_n}{dt} = \oint (\mathbf{j}_i - \mathbf{j}_v)d\mathbf{S} - \frac{dN_c}{dt}, \tag{3}$$

where $\mathbf{j}_i$ and $\mathbf{j}_v$ are the fluxes of interstitial atoms and vacancies per dislocation loop, respectively. The change in the total number of interstitial atoms in the dislocation loop is obviously determined only by the fluxes of vacancies and interstitial atoms onto this loop:

$$\frac{dN_{tot}}{dt} = \frac{2\pi R 2\pi r_0}{a^4}(D_i C_i - D_v C_v), \tag{4}$$

where r_0 is the radius of the dislocation core; D_i and D_v are the diffusion coefficients for interstitial atoms and

vacancies, respectively; and C_i and C_v are the concentrations of the interstitial atoms and vacancies, respectively. If the dislocation loops are large and the temperature is low, the mobility of vacancies is also low and the growth of the interstitial dislocation loop with time is determined by the relationship [9]

$$R \approx \left(\frac{3Z_iGt}{\pi q_0 N_L}\right)^{1/3}, \qquad (5)$$

where $Z_i \approx 1$ is the asymmetry coefficient of the absorption of interstitial atoms by the dislocation loop, G is the rate of point-defect formation, $q_0 \approx 3$–5 is the dimensionless coefficient of point-defect recombination, and N_L is the dislocation-loop density. Then, the equation of the total charge of the interstitial dislocation loop acquires the form

$$\frac{dQ}{dt} = \left(\frac{\pi R^2}{a^2} - \frac{Q}{e}\right)\langle \sigma \rangle_I \Phi. \qquad (6)$$

The general solution of this equation is

$$Q = \frac{\pi \langle \sigma \rangle_I \Phi}{a^2} \int_0^t R^2(\tau) e^{\langle \sigma \rangle_I \Phi(t-\tau)/e} d\tau. \qquad (7)$$

Since the energy E_0 of incident fast electrons considerably exceeds the ionization energy I of electrons in the interstitial atoms, it is possible to calculate the elastic scattering cross section using the Rutherford formula [10]

$$\langle \sigma \rangle_I = \int_I^{E_0} \frac{d\sigma}{dE} dE = 4\pi a_0^2 \frac{E_R^2}{IE_0}\left(1 - \frac{I}{E_0}\right), \qquad (8)$$

where $a_0 = 0.53$ Å is the Bohr radius and $E_R = 13.6$ eV is the Rydberg energy. If the number of neutral interstitial atoms in the dislocation loop considerably exceeds the number of charged atoms, $N_n \gg N_c$ and $\langle \sigma \rangle_I \Phi t/e \ll 1$, then the exponent in Eq. (7) may be ignored. Thus, according to Eqs. (5) and (7), the electrostatic charge of the dislocation loop increases as

$$Q \approx \frac{3}{5}\frac{\pi R^2}{a^2}\langle \sigma \rangle_I \Phi t. \qquad (9)$$

It is well known that electric voltage near the edge of an infinitely thin charged disk with the charge Q and radius R at the distance ρ equals [11]

$$E \approx \frac{Q}{\varepsilon R}\sqrt{\frac{1}{2\rho R}}, \qquad (10)$$

where ε is the dielectric constant of the medium.

As a result, the elastic stress arising near the edge of the charged interstitial dislocation loop because of polarization of the medium is [11]

$$\sigma \approx \frac{Q^2}{16\pi\varepsilon\rho R^3} \approx \left(\frac{3}{20}\right)^2 \frac{\pi R}{\varepsilon\rho a^4}\langle \sigma \rangle_I^2(\Phi t)^2. \qquad (11)$$

Thus, with the growth of the dislocation loop, elastic stresses increase with time and, when the theoretical yield stress is reached, initiate plastic deformation near the dislocation loop. Figure 1 shows the experimentally observed spontaneous transformation [4] of the dislocation loop under high elastic stresses into a dislocation network. This transformation is explained by the beginning of plastic deformation at the dislocation loop and the corresponding relaxation of high elastic stresses.

It was experimentally established [4–6] that, up to 288.3 s after the formation and growth of the dislocation loop, its average radius reaches 600 nm and the dislocation loop becomes unstable. Thus, assuming that the ionization energy I is close to the Rydberg energy E_R, we draw the following conclusion from Eqs. (8) and (11). For the 600-nm-long dislocation loop grown for 288.3 s, the elastic stresses close to the theoretical yield point, $\sigma_S = \mu/2\pi \approx 6 \times 10^{10}$ dyn/cm^2, can be obtained by using a 10^{11} e/(m^2 s) flux of 200-keV electrons. This flux is much lower than the maximum flux of 1.5×10^{23} e/(m^2 s) in the center of the electron beam, where the temperature is very high and the formation of new clusters is impossible, because the annealing rates are high and clusters are decomposed due to the high temperatures. At the electron-beam periphery, where the temperature is much lower, dislocation loops are formed and grown, and the growing dislocation loops subsequently become unstable and the electron flux is much lower [10^{15}–10^{18} e/(m^2 s)]. Thus, the above mechanism ensures charge accumulation at the dislocation loop because of the dynamic loss of electrons from the interstitial atoms of the dislocation loop owing to the elastic scattering of electrons by the electrons of the interstitial atoms even in the presence of all possible relaxation mechanisms. Substituting the values obtained above, we see that $\langle \sigma \rangle_I \Phi t/e \approx 0.14 \ll 1$, which proves the validity of the approximations that were used to derive Eq. (11).

Thus, the experimentally observed transformation of the dislocation loop with considerable elastic stresses into the dislocation network (see Fig. 1) is explained by the charge accumulation that occurs at the dislocation loop due to ionization processes and the subsequent plastic deformation near the dislocation loop that leads to the relaxation of high elastic stresses near the loop. The diffusion flux of electrons that are present in the matrix and incident on a positively charged dislocation loop obviously increases the flux of incident fast electrons, which is used here to evaluate the instability of the charged dislocation loop and to determine the time of the initiation of plastic deformation near this dislocation loop. However, the reserve equal to five orders of magnitude indicates that the above relaxation processes cannot prevail over the ion-

ization processes. Various competing processes will be analyzed and be discussed in more detail elsewhere.

REFERENCES

1. K. Yasuda, M. Nastasi, K. E. Sickafus, *et al.*, Nucl. Instrum. Methods Phys. Res. B **136–138**, 499 (1998).

2. K. E. Sickafus, Hj. Matzke, T. Hartmann, *et al.*, J. Nucl. Mater. **274**, 66 (1999).

3. K. E. Sickafus, Hj. Matzke, T. Hartmann, *et al.*, Nucl. Instrum. Methods Phys. Res. B **141**, 358 (1998).

4. A. I. Ryazanov, K. Yasuda, C. Kinoshita, and A. V. Klaptsov, J. Nucl. Mater. **307–311**, 918 (2002).

5. K. Yasuda, C. Kinoshita, S. Matsumura, and A. I. Ryazanov, J. Nucl. Mater. **319**, 74 (2003).

6. A. I. Ryazanov, K. Yasuda, C. Kinoshita, and A. V. Klaptsov, J. Nucl. Mater. **323**, 372 (2003).

7. O. S. Oen, *Cross Section for Atomic Displacements in Solids by Fast Electrons* (1973), ORNL-4897.

8. S. J. Zinkle and C. Kinoshita, J. Nucl. Mater. **251**, 200 (1997).

9. V. A. Borodin, A. I. Ryazanov, and D. G. Sherstennikov, Preprint IAÉ-5457/11 (Inst. of Atomic Energy, Moscow, 1992).

10. M. W. Thompson, *Defects and Radiation Damage in Metals* (Cambridge Univ. Press, Cambridge, 1969; Mir, Moscow, 1971).

11. L. D. Landau and E. M. Lifshitz, *Course of Theoretical Physics*, Vol. 8: *Electrodynamics of Continuous Media*, 3rd ed. (Nauka, Moscow, 1992; Pergamon, New York, 1984).

Translated by L. Man

Skyrmion-Approach Study of the Magnetic Properties and Spin Kinetics of Weakly Doped Cuprates

S. I. Belov, A. D. Ineev, and B. I. Kochelaev

Kazan State University, ul. Kremlevskaya 18, Kazan, 420008 Russia
e-mail: Boris.Kochelaev@ksu.ru
Received February 8, 2005; in final form, March 15, 2005

The evolution of the magnetic and kinetic properties of quasi-two-dimensional cuprates has been studied upon doping CuO_2 planes with electron holes. The notion of thermal skyrmions and hole-induced skyrmions was used to determine the spin-correlation length and nuclear relaxation rate as functions of temperature and hole concentration. © 2005 Pleiades Publishing, Inc.

PACS numbers: 74.72.–h, 75.10.–b

At present, the transformation of insulating layered cuprates to superconductors upon doping CuO_2 planes with electron holes still remains one of the most intriguing problems of the theory of high-temperature superconductivity. Nevertheless, no commonly accepted scenario for this evolution exists as yet, so that it calls for further investigation. In this work, we propose an alternative method for describing the radical transformation occurring in the magnetic and kinetic properties of the parent compounds at low hole concentrations.

It is known that undoped cuprates can be described using the model of a quantum Heisenberg antiferromagnet with $S = 1/2$ on a square lattice with a large exchange-interaction constant between the nearest neighbors. Many attempts have been made to develop the theory of magnetic and kinetic properties of these compounds using renormalization-group analysis, the $1/N$-expansion technique, and the chiral perturbation theory (cf., e.g., [1–4]). It was shown in [5, 6] that two-dimensional antiferromagnetism can successfully be studied in the skyrmion approach. The spectrum of elementary spin excitations above the skyrmion state, the local order parameter σ, the skyrmion mean size r_0, and the nuclear relaxation rate $1/T_1$ were found in the temperature range $0 < T < J$. At the same time, there is evidence that the quasi-localized motion of a hole over the CuO_2 plane in the Coulomb field of a dopant (Sr or Ba in La_2CuO_4) induces the formation of a three-dimensional spin texture whose topology coincides with the skyrmion structure [7]. Therefore, one can assume that both thermal skyrmions and hole-induced skyrmions are present in doped cuprates. Following the method described in [5, 6], we will determine the skyrmion mean size (related to the correlation length as $\xi = 2r_0$) and the nuclear relaxation rate as functions of the temperature and hole concentration.

In the case of many topological excitations, it is natural to expect that the nearest neighbors of each skyrmion are antiskyrmions and vice versa; this means that the total magnetization of the sublattices is zero (the Mermin–Wagner–Hohenberg theorem). In thermodynamic equilibrium, the probability of formation of a thermal skyrmion–antiskyrmion pair is proportional to $\exp(-\varepsilon_{sk}/T)$, where $\varepsilon_{sk} = 4\pi\sigma(1-\sigma)J$ is the renormalized skyrmion energy in the presence of spin fluctuations, σ is the local order parameter, and J is the exchange-interaction constant between nearest neighbors [5]. The total number of topological excitations is equal to the sum of the numbers of thermal and hole-induced skyrmions. Then, the equation for the skyrmion mean size in the weak-doping case can be rewritten as

$$\frac{a^2}{2\pi r_0^2} = n/2 + (1-n)\exp\left(-\frac{4\pi\sigma(1-\sigma)}{\tau}\right), \qquad (1)$$

where n is the concentration of quasi-localized holes and $\tau = T/J$.

The self-consistent equation for the order parameter σ was obtained by the Green's function method in [5]:

$$\sigma = \frac{e}{2\sqrt{2\pi}}\frac{r_0\tau}{a}\exp\left(\frac{2\sqrt{\pi}(\sigma - \sigma_{cr})}{\tau}\right), \qquad (2)$$

where $\sigma_{cr} = \sqrt{\pi}/4$. Therefore, we arrive at the system of two nonlinear equations (1) and (2) for $r_0 = r_0(T, n)$ and $\sigma = \sigma(T, n)$. Since this system has no exact analytical solution, we used numerical methods.

The calculated reciprocal correlation length as a function of temperature is shown in Fig. 1 for different hole concentrations and for the exchange integral $J = 1300$ K between the copper ions, together with the experimental data obtained in [8].
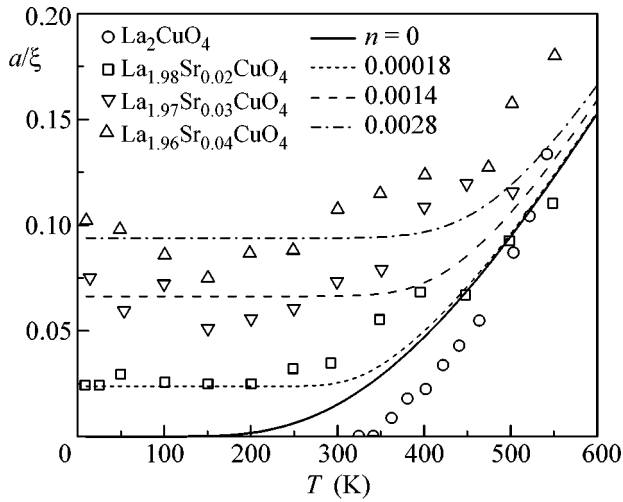
Fig. 1. Temperature dependence of the reciprocal skyrmion radius; solutions of Eqs. (1) and (2) and experimental data from [8] for various concentrations n of holes forming skyrmions.

Fig. 2. Temperature dependence of the nuclear relaxation rate; solutions of Eqs. (1)–(3) and (insert) experimental data from [9] for various concentrations n of holes forming skyrmions and for nominal concentrations x.

It is seen that the high-temperature dependence of the reciprocal skyrmion radius depends weakly on the hole concentration in the used approximation (at high temperatures, the thermal skyrmions play a dominant role) and is in qualitative agreement with the experiment.

The nuclear relaxation rate that is associated with the hyperfine interaction between the nuclear and electron spins in copper ions was obtained in [6] as a function of the order parameter and skyrmion size:

$$\frac{T_1^*}{T_1} = 0.79 \frac{\tau^2}{\sigma} \frac{r_0}{a}. \tag{3}$$

Here, $1/T_1^* = \sqrt{\pi} A^2/4J$, where A is the hyperfine-interaction constant. Using the values of σ and r_0 calculated for zero concentration, one can obtain the nuclear relaxation rate as a function of temperature and concentration. The results are presented in Fig. 2.

It is seen in Fig. 2 that $1/T_1$ does not converge at $T \longrightarrow 0$ in the case of zero concentration; the nuclear relaxation rate tends to zero. The rate increases with temperature as T^2, reaches a maximum (most pronounced at low concentrations), then decreases, and remains nearly constant at high temperatures. It is remarkable that the relaxation rate is independent of the hole concentration at high temperature; this fact is consistent with the experimental data by Imai, Slichter, *et al.* [9].

The results presented above suggest that the skyrmion approach enables one to account for the key features of the evolution of the magnetic properties of cuprates upon doping. At the same time, it should be noted that these properties start to strongly change at
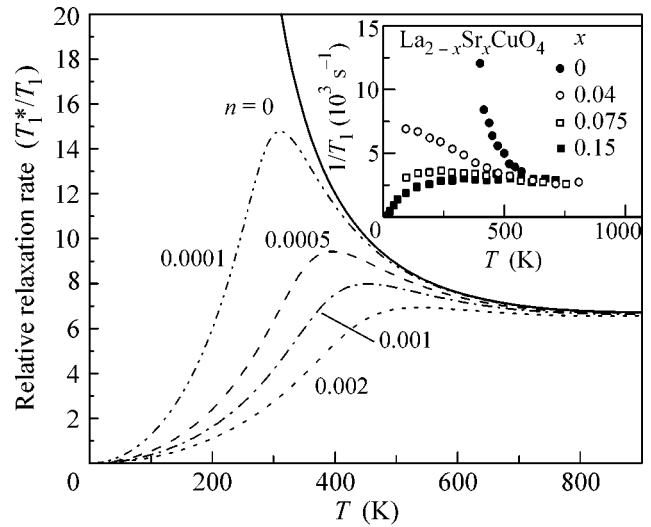
much lower hole concentrations compared to experiment, and this contradiction is most pronounced for the nuclear relaxation rate. In fact, such an apparent contradiction can be explained by the well-known phase-separation phenomenon in cuprates. In particular, recent EPR measurements of the phase separation in $La_{2-x}Sr_xCuO_4$ have shown that, at $x < 0.06$ and low temperatures, charge carriers in the CuO_2 plane are separated into hole-rich and hole-depleted regions [10]. Therefore, at a low doping level, most holes are concentrated in a small region of the sample and make almost no contribution to the NMR signal. Hence, the observed NMR signal comes from the region with a low concentration of quasi-localized holes that induce skyrmion formation; the concentration of such holes is expected to be much lower than the nominal concentration of holes introduced in the sample.

It is worth noting that interest in the spiral type of perturbations of antiferromagnetic spin order upon doping cuprates, which was suggested in [11] shortly before the "skyrmion" idea, has recently been rekindled. In particular, the role of the disordered distribution of doping impurities in the formation of the spin-glass state at $0.02 < x < 0.06$ was investigated in [12] under the assumption that all holes are localized by these impurities and form spiral local distortions of the antiferromagnetic order. In contrast, the authors of [13, 14] used the t–J model and have drawn the conclusion that the spiral state in the CuO_2 plane is generated by a delocalized hole if the exchange interaction is taken into account not only between the nearest copper ions but also between the next two coordination spheres. However, it has been shown quite recently that a hole in the Zhang–Rice model (that underlies the t–J model for cuprates) perturbs the antiferromagnetic order in the

form of a skyrmion in both localized and mobile states [15]. Evidently, the decisive role in the answer to the question of what ground state is generated by the electron hole in the CuO_2 plane of the parent compounds of superconducting cuprates belongs to the experiment.

Therefore, based on the assumption that a fraction of electron holes that are doped into a quasi-two-dimensional antiferromagnet initiates skyrmion formation, and, using the concept of skyrmions of two types (thermal and hole-induced), the spin correlation length and nuclear relaxation rate have been calculated for the doped compound. The results are in qualitative agreement with the experimental data.

REFERENCES

1. S. Chakravarty, B. I. Halperin, and D. R. Nelson, Phys. Rev. B **39**, 2344 (1989).

2. S. Tyc, B. I. Halperin, and S. Chakravarty, Phys. Rev. Lett. **62**, 835 (1989).

3. P. Hasenfratz and F. Niedermayer, Phys. Lett. B **268**, 231 (1991); Z. Phys. B **92**, 91 (1993).

4. A. V. Chubukov, S. Sachdev, and J. Ye, Phys. Rev. B **49**, 11919 (1994).

5. S. I. Belov and B. I. Kochelaev, Solid State Commun. **103**, 249 (1997).

6. S. I. Belov and B. I. Kochelaev, Solid State Commun. **106**, 207 (1998).

7. R. J. Gooding, Phys. Rev. Lett. **66**, 2266 (1991).

8. B. Keimer, N. Belk, R. J. Birgeneau, *et al.*, Phys. Rev. B **46**, 14 034 (1992).

9. T. Imai, C. P. Slichter, K. Yoshimura, and K. Kosuge, Phys. Rev. Lett. **70**, 1002 (1993).

10. A. Shengelaya, M. Bruun, B. I. Kochelaev, *et al.*, Phys. Rev. Lett. **93**, 017001 (2004).

11. B. I. Shraimann and E. D. Siggia, Phys. Rev. Lett. **62**, 1564 (1989).

12. N. Hasselmann, A. H. Castro Neto, and C. Morais Smith, Phys. Rev. B **69**, 014424 (2004).

13. O. P. Sushkov and V. N. Kotov, Phys. Rev. B **70**, 024503 (2004).

14. V. N. Kotov and O. P. Sushkov, Phys. Rev. B **70**, 195105 (2004).

15. T. Morinari, cond-mat/0502437.

Translated by V. Sakun

On the Nature of the Acoustic Mechanism of Domain Formation in a Cholesteric Liquid Crystal

O. A. Kapustina

Andreev Institute of Acoustics, Russian Academy of Sciences, ul. Shvernika 4, Moscow, 117036 Russia
e-mail: oakapustina@yandex.ru
Received August 17, 2004; in final form, March 17, 2005

The dual nature of the acoustic mechanism of destabilizing the planar texture of a cholesteric liquid crystal is confirmed experimentally. This destabilization manifests itself in the formation of a system of two-dimensional domains in the frequency range where the wavelength exceeds the cholesteric-helix pitch. A criterion for identifying two independent acoustic mechanisms (vortex and relaxation ones) is suggested and experimentally verified by analyzing the measured dependence of the critical compression amplitude on the cholesteric-helix pitch in the 40-, 120-, and 240-μm-thick mesophase layers for frequencies of 2.95 and 14.5 MHz, which are respectively lower and higher than the reciprocal relaxation time of the orientational order parameter of the cholesteric liquid crystal. © *2005 Pleiades Publishing, Inc.*

PACS numbers: 61.30.–v

The formation of a system of two-dimensional domains as a "square grid" [1] in a planar layer of a cholesteric liquid crystal (CLC) under the action of acoustic vibrations was discovered more than a quarter of a century ago. However, the mechanism of this phenomenon has not yet been unambiguously established. Recently, several attempts were made to construct models for interpretation of this effect [2, 3]. Today, the most attractive and reliable models are based on quite different approaches and postulate the existence of two independent acoustic mechanisms of the domain formation in the CLC: the "vortex" (linear [4]) and relaxation (nonlinear [5]) mechanisms. The key concept of the classical theory [4] (model I), which is based on the equations of the linear hydrodynamics of the CLC [6], is the introduction of an anisotropic term into the viscoelastic stress tensor. This term is associated with both the relaxation of the orientational-order parameter and the dispersion jump ΔE of the elastic modulus of the medium compressed along the crystal axis and normally to it. The approach that was used in [5] (model II) dramatically differs from the traditional one: it includes nonlinear corrections to the hydrodynamic equations that are attributed to structural relaxation. When determining rotational moments and stresses that are nonlinear with respect to the medium deformation and that have the relaxation nature, this approach invokes the microscopic model introduced for the statistical description of liquid crystals in [7–9].

One of the major questions concerning structural transformations in the CLC in acoustic fields is whether it is possible to experimentally identify different mechanisms of domain formation, and, if it is possible, to find the method of such identification and, thus, con-

firm the dual nature of this phenomenon. In this work, in order to answer this question, structural transformations in the planar layers of the CLC are experimentally studied under the action of the acoustic factor that is close to critical and the dependence of the critical value of this factor (the critical compression amplitudes ε_c) on the pitch P of a cholesteric helix and the layer thickness d is determined in two considerably different frequency ranges: below and above the boundary frequency equal to the reciprocal relaxation time of the orientational-order parameter.

The studies were performed on CLCs with equilibrium helix pitches of 2, 4, 10, and 30 μm. These were diluted cholesteryl chloride solutions in a ZhK-404 nematic liquid crystal (NLC). The typical configuration of the distribution of the director orientation in a thin CLC under the tangential orientational boundary conditions on both its sides is shown in Fig. 1a. In the unperturbed state, the helix axis h is normal to the layer (z axis) and the cholesteric layers are parallel to the boundaries of the layer with the coordinates $z = 0$ and d. The acoustic conditions at these boundaries are such that, if a longitudinal compression wave with the frequency ω and the compression amplitude ε_0 is incident onto the layer along its normal, then a standing wave of the form $\varepsilon = 2\varepsilon_0\cos[\omega(d-z)/c]\sin\omega t$ is generated in the layer, where c is the speed of sound in the CLC. We consider the frequency range where the wavelengths in the CLC exceed the cholesteric-helix pitch. It is also assumed that the cholesteric-helix pitch is much less than the thickness of the CLC layer.

The simplified schematic of the experimental setup is shown in Fig. 1b. The CLC solution fills a flat cell that is formed by glass plate *2* (an acoustically rigid

boundary, i.e., a boundary completely reflecting sound) and sound-transparent polymer film *3* with a light-reflecting coating. In order to create planar boundary conditions in the cell, its internal surfaces were preliminarily coated with a thin polymer (polyvinyl alcohol) film and then these surfaces were rubbed along the same direction to create an easy orientation axis for CLC molecules (Chatelin's method [2]). The cell design allowed us to vary the thickness of the CLC layer within 10–240 μm by varying the gap between plate *2* and film *3* (microdisplacements) in a way to preserve the boundary conditions in the cell and maintain the constant energy of cohesion between the CLC molecules and the cell walls. This procedure completely excluded fluctuations in the threshold ultrasound values associated with the above factors. The gap between plate *2* and film *3* in the cell was determined from the interference transmission spectrum. The homogeneity of the initial planar texture in the cell and its changes under the action of the acoustic factor were observed with a polarization optical microscope according to the schemes considered in detail in [2]. The transmission band of the optical system determined by the interference filter was 0.63 ± 0.6 μm. The CLC temperature in the cell was maintained constant (20°C) within an accuracy of 0.5° using a thermostat. Longitudinal waves *4* were generated by an ultrasonic transducer (Straubel-cut quartz [10] with a quasi-uniform distribution of the vibration amplitudes along the plate surface). The acoustic contact between the transducer and the cell that was filled with the CLC solution was provided by a thin transition layer of salol. The interaction level was monitored by a voltmeter measuring the voltage applied to the transducer. Then, this voltage was recalculated to the compression amplitude at the CLC layer boundary with the coordinate $z = 0$ by the well-known method for calculating the vibration amplitude of a multilayer system (transducer–transition layer–liquid crystal) with due regard for its resonance properties [10]. The vibration frequencies were 2.95 and 14.5 MHz.

The experiments were performed as follows. The cell was filled with a solution of the CLC with a certain helix pitch. Then, by moving plate *2* at the given gap value, a state of the cholesteric structure was created such that the distance *d* included an integer number of half-turns of the cholesteric helix. In this situation, the helix that was "inscribed" into the gap remained undeformed so that its pitch in the cell corresponded to the equilibrium pitch P_0 of the infinite CLC [6] (Fig. 1a). Then, an electric voltage was applied to the ultrasonic transducer and it was increased up to a value providing the formation of two-dimensional domains forming a square grid of equidistant bright lines parallel and normal to the lines of rubbing.

Two runs of experiments on the determination of the factors critical for domain formation were performed on the 40-, 120-, and 240-μm-thick planar CLC layers in four solution with the concentrations of the optically
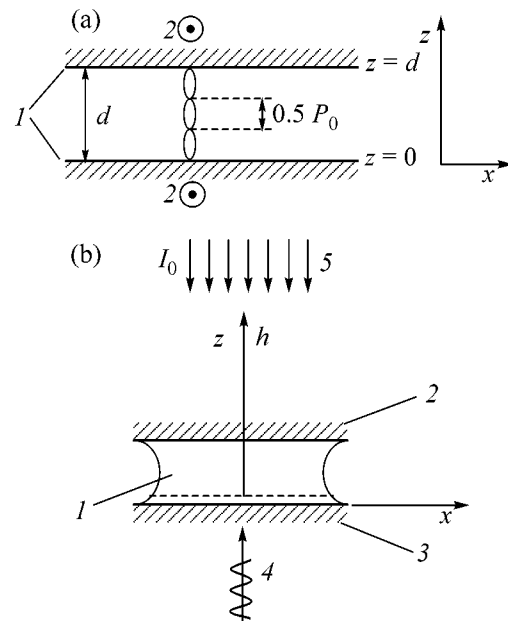

Fig. 1. (a) Problem geometry: (*1*) the surfaces of the cell at tangential orientational boundary conditions and (*2*) the directions of rubbing of these surfaces (the cholesteric helix is located along the *z* axis); (b) simplified schematic of the experiment: (*1*) the CLC, (*2*) the optically transparent plate (glass), (*3*) the sound-transparent film with a light-reflecting coating, (*4*) the longitudinal acoustic wave, and (*5*) the light flux incident onto the CLC layer along the layer normal (*z* axis).

active component (cholesteryl chloride) corresponding to the formation of the cholesteric phase with the above helix pitch at two frequencies, 2.95 and 14.5 MHz.

Figure 2 illustrates the experimental data on the critical compression amplitude for CLC solutions with the cholesteric-helix pitch ranging within 2–30 μm and a 120-μm-thick layer at the frequencies 2.95 and 14.5 MHz. It is seen that, with an increase in the helix pitch, the critical compression amplitudes either increase (at a frequency of 2.95 MHz) or decrease (at a frequency of 14.5 MHz). The solid and dashed straight lines that are drawn through the experimental points are the dependences $\varepsilon_c \sim P^{1/2}$ (at a frequency of 2.95 MHz) and $\varepsilon_c \sim 1/P^{1/2}$ (at a frequency of 14.5 MHz), respectively. Thus, with the passage from the frequencies $f < f_2$ to the frequencies $f > f_2$, the form of the function $\varepsilon_c(P)$ changes dramatically. The critical compression amplitudes of the same CLC solutions in the 40- and 120-μm-thick layers behave in the same way at these frequencies. This allowed us to draw the conclusion about the universal character of the above relation between the quantities ε_c and P in different frequency ranges.

The inset in Fig. 2 shows the experimental data on the effect of the layer thickness on the critical compression amplitude for the CLC solution with a helix pitch of 2 μm at the frequencies 2.95 and 14.5 MHz. It is seen that an increase in the layer thickness *d* at the constant
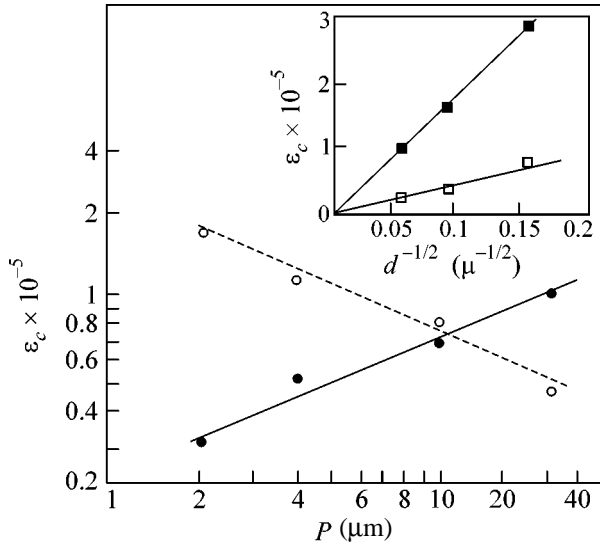
Fig. 2. Critical compression amplitude vs. the cholesteric helix pitch for a 120-μm-thick CLC layer at the frequencies (●) 2.95 and (○) 14.5 MHz. The inset: the critical compression amplitude vs. the thickness of the CLC layer at a constant helix pitch of 2 μm for frequencies of (■) 2.95 and (□) 14.5 MHz.

helix pitch for both frequencies results in a decrease in the critical compression amplitudes. This dependence is approximated by the function $\varepsilon_c \sim d^{-1/2}$.

Now, let us consider the formation of two-dimensional domains in an ideal planar CLC layer in the frequency range where the acoustic wavelength exceeds the cholesteric-helix pitch in terms of the models suggested in [4, 5].

Model I that was suggested in [4] postulates the vortex mechanism of destabilizing the planar texture of the layer and predicts a considerable change in the threshold of the effect with the change of the vibration frequency. It also predicts that the effect is the most pronounced in the frequency range $\omega_1 < \omega < \omega_2$, where the critical compression amplitude depends weakly on the frequency and is described by the expression

$$\varepsilon_c = (k/q)\{\rho K_{33}(3 + b)(1 - \delta)/4\gamma\tau\Delta E$$
$$\times [1 + \sin(2k_s d)/2k_s d]\}^{1/2}. \quad (1)$$

Beyond this range, the threshold of the effect is strongly frequency dependent and the critical compression amplitude changes according to the laws $\varepsilon_c \sim \omega^{-1/2}$ (at $\omega > \omega_1$) and $\varepsilon_c \sim \omega$ (at $\omega > \omega_2$). Here, $q = 2\pi/P$; $k = \pi 2^{1/2}/\Lambda$ is the wavenumber of the domains; $b = K_{33}/K_{22}$; K_{22} and K_{33} are the Frank elastic constants; ρ and γ are the density and rotational viscosity, respectively; τ is the relaxation time of the orientational-order parameter; δ is the parameter taking into account the relative extension of the cholesteric layers along the helix axis that may occurs because the boundaries of the CLC layer can be nonparallel (e.g., in the vicinity of the

Grandjean lines) or because pairs of disclinations can exist [6]; $k_s = \omega/c$; $\omega_1 = 1/A\tau$; $\omega_2 = 1/\tau$; and A is the combination of the parameters P, d, ρ, τ, and the Lesley viscosity coefficient α_i.

Model II [5] allows another interpretation of the phenomenon under consideration. It is based on the nonlinear relaxation mechanism that is most efficient for frequencies $\omega > \omega_2$ at which the critical compression amplitude is frequency independent and is equal to

$$\varepsilon_c = k\{K_{33}(3 + b)(1 - \delta)/\gamma(2\Omega_1 B + \Omega_2)F(\omega, \tau)\}^{1/2}. \quad (2)$$

Here, Ω_1 and Ω_2 are the parameters having the dimensionality of frequency, B is the combination of the viscosity coefficients, and $F(\omega, \tau) = \omega^2\tau^2/(1 + \omega^2\tau^2)$. With the passage to frequencies $\omega < \omega_2$, the critical amplitude ε_c increases rapidly as $\varepsilon_c \sim 1/\omega$ with a decrease in the vibration frequency.

Summarizing the above data, it is possible to state that the combined action of the vortex and relaxation mechanisms in the CLC results in a complex nonmonotonic dependence of the critical compression amplitude on the vibration frequency. In addition, there exist frequency ranges where this amplitude has a constant value at a constant layer thickness and constant cholesteric-helix pitch. Under the conditions of the above experiments with CLC solutions at the helix pitch varying from 2 to 30 μm and the layer thicknesses ranging within 40–240 μm, the boundaries of these ranges are determined by the frequencies $f_1 = \omega_1/2\pi \geq 0.5$ MHz and $f_2 = 1/2\pi\tau = 5.3$ MHz. (When evaluating the frequency f_2, we used the value $\tau = 3 \times 10^{-8}$ s characteristic of NLCs [2, 6].) Therefore, the frequencies 2.95 and 14.5 MHz that are used in our experiments really belong to the frequency ranges in which different acoustic mechanisms dominate.

We note that the difficulties associated with the selection of a criterion for determining the preferable model, I or II, in different frequency ranges and the evaluation of the contributions due to these mechanisms are partially explained by the fact that it is impossible to visually distinguish domains of different origins, because both vortex and relaxation mechanisms generate domains of the same size equal to [4, 5]

$$\Lambda = (Pd)^{1/2}[(3 + b)/8b]^{1/4}. \quad (3)$$

This statement is also confirmed by the observation of this effect at frequencies ranging from 0.3 to 16.0 MHz [11, 12]. In this respect, the only possible method of identifying these two independent mechanisms is the comparison of changes in the critical compression amplitudes at varying parameters P and d in the frequency ranges satisfying the inequalities $\omega_1 < \omega < \omega_2$ and $\omega > \omega_2$. Then, the theory [see Eqs. (1) and (2)] leads to the important conclusion on the dramatic change in the character of the relation between the critical compression amplitude and the helix pitch in the transition

through the boundary frequency f_2 separating the regions with two different prevalent mechanisms. Under the conditions where the vortex mechanism of destabilization (model I) prevails, the critical compression amplitude obeys the law $\varepsilon_c \sim P^{1/2}$, whereas it obeys the law $\varepsilon_c \sim P^{-1/2}$ in the region where the relaxation mechanism (model II) dominates. At the same time, an increase in the layer thickness at the constant value of the helix pitch results in the decrease in the critical compression amplitude. In this case, both models give the law $\varepsilon_c \sim d^{-1/2}$. One may readily see that these theoretical predictions correlate with the experimental data in Fig. 2 showing the dependence of the critical compression amplitude on the helix pitch and layer thickness. It is remarkable that, at certain combinations of the parameters P and d, the critical compression amplitudes in different frequency ranges, where different acoustic mechanisms of destabilization are prevalent and which are separated by the frequency f_2, are close to each other. This situation is illustrated by Fig. 2 for the critical compression amplitudes for a CLC solution with the 10 μm helix pitch and 120 μm-thick layer at the frequencies 2.95 and 14.5 MHz.

The above experimental data and their interpretation based on models I and II provide the conclusion that the analysis of the form of the functions $\varepsilon_c(\omega)$ and $\varepsilon_c(d)$ is insufficient for identifying the prevalent mechanism of the destabilization of a planar CLC layer. As was experimentally established in this work, the forms of the function $\varepsilon_c(P)$ are substantially different in essentially different frequency ranges (below and above the frequency of the orientational-order parameter equal to the reciprocal relaxation time). This difference can be interpreted on the basis of the hypothesis of the determining role of the structural relaxation processes at the frequencies satisfying the condition $\omega\tau > 1$ at which the critical compression amplitude corresponding to the alternative vortex mechanism of destabilization increases proportionally to the vibration frequency ($\varepsilon_c \sim \omega$). The attempts to separate the contributions of these mechanisms showed that there exists only one criterion of their identification: the dramatic change that occurs in the form of the function $\varepsilon_c(P)$ when one destabilization mechanism is replaced by the other (Fig. 2). Thus, we managed to confirm the concept of the dual nature of the acoustic mechanism of destabilizing the planar CLC layer in the frequency range where the wavelength exceeds the helix pitch.

Thus, the main result obtained in this work is as follows. The most pronounced physical effect that allows one to experimentally identify the vortex and relaxation mechanisms and their mutual correlation is the change that occurs in the form of the dependence of the critical compression amplitude on the helix pitch when passing through the frequency equal to the reciprocal relaxation time of the orientational-order parameter in the CLC.

Concluding the article, we emphasize the necessity of developing new approaches that would take into account relaxation processes in macroscopic phenomena and justify the applicability of statistical mechanics to the analysis of the structural transitions in CLCs. Since a CLC is a kind of an NLC (both mesophases possess only the orientational order and no translational order), a considerable contribution of the relaxation processes to change in the macrostructure in acoustic fields can be also expected in NLCs. However, the limitation $k_z \ll k \ll q$ ($k_z = \pi/d$), which was imposed onto the relation of the wavenumbers when formula (2) was derived in [5], is violated in NLCs. Therefore, the evaluation of the effect of nonlinear relaxation rotational moments and stresses in this type of mesophases requires additional studies.

REFERENCES

1. O. Kapoustina, V. Loupanov, and I. Gourova, in *7eme Congres International sur les Cristeaux Liguids* (Bordeaux, 1978), p. 51.

2. *Handbook of Liquid Crystals,* Ed. by D. Demus *et al.* (Wiley, Weinheim, 1998).

3. O. Kapustina, in *Physical Properties of Liquid Crystals* (Wiley, Weinheim, 1999).

4. E. N. Kozhevnikov, Zh. Éksp. Teor. Fiz. **92**, 1306 (1987) [Sov. Phys. JETP **65**, 731 (1987)].

5. E. N. Kozhevnikov, Akust. Zh. **48**, 777 (2002) [Acoust. Phys. **48**, 687 (2002)].

6. S. A. Pikin, *Structural Transformation in Liquid Crystals* (Nauka, Moscow, 1981) [in Russian].

7. M. Doi and S. Edwards, J. Chem. Soc., Faraday Trans. 2 **74**, 560 (1978).

8. A. N. Semenov, Zh. Éksp. Teor. Fiz. **85**, 549 (1983) [Sov. Phys. JETP **58**, 321 (1983)].

9. M. Osipov and E. Terentjev, Phys. Lett. A **134**, 301 (1989).

10. L. Bergmann, *Der Ultraschall und seine Anwendung in Wissenschaft und Technik* (Hirzel, Zurich, 1954; Inostrannaya Literatura, Moscow, 1956).

11. I. Gurova and O. Kapustina, Pis'ma Zh. Éksp. Teor. Fiz. **63**, 866 (1996) [JETP Lett. **63**, 907 (1996)].

12. O. A. Kapustina, N. A. Kolesnikova, and O. V. Romanova, Akust. Zh. **50**, 77 (2004) [Acoust. Phys. **50**, 66 (2004)].

Translated by L. Man

Anisotropic Low-Temperature in-Plane Magnetoresistance in Electron Doped $Nd_{2-x}Ce_xCuO_{4+\delta}$[¶]

A. I. Ponomarev[1], L. D. Sabirzyanova[1], A. A. Ivanov[2], A. S. Moskvin[3], and Yu. D. Panov[3]

[1] Institute of Metal Physics, Ural Division, Russian Academy of Sciences, Yekaterinburg, 620219 Russia
[2] Institute of Engineering Physics, Moscow, 115409 Russia
[3] Department of Theoretical Physics, Ural State University, Yekaterinburg, 620083 Russia
Received March 2, 2005; in final form, March 21, 2005

Nominally electron doped antiferromagnetic tetragonal nonsuperconducting $Nd_{2-x}Ce_xCuO_{4+\delta}$ ($x = 0.12$) has been shown to manifest strong angular dependence of the in-plane magnetoresistance on the orientation of the external magnetic field within the *ab* plane in many aspects similar to that observed in hole doped $YBa_2Cu_3O_{7-\delta}$ and $La_{2-x}Sr_xCuO_4$. Specific fourfold angular magnetoresistance anisotropy amounting to several percents was observed in oxygen annealed films at low temperatures and in an external magnetic field up to 5.5 T. The strong temperature dependence and fourfold symmetry observed in our sample points to a specific role of rare-earth (Nd) ions in magnetoresistance anisotropy. At low temperature $T = 1.4$ K, we observed the unusual transformation of magnetoresistance response with increasing the external magnetic field, which seems to be a manifestation of a combined effect of a crossover between first and second order spin-flop transitions and a field-dependent rare-earth contribution to quasiparticle magnetotransport. © *2005 Pleiades Publishing, Inc.*

PACS numbers: 71.10.Hf, 72.20.My, 74.25.Fy, 74.72.Bk

The unusual spin and charge dynamics in high-T_c cuprates have been attracting great interest. Especially, in the underdoped region of hole-doped cuprates, many anomalous features have been unveiled. Unusual magnetoresistance anomalies were reported recently for the heavily underdoped antiferromagnetic $TmBa_2Cu_3O_{6+x}$ ($x = 0.30$) by Amitin *et al.* [1], $YBa_2Cu_3O_{6+x}$ ($x = 0.30$; 0.32) by Y. Ando *et al.* [2], $YBa_2Cu_3O_{6+x}$; ($x = 0.25$) by E. Cimpoiasu *et al.* [3], and $La_{2-x}Sr_xCuO_4$ by Y. Ando *et al.* [4]. The in-plane resistivity ρ_{ab} in all the crystals exhibits unconventional metal-dielectric duality with the high-temperature ($T > 50$ K) metal-like behavior in contrast with the low-T insulating one, which is not compatible both with that for a simple band insulator and for an Anderson insulator. The crystals demonstrate an unusual behavior of the in-plane magnetoresistance, $\Delta\rho_{ab}/\rho_{ab}$, when the magnetic field **H** is applied along the CuO_2 planes. These are a striking *d*-wave shaped ($\propto\cos 2\phi$) angular dependence with a clear $\propto 1/T$ temperature dependence, anomalous low-field behavior with saturation above a well-defined threshold field, and hysteretic effects at low temperatures.

Anisotropic magnetoresistance (AMR) anomalies observed in heavily underdoped hole-doped 123 and 214 cuprates are believed to be an important signature of the interplay between the charge and spin subsystems, which seemingly play a central role in the physics of high-temperature superconductors. This interplay, tuned by a charge doping, underlies the dramatic changes in the physical properties across the phase diagram of these materials. Its study may provide valuable information as regards the nature of charge carriers and magnetism in cuprates, their role in high T_c, and the origin of both magnetoresistance anomalies. In this connection, it is strongly desirable to extend the respective study to other cuprates, in particular, to electron doped ones. Indeed, the question arises, whether the features generic to hole-doped cuprates are observable in electron doped ones? Maybe these features are inherent only to hole carriers as it was argued in a microscopic model by Moskvin and Panov [5]?

The properties of the electron doped family of cuprates have been studied to a lesser extent than those of their hole doped counterparts. Just recently, Lavrov *et al.* [6] showed that a magnetic-field-induced transition from noncollinear to collinear spin arrangement in adjacent CuO_2 planes of lightly electron-doped $Pr_{1-3x}La_{0.7}Ce_xCuO_4$ ($x = 0.01$) crystals affects significantly both the in-plane and out-of-plane resistivity. In the high-field collinear state, the magnetoresistance does not saturate but exhibits an intriguing fourfold-symmetric angular dependence, oscillating from being positive at **H** ∥ [100] to being negative at **H** ∥ [110] with $\Delta\rho_{ab}/\rho_{ab}$ exceeding 30% at low temperatures. Fournier *et al.* [7] found sharp fourfold magnetoresistance oscillations for nonsuperconducting $Pr_{2-x}Ce_xCuO_4$ crystals at a substantially larger electron doping ($x = 0.15$). The questions arise, what is the mechanism of the revealed MR features and whether these features are observable in other electron doped cuprates?

[¶] This article was submitted by the authors in English.

The main goal of our paper was to investigate the low-temperature magnetoresistance in thin films of underdoped $Nd_{2-x}Ce_xCuO_{4+\delta}$ [8]. It turned out that the oxygen annealed films indeed reveal the anisotropic magnetoresistance, whose angular dependence exhibits anomalous field dependence evidencing the unconventional character of first-to-second order crossover for spin-reorientation transition.

The *c*-axis oriented epitaxial $Nd_{2-x}Ce_xCuO_{4+\delta}$ films with a thicknesses of 2500 Å and fixed contents of cerium ($x = 0.12$) were grown using pulsed laser ablation from a ceramic target. The process consists of the evaporation of the ceramic target by a focused laser beam and subsequent deposition of the target material on a heated single-crystal $SrTiO_3$ substrate with an orientation of [100] (with a size of 5×10 mm and a thickness of 1.5 mm). The temperature of the substrate was 800°C, the deposition pressure was 0.8 Torr, the residual gas was air, and the target was a sintered ceramic pellet of $Nd_{2-x}Ce_xCuO_{4+\delta}$ of a specified composition. In the thus obtained single-crystal films, the CuO_2 (ab) plane coincided with the plane of the substrate. To obtain samples with various oxygen contents, we made use of two regimes of annealing: "the optimum annealing" (60 min, $T = 780°C$, $p = 10^{-3}$ Torr) and "annealing in oxygen" (60 min, $T = 500°C$, $p = 760$ Torr). The x-ray diffraction measurements showed that the $Nd_{2-x}Ce_xCuO_{4+\delta}$ single-crystalline films on the $SrTiO_3$ substrates are epitaxial with [001] orientation of the surface plane and a [001] misorientation of the domains of less than one degree.

The resistivity measurements were performed with a standard four-probe technique and a superconducting solenoid in a dc magnetic field of up to $H = 6$ T in a temperature range of 1.4–300 K. First, we should note that both the as grown and annealed samples reveal the temperature dependence of resistivity [11] typical for hole-underdoped cuprates [2, 4] with high-temperature metallic and low-temperature insulating behavior. In Fig. 1, we present the temperature dependence of resistivity for the as grown and the oxygen annealed samples. To detect the in-plane magnetoresistance anisotropy, that is, the dependence of the magnetoresistance on the angle between the direction of the current and that of the external magnetic field, the sample was rotated around the *c* axis by 0–270 degrees with a fixed in-plane orientation of the magnetic field. For the oxygen annealed sample, we actually found the in-plane magnetoresistance anisotropy with minima and maxima alternating in 45°, thus, forming a four-lobe rose. In Fig. 2, we present the raw experimental magnetoresistance data obtained at $T = 4.2$ K and an external magnetic field of 4 and 5 T (the latter pattern was continued through the whole angle range). In both cases, we clearly see the fourfold angular symmetry of the AMR effect. The detailed field behavior of the AMR took place at a low temperature (1.4 K). The close examination of the field dependence of the AMR at $T = 1.4$ K
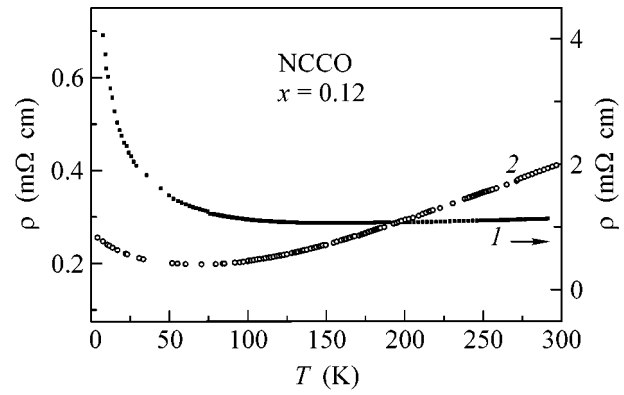

Fig. 1. Temperature dependence of resistivity for the (*1*) oxygen annealed and (*2*) grown thin films of $Nd_{2-x}Ce_xCuO_{4+\delta}$ ($x = 0.12$).

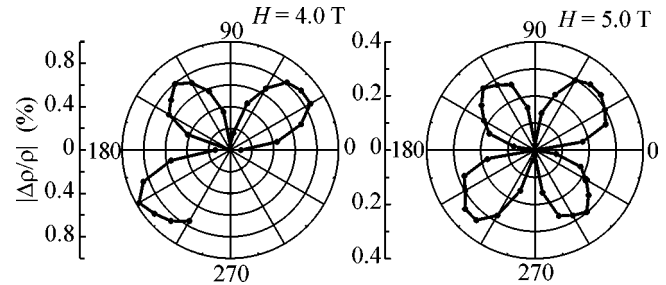**Fig. 2.** Angular dependence of magnetoresistance $\Delta\rho(h, \phi)/\rho(h, \phi = 0)$ in the oxygen annealed thin film $Nd_{2-x}Ce_xCuO_{4+\delta}$ ($x = 0.12$) at $T = 4.2$ K.

(Fig. 3) revealed its unexpected behavior. Indeed, at a relatively small external field (1.5 T), we are dealing with a fourfold four-lobe rose with lobes oriented along $\pm\pi/4$, $\pm3\pi/4$. On increasing the applied field from 1.5 up to 3.5 T, we arrive at fairly visible lobes broadening, firstly, with a flat top, then, with a concave top. Then, at $H_{ext} = 4.0$ T, we see a puzzling effect of the lobes "splitting" accompanied by a sharp decrease of the AMR effect. A further increase of the field leads to the closing in of different half-lobes along the directions $\pm\pi/2$, $\pm3\pi/2$, as a result, at $H_{ext} = 4.5$ T, we see a fourfold four-lobe rose rotated $\pm\pi/4$ with respect to that typical for small external fields. The effect is accompanied by a strong increase of the AMR, which is particularly visible at $H_{ext} = 5.5$ T, when it exceeds by an order of magnitude the 4.2 K effect. This unconventional field behavior of the AMR most likely offers evidence of an unusual rearrangement of the magnetic structure induced by an external field.

In Fig. 4, we have presented the field dependence of the magnetoresistivity for the field oriented along the direction of the current measurement. The field effect at
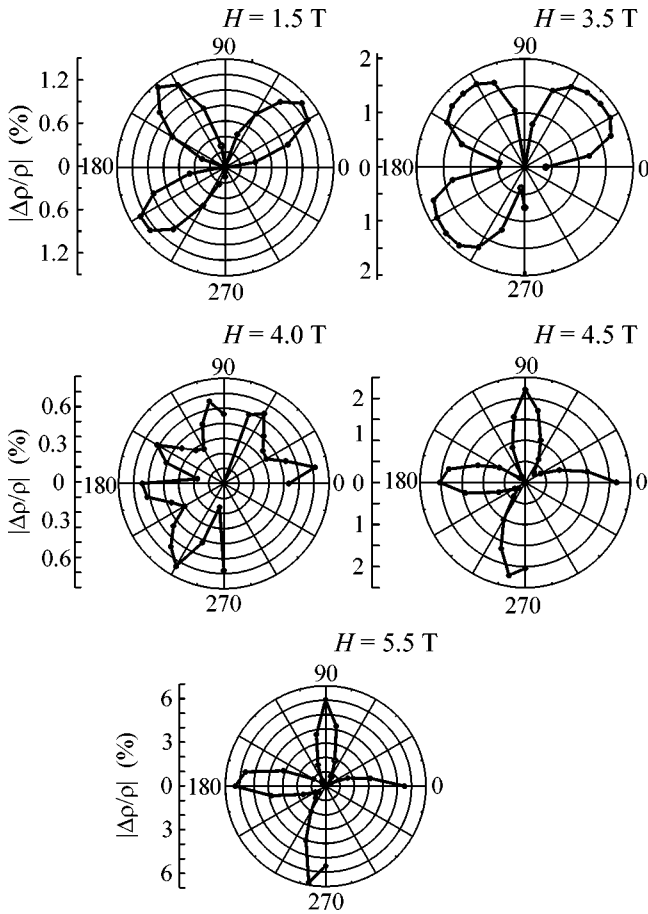
H = 1.5 T

H = 3.5 T

H = 4.0 T

H = 4.5 T

H = 5.5 T

Fig. 3. Transformation of AMR in NdCeCuO film at $T = 1.4$ K in a rising external field as evidence of unconventional first-to-second order crossover spin-reorientation transition.
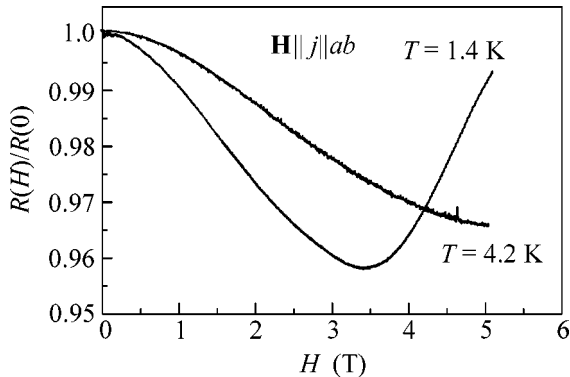

Fig. 4. Field dependence of magnetoresistance in the oxygen annealed thin film of $Nd_{2-x}Ce_xCuO_{4+\delta}$ ($x = 0.12$).

$T = 4.2$ K looks like that for the 123 and 214 systems [2, 4]. However, lowering the temperature to the range of Nd ordering leads to a puzzling reentrant effect when the magnetoresistance first falls down to $H = 3.5$ T and

then rises backwards up to small values at $H = 5$ T. It is worth noting that the reentrant behavior of the magnetoresistance reflects an interplay between the isotropic and anisotropic contributions. We did not observe sizeable hysteretic effects, which likely points to a manifestation of the effects of the rotation of the antiferromagnetic vector rather than the effects of the shift of domain walls.

Turning to the discussion of the experimental data, we first would like to note that the complete interpretation of anisotropic magnetoresistance in electron/hole doped cuprates implies knowledge of its electron structure, the structure of charge carriers, the magnetic structure, and its transformation in an external magnetic field.

Understanding the anomalous features of the in-plane and out-of-plane normal state transport, particularly magnetotransport, in layered cuprates remains a challenge. Even in the simplest form, we deal with the general problem of the transport properties of a single electron or hole in a strongly correlated antiferromagnetically ordered quasi-2D cuprate which continues to be the topic of much debate, both theoretically and experimentally.

The first purely qualitative scenario of anisotropic magnetoresistance in heavily underdoped cuprates was suggested by Ando *et al.* [2]. The authors qualitatively consider these features to be a manifestation of the "charge stripe" ferromagnetic structure in 123 system, which could be easily rotated by a rather small external magnetic field. The stripe scenario was first questioned by Janossy *et al.* [12]. In their view, the anomalous magnetoresistance is due to an *ab* plane anisotropy of the resistivity in the bulk and to a magnetic field dependent antiferromagnetic (AFM) domain structure (magnetic inhomogeneity). The phenomeno-logical symmetry based theory of anisotropic magnetoresistance in the underdoped easy-plane antiferromagnets of $YBa_2Cu_3O_{7-\delta}$-type has been developed by Gomonaj and Loktev [13] and by Cimpoiasu *et al.* [3]. The in-plane resistivity was assumed to be a symmetry allowed function of the components of the in-plane strain tensor, which was produced by the magnetoelastic coupling [3]. Gomonaj and Loktev [13] considered the in-plane resistivity to be a symmetry allowed function of the in-plane components of the antiferromagnetic vector **L**. The field and angular dependencies of the resistivity tensor in 123 systems have been shown to be in satisfactory agreement with the available experimental data for the low-field polydomain and high-field single-domain phases [3, 13]. However, despite the phenomenological approaches providing a fairly reasonable explanation of many aspects of the anisotropic magnetoresistance phenomenon, they fail to explain the magnitude of the effect observed and the strong $1/T$ temperature dependences both of isotropic and anisotropic magnetoresistance observed in 123 and 214 systems. Such a low-temperature anomaly is absolutely incom-

patible with the expected saturation of the magnetic Cu subsystem. Moskvin and Panov [5] have proposed a microscopic scenario for *hole* magnetoresistance, in which the features of the in-plane anisotropic magnetoresistance are attributed to the spin-induced orbital polarization of the triplet state formed by a doped hole in the CuO_4 centers. The model is by now the only microscopic theory that seems to provide the most consistent interpretation of magnetoresistance anomalies in cuprates. The model implies a quasi-degeneracy in the ground state of the two-hole CuO_4^{5-} center with the two close in energy $^1A_{1g}$ and ^1E_u terms of the b_{1g}^2 and $b_{1g}e_u$ configurations, respectively. In other words, one implies two near equivalent locations for the additional hole: either in the Cu3d-O2p hybrid $b_{1g}(d_{x^2-y^2})$ state to form a Zhang–Rice (ZR) singlet $^1A_{1g}$ or in a purely oxygen nonbonding doublet $e_{ux, y}$ state with particular Cu^{2+}–Cu^{3+} valence resonance. The e_u hole can be coupled with the b_{1g} hole both antiferro- and ferromagnetically. This simple consideration clearly indicates a necessity to incorporate in the valence multiplet both the spin singlet $(b_{1g}e_u)^1E_u$ and the spin triplet $(b_{1g}e_u)^3E_u$, whose energy could be even lower due to ferromagnetic $b_{1g} - e_u$ exchange. The pseudo-Jahn–Teller (JT) polaronic nature of the spin-singlet $^1A_{1g} - {}^1E_u$ ground state [14] favors their localization. In addition, one should account for the antiferromagnetic background, which leads to the crucial enhancement of the effective mass for the moving spin singlets. Consequently, a spin-singlet small pseudo-JT polaron as a hole ground state is likely to be immobile. In such a situation, the most effective channel for the hole transport could be related to the low-lying excited spin-triplet $b_{1g}e_u : {}^3E_u$ term. This gives rise to a thermoactivated hole conductivity, which is actually observed in most slightly doped cuprates. The doped electron in cuprates occupies the only $b_{1g}(d_{x^2-y^2})$ orbital to form a ZR-singlet-like $^1A_{1g}$ state. At first sight, it implies the electron-hole symmetry of the transport properties in cuprates; however, the existence of an alternative e_u state for the hole actually points to strong electron-hole asymmetry. It should be noted that the nature itself of effective charge carriers in cuprates may evolve with doping from a single hole (electron) for lightly doped systems to a collective carrier similar to a charge density wave for a sizeable doping [15, 16].

In contrast to the YBaCuO and LaCuO cuprates in the NdCeCuO and other electron doped systems, we deal with an additional factor governing the quasiparticle transport. The issue concerns the rare-earth sublattice, which is believed to strongly affect the low-temperature transport properties [6, 10]. Indeed, in the frame of a simple activation mechanism of the conductivity, it is reasonable to assume that the activation is accompanied by a change in a crystal field acting on the

R ion and its magnetic anisotropy. A tetragonal crystal field includes the magnetic field-dependent part, which can be written for the in-plane directed field as follows (see, e.g., [17]):

$$H_{cf} = d(H_{ext})\cos 4\phi, \tag{1}$$

where ϕ is an azimuthal angle of the orientation of effective magnetic field for the Nd ion that is the sum of the external magnetic field and exchange fields due to Nd–Cu and Nd–Nd coupling. Thus, we may conclude that the R ion can indirectly affect the quasiparticle transport through the activation energy, which may intricately depend on the orientation of the surrounding Nd ion magnetic momenta giving rise to a specific mechanism of anisotropic magnetotransport.

The explanation of the low-temperature magnetotransport properties in the $Nd_{2-x}Ce_xCuO_{4+\delta}$ system is hampered by the lack of information sufficient to understand and describe its magnetic state. To the best of our knowledge, the magnetic-field studies were performed only for undoped Nd_2CuO_4, where the Cu sublattice first orders antiferromagnetically into the noncollinear type-I spin structure below $T_{N1} \approx 275$ K [18]. On further cooling, the Cu spins reorient into type-II (at $T_{N2} \approx 75$ K) and type-III ($T_{N3} \approx 30$ K) phases. In the type-II phase, all the Cu spins rotate by $\pm90°$ about the c axis from the type-I phase. They rotate back to their original direction below T_{N3} in the type-III phase. As discussed in [17], we may consider the entire system to be built up of weakly interacting sets of planes, each set consisting of a Cu plane with one Nd plane above it and another below it. Thus, for most purposes, it suffices to consider a 2D model consisting of a single set of Nd–Cu–Nd threeplanes. The energy of the interplane A–B coupling may be written as a result of the effective the pseudo-dipolar interactions between Cu moments as follows:

$$E_{AB} = -Q\sin(\Phi_A + \Phi_B),$$

where $\Phi_{A, B}$ are the azimuthal angles of the orientation of Cu antiferromagnetic vectors for *A*, *B* units, respectively. This energy is minimal at $(\Phi_A + \Phi_B) = \pi/2$ if $Q > 0$ and at $(\Phi_A + \Phi_B) = -\pi/2, 3\pi/2$ if $Q < 0$. The parameter $Q > 0$ in phases I and III, and $Q < 0$ in phase II; in other words, it changes its sign twice, which explains the result of the subtle competition of Cu–Cu, Cu–Nd, and Nd–Nd contributions to Q [17, 19]. It should be noted that any of these spin-reorientation transitions proceeds via two equivalent clockwise and counterclockwise rotations of Cu antiferromagnetic vectors when the relation $(\Phi_A + \Phi_B) = \pi/2$ (phases I, III) transforms into $(\Phi_A + \Phi_B) = -\pi/2, 3\pi/2$ (phase II).

On further lowering the temperature, the large exchange coupling between the Cu and Nd polarizes the Nd spins and induces an ordered moment. Below about 30 K, the ordered arrangement of the Cu and Nd spins is noncollinear. At low temperatures $T < 1.5$ K, the application of a magnetic field of about 4.4 Tesla

along the [100] direction seems to result in a spin-flop transition, in which the Cu and Nd spins oriented along the [100] direction rotate in-plane by 90° [20]. This would result in a collinear spin structure in which all of the ordered moments are approximately perpendicular to $\mathbf{H}_{ext}$. If a smaller field (0.7–2 T) is applied along the [110] direction, there is a spin-flop transition in which all of the spins rotate in plane by about 45°, giving rise to the same collinear spin structure [20]. The field at which each of these transitions occurs has been studied using several techniques; however, the effect of an applied field with arbitrary direction in the ab plane remains unclear despite several theoretical attempts. The spin configuration of the noncollinear spin structure in the NdCuO system has been analyzed in a magnetic field parallel to the (ab) plane by Petitgrand *et al.* [19]. For the field along the [110] direction, the transition is of second order with a critical spin-flop field $H_{SF}^{[110]}$. For $H < H_{SF}^{[110]}$, the Cu-AFM vectors in the A and B units are expected to be oriented symmetrically with respect to the direction of the external field at the angle [19, 13]

$$\Phi_A = \pi/2 - \Phi_B = -\frac{1}{2}\arcsin\frac{H^2\sin 2\phi}{(H_{SF}^{[110]})^2}. \qquad (2)$$

However, it is worth noting that the angular dependence (2) seems to be applicable only in a rather narrow range near the [110] direction. For the external field along the [100] direction, the transition is of the first order with a critical spin-flop field $H_{SF}^{[100]} > H_{SF}^{[110]}$. With increasing the angle in between the [100] direction and the external field, the spin flop remains the first-order transition and smoothly approaches the second order when the external field approaches the [110] direction. However, the first-order transition for the external field turned slightly away from the [100] direction is accompanied by a relevant rotation of the Cu-AFM vectors in the A and B units [19]:

$$\Phi_A = \pi/2 - \Phi_B \approx -\frac{H^2}{(H_{SF}^{[110]})^2}\phi. \qquad (3)$$

The magnetic data on the Ce-doped system is very scant. Neutron-diffraction data [21] point to $T \approx 1.2$ K as the Nd-ordering temperature in single-crystalline sample $Nd_{2-x}Ce_xCuO_{4+\delta}$ ($x = 0.15$) that is close to $T_{N_2} \approx 1.2$ K in Nd_2CuO_4. The dilution of the Nd sublattice is expected to result in a considerable shift of the spin-reorientation transitions I–II and II–III to low temperatures.

Recent neutron studies on Pr_2CuO_4 single crystals [22] have revealed rather unexpected spin structure transformations in differently in-plane directed external magnetic fields, which may result in a revision of many earlier magnetic data for $Nd_{2-x}Ce_xCuO_{4+\delta}$ as well. First of all, the authors emphasized the quantum char-

acter of the spin system and orientational phase transitions. They have observed a novel phase transition from a noncollinear phase with orthogonal AF subsystems to a collinear one with spins oriented along the [110] direction and proposed that the transition seems to look like a conventional second order spin-flop transition only for the external magnetic field $\mathbf{H} \parallel$ [110], while, with deviation from the [110] direction, the critical field rises and the transition becomes the first order one for $\mathbf{H} \parallel$ [100] with the critical field H_C [100] = 5.4 T. In all the cases, except for $\mathbf{H} \parallel$ [110], the spin-flop state is reached only at $H \longrightarrow \infty$.

Thus, the spin-flop transition in $Nd_{2-x}Ce_xCuO_{4+\delta}$ for the external field rotated in the ab plane is remarkable for a first-to-second order crossover, which can manifest itself in AMR through the competition of two characteristic angular patterns typical for two orientations of an external field, near two high symmetry directions, [100] and [110], respectively. In the absence of an appreciable hole contribution for electron doped $Nd_{2-x}Ce_xCuO_{4+\delta}$, we may speculate that the main mechanism of the magnetoresistance anisotropy is specified by the field dependence of the activation energy for the electron transport due to the effect of the field-dependent Nd-ion crystal field (1). However, for all that, we should take into account the nonequivalence of Nd ions from different sublattices with a complex relation between the magnitude and orientation of the effective fields on Nd ions and that for the external magnetic field. Indeed, for a small external magnetic field, the Nd ions feel mainly the magnetic polarization of the Nd–Cu system somehow or other ordered by the external field, while, for a large magnetic field, the Nd ions feel mainly the magnitude and orientation of the external field. In such a case, the magnitude of the exchange field on the Nd ion appears as a peculiar border between the low-field and high-field magnetotransport behavior. We suppose the unusual transformation of the angular AMR pattern seen in Fig. 3 and the reentrant behavior of magnetoresistance at $T = 1.4$ K seen in Fig. 4 mirror a first-second order spin-flop crossover effect, on the one hand, and a specific rare-earth contribution to the magnetotransport, on the other hand. The external field $H_{ext} \approx 4.0$ T ($T = 1.4$ K), which defines a fairly narrow range of fields with a distinctly visible splitting effect and a remarkable suppression of magnetoresistance anisotropy, is believed to provide a reliable estimate of the exchange field on Nd ions. Interestingly, the 4.2 K data (Fig. 2) reveal a fairly visible lobe broadening with increasing the magnetic field, which may also be a manifestation of the remarkable nonequivalence of Nd ions from different sublattices for the external field rotated in the ab plane.

In conclusion, the nominally electron-doped $Nd_{2-x}Ce_xCuO_{4+\delta}$ ($x = 0.12$) is shown to reveal a strong low-temperature anisotropy of in-plane magnetoresistance. Specific fourfold angular magnetoresistance anisotropy reaching the magnitude of several percents

was observed in oxygen annealed $Nd_{2-x}Ce_xCuO_{4+\delta}$ films at low temperatures and in an external magnetic field up to 5.5 T. At low temperature ($T = 1.4$ K), we observed the unusual transformation of the magnetoresistance response with increasing the external magnetic field, which seems to be a manifestation of a combined effect of a crossover between the first and second order spin-flop transitions and a field-dependent rare-earth contribution to the quasiparticle magnetotransport. At present, we have uncovered only a part of the features that characterize the AMR in the NCCO system. Unfortunately, the lack of the detailed magnetic and transport information does not allow a full quantitative description of the effect. The unified and unambiguous interpretation of all the aspects of this complex effect remains a challenging problem for future experimental research and theoretical studying.

REFERENCES

1. E. B. Amitin *et al.*, Pis'ma Zh. Éksp. Teor. Fiz. **70**, 350 (1999) [JETP Lett. **70**, 352 (1999)].

2. Y. Ando, A. N. Lavrov, and K. Segawa, Phys. Rev. Lett. **83**, 2813 (1999).

3. E. Cimpoiasu, V. Sandu, C. C. Almasan, *et al.*, Phys. Rev. B **65**, 144505 (2002).

4. Y. Ando, A. N. Lavrov, and S. Komiya, Phys. Rev. Lett. **90**, 247003 (2003).

5. A. S. Moskvin and Yu. D. Panov, cond-mat/0008035; Solid State Commun. **122**, 253 (2002).

6. A. N. Lavrov, H. J. Kang, Y. Kurita, *et al.*, Phys. Rev. Lett. **92**, 227003 (2004).

7. P. Fournier, M.-E. Gosselin, S. Savard, *et al.*, Phys. Rev. B **69**, 220501 (2004).

8. Preliminary results were reported at *20th General Conference on Condensed Matter Division EPS* (Prague, 2004) (see Ref. [9]). While preparing this manuscript, we became aware of an experimental study of anisotropic in-plane magnetoresistance in lightly doped $Nd_{2-x}Ce_xCuO_4$ ($x = 0.025$) (see Ref. [10]) which results are in accordance with ours.

9. A. I. Ponomarev, L. D. Sabirzyanova, K. S. Sazonova, *et al.*, in *Book of Abstracts of 20th General Conference on Condensed Matter Division EPS* (Prague, 2004), p. 125.

10. S. Li, S. D. Wilson, D. Mandrus, *et al.*, Phys. Rev. B **71**, 054505 (2005).

11. A. I. Ponomarev, A. N. Ignatenkov, T. B. Charikova, *et al.*, Phys. Met. Metallogr. **95**, 551 (2003).

12. A. Janossy, F. Simon, and T. Feher, Phys. Rev. Lett. **85**, 474 (2000).

13. E. V. Gomonaj and V. M. Loktev, Phys. Rev. B **64**, 064406 (2001).

14. A. S. Moskvin and Yu. D. Panov, JETP **84**, 354 (1997); Phys. Status Solidi B **212**, 141 (1999); J. Phys. Chem. Solids **60**, 607 (1999).

15. A. S. Moskvin, Physica B (Amsterdam) **252**, 186 (1998).

16. A. S. Moskvin, Yu. D. Panov, and N. V. Mel'nikova, JETP **99**, 1108 (2004).

17. R. Sachidanandam, T. Yildirim, A. B. Harris, *et al.*, Phys. Rev. B **56**, 260 (1997).

18. S. Skanthakumar, J. W. Lynn, J. L. Peng, and Z. Y. Li, Phys. Rev. B **47**, 6173 (1993).

19. D. Petitgrand, S. V. Maleyev, Ph. Bourges, and A. S. Ivanov, Phys. Rev. B **59**, 1079 (1999).

20. A. S. Cherny, E. N. Khats'ko, G. Chouteau, *et al.*, Phys. Rev. B **45**, 12600 (1992).

21. J. W. Lynn, I. W. Sumarlin, S. Skanthakumar, *et al.*, Phys. Rev. B **41**, 2569 (1990).

22. V. P. Plakhty, S. V. Maleyev, S. V. Gavrilov, *et al.*, Europhys. Lett. **61**, 534 (2003).

Electron Paramagnetic Resonance
in a $Gd_{0.14}Si_{0.86}$ Amorphous Film: Bottleneck Regime

S. V. Gudenko

Russian Research Center Kurchatov Institute, pl. Akademika Kurchatova 1, Moscow, 123182 Russia
e-mail: gudenko@imp.kiae.ru
Received February 1, 2005; in final form, February 18, 2005

Electron paramagnetic resonance (EPR) in a $Gd_{0.14}Si_{0.86}$ amorphous film is studied over a wide temperature range from 4 to 300 K. The experimental results are analyzed with regard to the strong structural disorder in the system under study. This disorder leads to the formation of droplets, that is, regions with a high density of electronic states. It is shown that the observed EPR signal can be formed only in the double bottleneck regime, and temperature dependences are obtained for the line position and width. The spin-lattice relaxation rates for electrons and Gd ions, the second spectral moment of the line, the ferromagnetic transition temperature, the number of Gd atoms in the droplets, and the product of the electron density of states by the exchange coupling constant between electrons and Gd ions are evaluated from comparison with experimental data. The values obtained corroborate the validity of the assumptions that the double bottleneck conditions are fulfilled and structural and phase nanoscale inhomogeneities exist in the system. © 2005 Pleiades Publishing, Inc.

PACS numbers: 75.30.–m, 76.30.–v

1. INTRODUCTION

In recent years, amorphous silicon-based alloys doped with rare-earth (RE) elements RE_xSi_{1-x} (RE = Gd, Tb, Y) have been studied intensively because of their unusual magnetic and transport properties and their possible use in optoelectronics [1]. The high degree of disorder in the system due to the amorphous structure of the alloys and the occurrence of intrinsic defects, which are formed, for example, by numerous dangling bonds, unfilled vacancies, etc., leads to noticeable spatial fluctuations in the concentration of the rare-earth impurity and to a redistribution of the electron density in the bulk of the material. As a result, regions with an increased electron concentration (droplets) arise, and local ferromagnetic order can appear in them for magnetic RE elements because of RKKY interaction [2]. It is magnetic ordering in the droplets that is responsible both for a significant difference in the transport properties of Gd_xSi_{1-x} samples as compared to their nonmagnetic Y_xSi_{1-x} analogues and for the effect of giant negative magnetoresistance [3].

In this work, the magnetic properties of a $Gd_{0.14}Si_{0.86}$ amorphous alloy have been studied by the electron spin resonance (EPR) technique. Previously, the magnetic properties of Gd_xSi_{1-x} amorphous films were studied as functions of their composition ($x = 0.002$–0.1) in [4] by EPR and Quantum Design SQUID dc magnetometry. It was shown that Gd occurred in the trivalent state Gd^{3+} ($4f^7$, $S = 7/2$, $L = 0$) with the spectroscopic splitting factor close to $g = 2$. The line width determined as the field distance between peaks of the derivative of the absorption curve was independent of the Gd concentration

within the experimental error and was $dH_{pp} = 800 \pm 50$ G for temperatures $T > 30$ K and at the frequency $\nu \cong 9.48$ GHz. Based on this result, the conclusion was drawn that the majority of Gd atoms enter into the composition of the stable $GdSi_2$ complex. The independence of the line width on the concentration of Gd ions is rather surprising, because, for example, the dipole–dipole broadening alone comprises more than 1.5 kG at a concentration of about 10 at. %; however, this circumstance was not explained at all in [4]. The complete absence of any evidence of the fine structure in spite of the definitely noncubic structure of $GdSi_2$ complexes and the rather high spin $S \gg 1/2$ is also not clear.

2. EXPERIMENTAL PROCEDURE

The measurements were performed with a $Gd_{0.14}Si_{0.86}$ amorphous film 1.3 µm thick fabricated in the laboratory headed by Prof. F. Hellman (Department of Physics, University of California, San Diego) by electron beam coevaporation [5] onto a crystalline NaCl substrate. The film area was about 10 mm². To perform the experiments, the film (after dissolving the NaCl substrate) was fixed on a quartz holder installed in the goniometer of the resonator. The accuracy of adjusting the angle between the film plane and the magnetic field direction was no worse than 0.5°. The spectra were recorded on a Bruker ESP-300 EPR spectrometer equipped with a helium flow cryostat (Oxford Instruments). The experiments were carried out in the temperature range from 4 to 300 K at the frequency $\nu \cong$ 9.46 GHz for two orientations of the magnetic field,

namely, parallel and perpendicular to the film plane. Conventionally, the first derivative of the absorption signal was recorded.

3. EXPERIMENTAL RESULTS

The absorption spectrum observed for both orientations of the magnetic field consisted of one line. At temperatures $T \geq 30$ K, the line shape rather well corresponded to a Lorentzian curve. As the temperature decreased below 30 K, the line changed, becoming close in shape to a Gaussian curve at $T \leq 20$ K. The line width dH_{pp} (Fig. 1) depended rather weakly on the temperature in the region $T \geq 50$ K and was about 800 G as in [4]. However, as distinct from [4], a line width minimum about 100 G deep was observed in this work in the temperature range 120–180 K. As the temperature decreased below 50 K, the line broadened rapidly, and its observation became impossible at a temperature of about 5 K. The resonance field for both orientations (Fig. 2) at temperatures $T \geq 100$ K decreased approximately linearly with increasing temperature. The field strength for the perpendicular orientation was higher over the entire range of the studied temperatures. This distinction increased with decreasing temperature and reached a value of about $H_{r\perp} - H_{r\parallel} \approx 300$ G at a temperature of 10–15 K. At a temperature of about 300 K, the average (between the orientations) field strength corresponded to a g factor close to 2. The magnetic susceptibility obtained by the double integration of the spectra obeyed the Curie–Weiss law $\chi = C/(T - \theta)$ at temperatures of $T \geq 100$ K quite well with a small negative temperature $\theta \approx -30$ K. The absolute calibration of the susceptibility was performed in this region, where the constant C was taken equal to $C = S(S + 1)g_{Gd}^2\mu_B^2 N_{Gd}/3k_B$. Here, $S = 7/2$, $g_{Gd} = 2$, and $N_{Gd} = 7 \times 10^{21}$ cm^{-3} are the spin, g factor, and concentration of Gd ions, respectively; μ_B is the Bohr magneton; and k_B is the Boltzmann constant. In Fig. 3, the susceptibility is evaluated in terms of the magnetic moment per Gd ion in the resonance field. As the temperature decreased below 100 K, θ decreased in absolute value and even became positive (≈ 5 K). The susceptibility itself reached a maximum at a temperature of $T \cong 12$ K and then sharply dropped. As is known [6], the sign of the RKKY interaction depends on the electron density and distance between the ions. For inhomogeneous systems, the change in the sign of θ can be due to a change in the relative contribution to the susceptibility from the regions with ferromagnetic and antiferromagnetic interactions.

4. DISCUSSION

There are several different sources of the EPR signal in the system under study: Gd ions residing in the matrix and in the droplets with a higher electron density as well as electrons themselves. The Gd ions experience a crystal field of noncubic symmetry [4], which
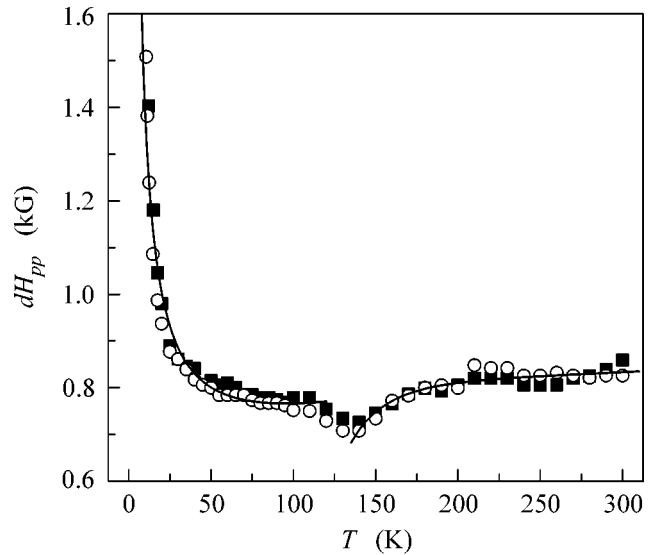
Fig. 1. Temperature dependence of the EPR line width dH_{pp} at the frequency $\nu \cong 9.46$ GHz when the magnetic field is (■) perpendicular and (○) parallel to the film plane. The solid curves are obtained by Eqs. (12) and (13) at the optimal values of the parameters (see the text).
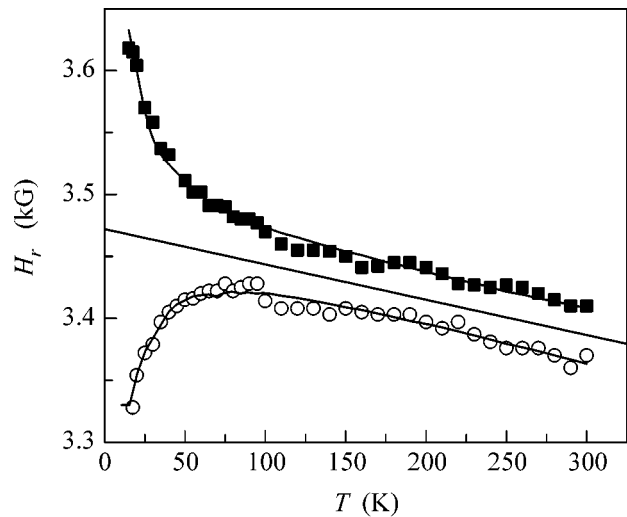

Fig. 2. Same as in Fig. 1, but for the resonance field strength. The solid curves are obtained by Eq. (18) with the parameters $H_0 = 3470$ G, $l = -0.3$ G/K, and $\beta = 0.95$ or -0.7 for the magnetic field perpendicular or parallel to the film plane, respectively. The straight line corresponds to $\beta = 0$.

must lead to the fine splitting of the line at $S = 7/2 > 1/2$. The absence of signals of various types, the absence of the fine structure, and the Lorentzian line shape indicate that the double bottleneck conditions are fulfilled [7]. In this case, first, the exchange interaction of Gd ions with electrons leads to the disappearance of the fine structure and the separate signals from these ions and electrons inside each Gd subsystem, and, second,
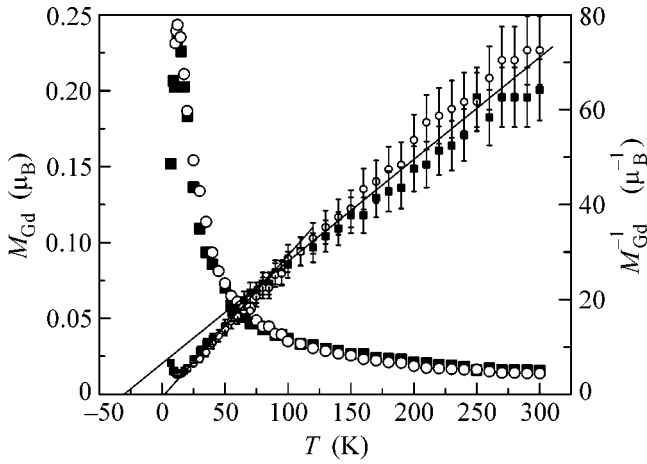
Fig. 3. Temperature dependence of the magnetic moment per Gd ion in the resonance field for two orientations of the magnetic field with respect to the film plane. The designations of experimental points are the same as in Fig. 1. The straight lines correspond to the Curie–Weiss law $M_{Gd}^{-1} \propto T - \theta$.

the interaction between subsystems is sufficiently strong for the formation of one common EPR signal from these subsystems.

If the bottleneck conditions are fulfilled for two subsystems whose fundamental resonance frequencies and susceptibilities are ω_1, ω_2 and χ_1, χ_2, respectively, then the complex frequency of the common resonance is determined by the expression [7]

$$\omega^* \cong \frac{\chi_1 \omega_1 + \chi_2 \omega_2}{\chi_1 + \chi_2}. \tag{1}$$

The real part of this expression determine the line position, and the imaginary part determines the line width. Using this formula, first inside each subsystem (for electrons and Gd ions), then for the interacting subsystems, and applying the theory developed in [7], one can obtain equations for the line position ω_r and the line width $d\omega$

$$\omega_r = \mathrm{Re}\,\omega^* \cong \omega_s^0 \left[1 + \frac{\lambda}{\chi_1 + \chi_2} \right.$$
$$\left. \times \left(\frac{M_2^{(1)}(1-f)\chi_e^{(1)}\chi_1}{(3/T_{1e})^2} + \frac{M_2^{(2)} f \chi_e^{(2)}\chi_2}{(3/T_{2e})^2} \right) \right], \tag{2}$$

$$d\omega = \mathrm{Im}\,\omega^* \cong \frac{1}{T_{sL}} + \frac{(1-f)\chi_e^{(1)} + f\chi_e^{(2)}}{\chi_1 + \chi_2} \frac{1}{T_{eL}}$$
$$+ \frac{1}{\chi_1 + \chi_2} \left(\frac{M_2^{(1)}\chi_1}{(3/T_{1e})} + \frac{M_2^{(2)}\chi_2}{(3/T_{2e})} \right). \tag{3}$$

Here,

$$\frac{1}{T_{se}} = \frac{1}{T_{1(2)e}} \cong \frac{4\pi}{\hbar}(\rho_{1(2)}J)^2 k_B T \tag{4}$$

is the Korringa relaxation rate of ions on electrons; $1/T_{eL}$ and $1/T_{sL}$ are the spin-lattice relaxation rates of electrons and ions; ω_s^0 is the resonance frequency of isolated Gd spins disregarding their interactions with the lattice and with each other; $\lambda = 2J/(g_s g_e \mu_B^2)$ is the molecular field constant; the interaction between electrons and Gd ions is described by the Hamiltonian $H_{ex} = -2\sum_j J\mathbf{S}\mathbf{s}(\mathbf{r}_j)$; $\mathbf{s}(\mathbf{r}_j)$ is the electron spin density at an S ion location point;

$$\chi_e^{(1,2)} \cong \frac{1}{2} g_e^2 \mu_B^2 \rho_{1(2)} \tag{5}$$

and $\chi_{1(2)}$ are the magnetic susceptibilities of electrons and ions per lattice site; $M_2^{(1,2)}$ is the second spectral moment of Gd ions due to anisotropic spin–spin interactions, fine and hyperfine structures, and other sources of inhomogeneous broadening; g_e and g_s are the electron and ion g factors, respectively; $\rho_{1(2)}$ is the electron density of states at the Fermi level per lattice site; f is the volume fraction of droplets; and $\hbar$ is the Planck constant. From here on, subscripts 1 and 2 correspond to the matrix and droplets, respectively. The electron density of states in the droplets ρ_2 is considerably higher than the density ρ_1 in the matrix. Their ratio $A = \rho_2/\rho_1 \cong 3.6$ was obtained in [2] from rather general assumptions considering that the volume fraction of droplets was approximately $f \cong 0.1$ and the ratio of the total concentrations of Gd atoms in the droplets and in the matrix was $c_2/c_1 \approx 0.5$. These values will also be used below for various estimations. The trivalent Gd^{3+} ion in the silicon matrix serves as a donor, supplying one electron to the matrix. Assuming that the concentration of silicon atoms is $N_{Si} \cong 5 \times 10^{22}$ cm^{-3} [2, 5] and the relative concentration of Gd^{3+} ions is $c = c_1 + c_2 = 0.14$, one can estimate the density of states in the simplest free electron model $k_B\rho \approx 10^{-5}$ K^{-1}. The characteristic value of the exchange integral for RE elements is $|J| \approx 10^3$ K $\times k_B$.

Because the electron density is relatively small, the interaction of Gd ions in the matrix will be considered weak over the entire temperature range; therefore, for these ions

$$\chi_1 \cong \frac{c_1 S(S+1) g_s^2 \mu_B^2}{3k_B T}. \tag{6}$$

In accordance with the model developed in [2], a local ferromagnetic transition takes place at a certain temperature $T = T_D$ in the droplets. Therefore, for the Gd sus-

ceptibility in the droplets above the T_D point in the paramagnetic phase, it will be assumed that

$$\chi_{2HT} \approx \frac{c_2 S(S+1) g_s^2 \mu_B^2}{3 k_B (T - T_D)}. \qquad (7)$$

In the region $T < T_D$, the droplets containing K Gd ions will be considered as *superparamagnetic* particles with the spin KS. The interaction between them, as well as between separate matrix Gd ions, is realized through electrons with the density ρ_1; therefore, similar to Eq. (6), their susceptibility can be estimated as

$$\chi_{2LT} \cong \frac{c_2 S(KS+1) g_s^2 \mu_B^2}{3 k_B T}. \qquad (8)$$

Let us introduce the relaxation rate of electrons on ions S (Overhauser relaxation) $\frac{1}{T_{es}} \cong \frac{8\pi c}{3\hbar} S(S+1)\rho J^2$. At the values of the parameters indicated above, the following inequalities are fulfilled well in the entire range of studied temperatures: $1/T_{es} \gg 1/T_{se}$, $1/T_{es} > |\lambda\chi_s\omega_e|$, $1/T_{se} > |\lambda\chi_e\omega_s|$, and $\chi_s \gg \chi_e$. Here, for the estimation of the resonance frequencies of the ions and electrons, it was assumed that $\omega_s \cong \omega_e \cong 2\pi \times 10^{10}$ s^{-1}. With the additional suggestion on the values of spin-lattice relaxation

$$\frac{1}{T_{eL}} \gg \frac{1}{T_{sL}}, \qquad (9)$$

the double bottleneck conditions are reduced to the inequality [7]

$$\frac{1}{T_{eL}} < \frac{1}{T_{es}} \approx 3 \times 10^{13} \text{ s}^{-1}. \qquad (10)$$

In addition, a necessary condition for the applicability of Eqs. (2) and (3) is the fulfillment of the inequality

$$\left| \frac{3}{T_{se}} + i\lambda\chi_e\omega_s^0 \right| \gg \sqrt{M_2}, \qquad (11)$$

which determines the exchange narrowing in the case when the second moment M_2 is noticeable.

By virtue of the latter condition, the line shift determined by Eq. (2) turns out to be much smaller than the Knight shift [7] $|\Delta\omega_r/\omega_s^0| \ll |\lambda\chi_e| \cong |\rho J| \approx 10^{-2}$ and the shift rapidly decreases with increasing temperature.

In the second term in Eq. (3) for the line width, the numerator does not depend on the temperature and the denominator involves the total susceptibility of the system $\chi_{exp} = \chi_1 + \chi_2$, which is inversely proportional to the temperature to a rather good accuracy (see Fig. 3). Hence, similar to Korringa relaxation, this term must make a contribution linear in temperature to the line width. The form of the temperature dependence and, correspondingly, the contribution of the third term to the line width are determined by the ratio of the second moments and susceptibilities of the subsystems and can

qualitatively differ for different temperature ranges. The distinction of the subsystems in the paramagnetic region at $T > T_D$ is mainly determined by the difference in the electron densities of states, which does not directly affect the second moment; therefore, for this region, it will be assumed that $M_2^{(1)} \cong M_2^{(2)} = M_2$. As the temperature approaches T_D, the relative contribution to the line width from the droplets will increase in accordance with Eqs. (6) and (7). With regard to the relation $\rho_2 \gg \rho_1$, this means a decrease in the contribution to the line width from the third term in Eq. (3).

Assuming that the main contribution to the second moment is due to the uniaxial anisotropy of the crystal field of the form $H_1 = -D S_z^2$, one can estimate the ratio of the second moments in the region $T < T_D$. Under the assumption of random distribution of the local axes of crystallites, averaging over the droplets containing K Gd ions yields $M_2^{(2)}/M_2^{(1)} \cong 1/K$. Now, taking into account the above comments, it is easy to obtain the wanted expressions for the line width by the field in various temperature ranges based on Eqs. (3)–(8)

$$dH_{ppHT} = dH_{sL} + \frac{b_{HT}}{\chi_{exp}} + \frac{P}{T}\left[\left(1 + \frac{c_2}{c_1}\frac{T}{T - T_D}\right)^{-1}\right.$$
$$\left. + A^{-2}\left(1 + \frac{c_1}{c_2}\frac{T - T_D}{T}\right)^{-1}\right] + dH_0, \qquad (12)$$

$$dH_{ppLT} = dH_{sL} + \frac{b_{LT}}{\chi_{exp}} + \frac{LP}{T} + dH_0. \qquad (13)$$

Here,

$$dH_{sL} = \frac{2}{\sqrt{3}}\frac{\hbar}{g\mu_B}\frac{1}{T_{sL}}, \qquad (14)$$

$$b_{HT(LT)} = \frac{\hbar\mu_B g_e^2 \rho_1 [1 + f(A - 1)]}{\sqrt{3}g}\frac{1}{T_{eL}}, \qquad (15)$$

$$P = \frac{1}{6\pi\sqrt{3}}\frac{\hbar^2 M_2}{g\mu_B k_B (\rho_1 J)^2}, \qquad (16)$$

$$L = \left(1 + \frac{c_2}{c_1}\frac{S}{S+1}\right)\left(1 + \frac{c_2}{c_1}\frac{KS}{S+1}\right)^{-1}, \qquad (17)$$

and the quantity dH_0 describes line broadening due to all other mechanisms that were disregarded in our model.

The solid curves in Fig. 1 correspond to Eqs. (12) and (13) with the parameters $dH_{sL} + dH_0 = 607$ G, $b_{HT} = 8 \times 10^{-5}\mu_B$, $b_{LT} = 12 \times 10^{-5}\mu_B$, $P = 56562$ G K, $T_D = 137$ K, $L = 0.134$, $c_2/c_1 = 0.5$, and $A = 3.6$. The two latter parameters were fixed in accordance with the estimates given in [2], and the other parameters were selected using the standard least-squares procedure. It is evident

that the experimental curves are described rather well by Eqs. (12) and (13): the deviation does not exceed the scatter of the experimental points in the entire temperature range except for the narrow region $T = 120–130$ K. The g factor in Eqs. (14)–(16) is directly determined from the value of the resonance field disregarding its shift due to the demagnetization effect associated with the shape of the sample. As will be shown below, it can be assumed that $g = 2$ with an accuracy of no worse than 2–3%, and the product $\rho_1 J \cong -2.5 \times 10^{-2}$ can be estimated from the line shift obtained when the temperature tends to zero. For the electron density of states, it is assumed, as previously, that $k_B \rho_1 \approx 10^{-5}$ K^{-1}. The g factor for electrons usually also differs only slightly from $g_e = 2$ [8, 9]. Now, the use of Eqs. (14)–(17) gives the following estimates: $1/T_{sL} \leq 10^{10}$ s^{-1}, $1/T_{eL} \approx 10^{12}$ s^{-1}, $\hbar^2 M_2 \cong 0.16(k_B K)^2$, and $K \cong 24$.

It is evident that the assumptions for the relaxation rates (9) and (10) are fulfilled well. Moreover, relationship (11) is fulfilled rather well at $T > 10–20$ K; hence, the system occurs in the double bottleneck regime, and the use of Eqs. (1)–(3) is fully justified.

For a specified concentration of Gd ions, the second moment conditioned by the dipole–dipole interaction can be readily estimated $\hbar^2 M_{2dd} \cong 0.024(k_B K)^2$. It is evident that its value is almost an order of magnitude smaller than the estimate that was obtained here for the total moment M_2. This circumstance explains the independence of the line width of the concentration of Gd up to a level of 10–20 at. % and allows the inference that the single-ion contribution to the resulting value of the second moment dominates. In other words, this means that the main contribution to the second moment is not associated with the interaction of Gd ions with each other but is due to either their interaction with the nearest local environment, for example, crystal field, or hyperfine interaction. The hyperfine coupling constants for ^{155}Gd and ^{157}Gd are sufficiently small [10, 11] and yield a splitting value of $\approx$3–5 G, which is much less than the characteristic line width. Moreover, their total relative natural concentration is less than 30%. Thus, it is most likely that the second moment is conditioned just by the crystal field of the nearest neighbors. Under the assumption of the uniaxial anisotropy of the crystal field, its parameter $D \cong 0.14$ ($K k_B$) can be readily estimated (for $S = 7/2$ and the random distribution of the crystallite axes $M_2 \cong 8D^2$ [12]).

As was shown in [13], the change in the value of the resonance field with decreasing temperature can be related to, among other things, the increase in the magnetization M of the sample. It depends on the shape of the sample and the character of the arrangement of ions—the sources of the EPR signal—in the crystal lattice. For ions located at the crystal lattice sites of a cubic symmetry and also in the case of their isotropic random arrangement, the additional shift in the resonance field for the observation of EPR in a thin film equals $\Delta H_{r\perp} = 4\pi M$ for the magnetic field parallel to the film plane and $\Delta H_{r\parallel} = -2\pi M$ for the magnetic field perpendicular to the film plane. In accordance with these facts and taking into account the linear behavior, which is clearly seen at high temperatures, an attempt was made to describe the temperature dependence of the resonance field by the curve

$$H_r = H_0 + \beta 4\pi M + lT. \tag{18}$$

The solid lines in Fig. 2 are obtained by Eq. (18) with the parameters $H_0 = 3470$ G, $l = -0.3$ G/K, and $\beta = 0.95$ or -0.7 for the magnetic field perpendicular or parallel to the film plane, respectively. The value $M = M_{Gd} N_{Gd}$ was recalculated directly from the experimental susceptibility data (Fig. 3). It is evident that the experimental curves are rather well described by the dependence corresponding to Eq. (18). A significant difference of the value of β from -0.5 for the parallel orientation of the field points most likely to the occurrence of short-range order of a noncubic symmetry in the arrangement of Gd ions. This may indicate that the formation of droplets and the ordering of Gd ions in these droplets are of a chemical nature. The straight line in Fig. 2 corresponds to $\beta = 0$. It characterizes the value of the resonance field without its shift due to the magnetization of the sample. This determination of the resonance field allows the value of the g factor to be obtained more correctly. The value H_0 corresponds to the resonance field that would be observed at $T \longrightarrow 0$. The value of the g factor in this case is $g_0 = 1.95 < 2$. As was already mentioned, the line shape approached a Gaussian curve as the temperature decreased below 20 K. This fact points to slowing down of exchange fluctuations and to the escape of the system from the bottleneck regime. Slowing down of exchange fluctuations is most likely related to the approach of a phase transition to a spin glass state [3, 5, 14–16]. In our work, the occurrence of a phase transition is indicated by both the maximum of the susceptibility ($T_m \approx 12$ K) and the disappearance of the EPR signal itself at a lower temperature ($T_{SG} \approx 5–6$ K). Under these conditions, electrons rather rapidly relax to the lattice and their magnetization has time to follow the instant value of the internal field [7]. This leads to a shift of the resonance field (Knight shift), whose value is determined by the known equation $\Delta g/g = \lambda \chi_e = (g_e/g)\rho J$. To an accuracy of tenths of a percent, the value of the g factor for noninteracting S ions Gd^{3+} does not differ from 2 [10]. Hence, using the experimental value $\Delta g = 2 - g_0 = 0.05$, one can easily obtain the estimate used above for the value $\rho_1 J \cong -2.5 \times 10^{-2}$ and, assuming that $k_B \rho_1 \approx 10^{-5}$ K^{-1}, the value of the exchange constant $J \approx -2.5 \times 10^3$ (K k_B).

5. CONCLUSIONS

Experimental results were analyzed with regard to the strong structural disorder of the system under study,

leading to the formation of droplets, that is, regions with a high electron density of states. It was shown that the observed EPR signal could be formed only under the double bottleneck conditions. Relaxation rates were estimated, and relationships were obtained whose fulfillment was necessary for the accomplishment of these conditions in the system under study. Equations were obtained that described the temperature dependences of the line position and width in the system in which a local ferromagnetic transition occurred in the droplets. With an optimized selection of parameters, the equation for the line width described well the experimental data. The most important parameters that were estimated in this way are the spin-lattice relaxation rates for electrons $1/T_{eL}$ and for ions $1/T_{sL}$, the second spectral moment of the line M_2, the crystal field parameter D, the ferromagnetic transition temperature T_D in the droplets, and the number K of Gd atoms in the droplets. The values of the relaxation rates obtained experimentally corroborated the correctness of the assumption that the system occurred under the double bottleneck conditions. The value of M_2 turned out to be almost an order of magnitude larger than the second moment given by the dipole–dipole interaction. This explained well the independence of the line width from the concentration of Gd, which also counted in favor of the bottleneck regime. Finally, an analysis of the temperature dependence of the line position with regard to the effect of the sample magnetization allowed the conclusion that short-range order of a noncubic symmetry occurred in the system of Gd ions and gave an estimate for the product $\rho_1 J$ of the electron density of states by the exchange coupling constant between electrons and Gd ions.

REFERENCES

1. *Rare-Earth Doped Semiconductors II*, Ed. by S. Coffa, A. Polman, and R. Schwartz (Mater. Res. Soc., Pittsburgh, 1996), Mater. Res. Soc. Symp. Proc., Vol. 422.

2. S. Caprara, V. V. Tugushev, and N. K. Chumakov, Zh. Éksp. Teor. Fiz. (2005) (in press).

3. F. Hellman, M. Q. Tran, A. E. Gebala, *et al.*, Phys. Rev. Lett. **77**, 4652 (1996).

4. M. S. Sercheli, C. Rettori, and A. R. Zanatta, Braz. J. Phys. **32** (2A), 409 (2002).

5. W. Teizer, F. Hellman, and R. C. Dynes, Phys. Rev. Lett. **85**, 848 (2000).

6. K. Yosida, Phys. Rev. **106**, 893 (1957).

7. S. E. Barnes, Adv. Phys. **30**, 801 (1981).

8. S. A. Al'tshuler and B. M. Kozyrev, *Electron Paramagnetic Resonance* (Fizmatgiz, Moscow, 1961; Academic, New York, 1964).

9. R. J. Elliott, Phys. Rev. **96**, 266 (1954).

10. S. A. Al'tshuler and B. M. Kozyrev, *Electron Paramagnetic Resonance in Compounds of Transition Elements*, 2nd ed. (Nauka, Moscow, 1972; Halsted, New York, 1975).

11. D. R. Hutton and G. J. Troup, Br. J. Appl. Phys. **15**, 405 (1964).

12. D. L. Huber, G. Alejandro, A. Caneiro, *et al.*, Phys. Rev. B **60**, 12155 (1999).

13. I. Svare and G. Seidel, Phys. Rev. **134**, A172 (1964).

14. B. L. Zink, E. Janod, K. Allen, *et al.*, Phys. Rev. Lett. **83**, 2266 (1999).

15. F. Hellman, D. R. Queen, R. M. Potok, *et al.*, Phys. Rev. Lett. **84**, 5411 (2000).

16. B. L. Zink, V. Preisler, D. R. Queen, *et al.*, Phys. Rev. B **66**, 195208 (2002).

Translated by A. Bagatur'yants

Negative Magnetoresistance of a High-Mobility Two-Dimensional Electron Gas in a Nonlinear Regime

A. A. Bykov, A. K. Kalagin, and A. K. Bakarov

Institute of Semiconductor Physics, Siberian Division, Russian Academy of Sciences, Novosibirsk, 630090 Russia
e-mail: bykov@thermo.isp.nsc.ru
Received March 24, 2005

The effect of the measuring current I_{dc} on the magnetoresistance (MR) of a high-mobility two-dimensional electron gas (2DEG) in a GaAs quantum well with AlAs/GaAs superlattice barriers has been studied. It has been found that, as I_{dc} increases, the MR of the 2DEG in the studied structures becomes negative in the range of classically strong magnetic fields. It has been shown that the observed negative MR is due to the transport of the 2DEG in the nonlinear regime. © 2005 Pleiades Publishing, Inc.

PACS numbers: 73.23.–b, 73.40.Gk

Recent experiments have led to the discovery of a new type of magnetotransport effects occurring in a high-mobility two-dimensional electron gas (2DEG) in the region of classically strong magnetic fields under the action of microwave radiation [1–6] and a constant electric field [7]. These experiments stimulated the development of a theory explaining the observed effects [8–13]. In particular, it has recently been proved theoretically in [14] that the character of scattering in the high-mobility 2DEG with large filling factors depends strongly on the magnitude of the constant electric field and may change substantially when the linear regime changes to the nonlinear one.

For the high-mobility 2DEG in the range of classically strong magnetic fields in the linear regime, this theory predicts positive magnetoresistance (MR). This circumstance is due to the memory effects in the 2DEG magnetotransport [15], which means that the probability that an electron returns to the same scattering impurity after a scattering event increases with the magnetic field. At the same time, the probability of returning the electron to the initial point decreases as the electric field increases. Consequently, the MR of the high-mobility 2DEG in the region of a classically strong magnetic field must change upon a transition from the linear to nonlinear regime.

Here, we study the MR of the high-mobility 2DEG in a quantum well with AlAs/GaAs superlattice barriers in the linear and nonlinear regimes. It has been found that the MR of the high-mobility 2DEG in such selectively doped structures becomes negative in the region of classically strong magnetic fields upon an increase in the direct pulling current I_{dc}. It has been shown experimentally that the observed negative MR is associated with magnetotransport in the 2DEG in the nonlinear regime.

The selectively doped structures studied here were grown using molecular beam epitaxy (MBE) on (100) GaAs substrates. The width of the GaAs quantum well was 13 nm. AlAs/GaAs type II superlattices served as the barriers [16]. The mobility and concentration of the
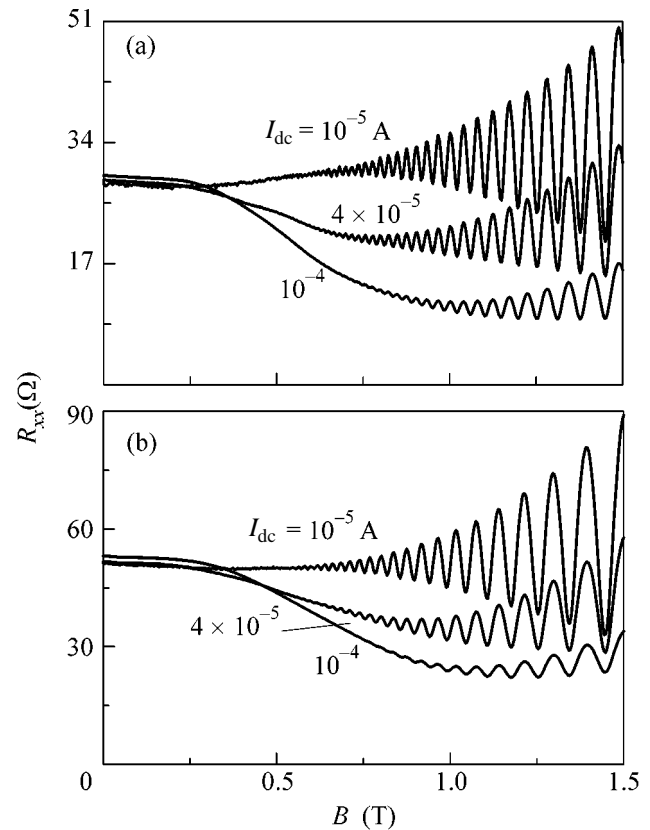

Fig. 1. Dependence $R_{xx}(B)$ at $T = 4.2$ K for samples with a mobility of (a) 0.8×10^6 and (b) 0.5×10^6 cm^2/(V s) for various I_{dc} values.
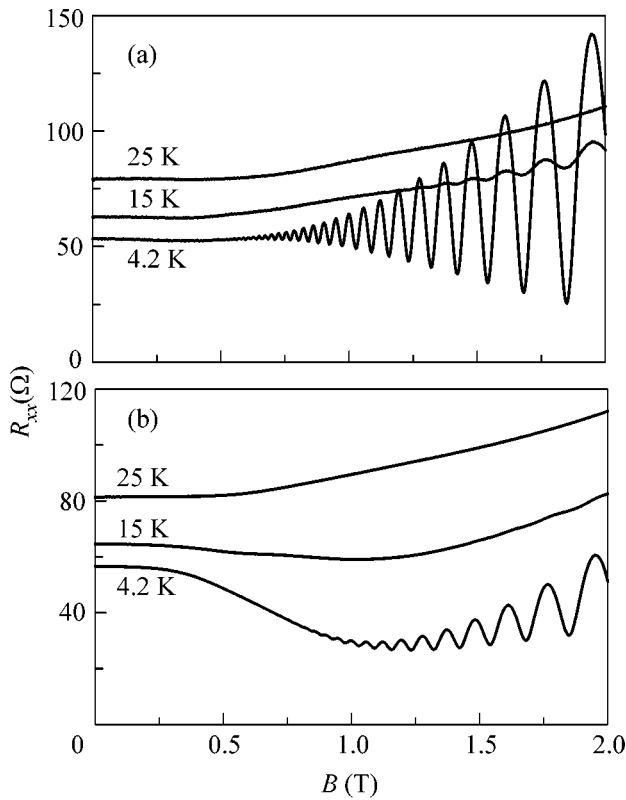
Fig. 2. Dependence $R_{xx}(B)$ for a sample with a mobility of 0.5×10^6 cm^2/(V s) at $I_{dc} =$ (a) 10^{-6} and (b) 10^{-4} A for various temperatures.

Fig. 3. Dependence $R_{xx}(B)$ for a sample with a mobility of 0.8×10^6 cm^2/(V s) at $I_{dc} =$ (a) 10^{-6} and (b) 10^{-4} A for various temperatures.

2DEG in the initial MBE structures at liquid helium temperature were $\mu = (0.5–1) \times 10^6$ cm^2/(V s) and $n_s = (0.9–1.3) \times 10^{12}$ cm^{-2}, respectively. The measurements were carried out in magnetic fields up to 2 T on Hall bridges 50 μm wide with a distance of 200 μm between the potentiometer terminals. The MRs of two groups of samples that were prepared from two different MBE structures with different mobilities and concentrations were studied in detail. The resistance was measured in a direct current varying between 10^{-6} and 3.5×10^{-4} A in the temperature range from 4.2 to 25 K.

Figure 1 shows the typical dependences of the MR of the 2DEG at $T = 4.2$ K for various values of the measuring current I_{dc} for samples with different mobilities. It is seen that, as I_{dc} increases, the amplitude of the Shubnikov–de Haas (SdH) oscillations decreases and a pronounced negative MR appears. Figure 2 shows the typical $R_{xx}(B)$ curves for samples with a lower mobility for various temperatures at $I_{dc} = 10^{-6}$ and 10^{-4} A. It follows from these experimental curves that an increase in temperature not only suppresses the SdH oscillations but also leads to the appearance of a positive MR, which is completely consistent with the theory proposed in [14]. The MR of the 2DEG that is measured for $I_{dc} = 10^{-4}$ A reverses its sign with an increase in tem-
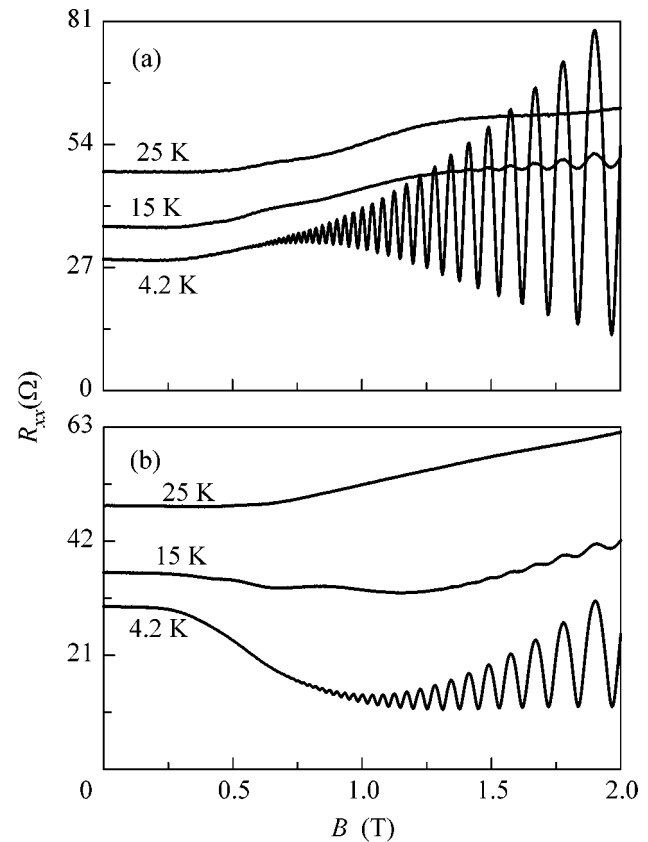
perature; i.e., the negative MR becomes positive. A qualitatively similar behavior is also observed for samples with a higher mobility (see Fig. 3). However, in this case, an oscillating component (which is not observed at $T = 4.2$ K) appears against the background of positive MR. One of the possible causes for the appearance of this component in samples with a higher mobility (and, hence, a higher concentration) is the filling of the second size quantization level, which is corroborated by the absence of this component for samples with a lower concentration.

The appearance of negative MR upon an increase in I_{dc}, which is observed in Fig. 1, may be due to at least two causes. One of them is the increase in the electron temperature as a result of the heating of the 2DEG. This behavior is corroborated by a decrease in the amplitude of the SdH oscillations with increasing I_{dc}. Another cause is a change in the scattering cross section in a constant electric field [14]. The magnetic field dependences of the MR of the 2DEG at various temperatures (Figs. 2 and 3) for all the samples studied here show that an increase in temperature leads to the appearance of positive MR, to an increase in the resistivity in zero magnetic field, and to the suppression of the SdH oscillations. Such an effect of temperature of the MR of the 2DEG suggests that an increase in the electron temper-
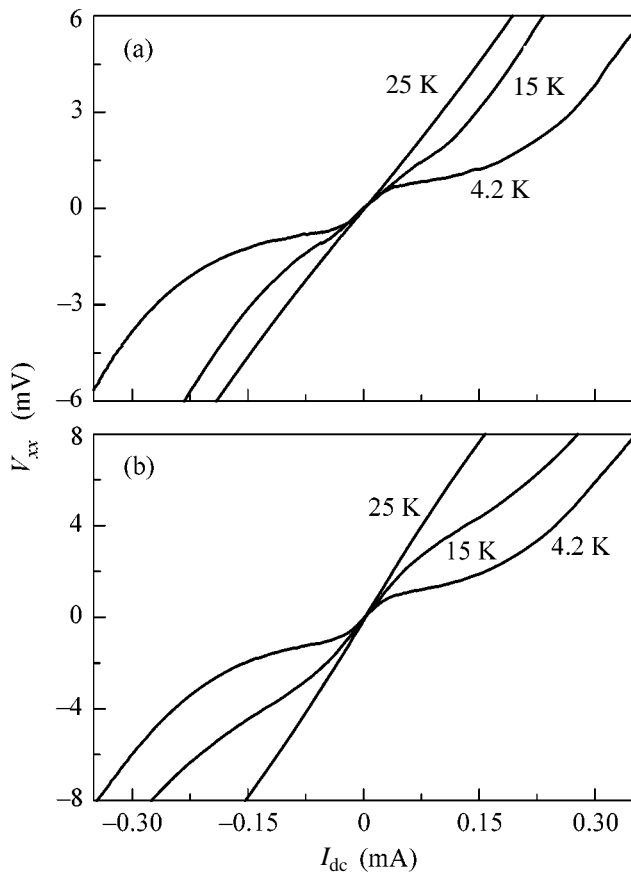
Fig. 4. Current–voltage characteristics of a sample with a mobility of 0.8×10^6 cm^2/(V s) for (a) $T = 4.2$ K and the magnetic field $B = (1)$ 0, (2) 0.6, and (3) 1.2 T and (b) $B = 1$ T and various temperatures.

ature with increasing I_{dc} cannot be responsible for the appearance of negative MR in the samples under investigation.

Another most probable cause for the appearance of negative MR in the 2DEG with increasing I_{dc} is the effect of the electric field on the scattering cross section. In this case, the current–voltage characteristic (CVC) of the resistance of the 2DEG must be nonlinear [14]. Figure 4a shows the CVCs recorded at a temperature of 4.2 K in various magnetic fields. Indeed, it is seen in the figure that the CVC becomes nonlinear as the magnetic field increases. With an increase in I_{dc}, the slope of the CVC becomes equal to the slope of the CVC for zero magnetic field in agreement with the theory. Such a behavior indicates that, above a certain critical current j_0, the probability that an electron returns to the region of its previous scattering becomes insignificant and this process does not affect the magnetotransport. Figure 4b shows that the CVC in a nonzero magnetic field also becomes linear with increasing temperature.

The j_0 value above which the slope of the CVC is determined by the transport relaxation time in zero magnetic field [14] is determined by the expression $j_0 =$

$en_s \xi \omega_c / 2\pi$, where ξ is the correlation length of the scattering potential. Using the j_0 value determined from the CVC, we estimated the correlation length of the scattering potential in our samples as 5–10 nm. This estimate coincides in order of magnitude with the distance between the GaAs quantum well and δ-doped layers in our structures, and it agrees with the generally accepted estimates of the correlation length of the scattering potential in high-mobility structures with modulated doping.

Thus, we have observed a negative MR of the 2DEG in the GaAs quantum well with AlAs/GaAs superlattice barriers. This negative MR arises when the direct pulling current increases, and it is shown to be associated with the nonlinearity of the CVC. Our results are consistent with the theory of the magnetotransport of the high-mobility 2DEG with large filling factors in the nonlinear regime [14].

REFERENCES

1. M. A. Zudov, R. R. Du, J. A. Simmoms, *et al.*, Phys. Rev. B **64**, 201311(R) (2001).
2. R. Mani, J. H. Smet, K. von Klitzing, *et al.*, Nature **420**, 646 (2002).
3. I. V. Kukushkin, J. H. Smet, V. I. Fal'ko, *et al.*, Phys. Rev. B **66**, 121306(R) (2002).
4. M. A. Zudov, R. R. Du, L. N. Pfeiffer, *et al.*, Phys. Rev. Lett. **90**, 046807 (2003).
5. S. I. Dorozhkin, Pis'ma Zh. Éksp. Teor. Fiz. **77**, 681 (2003) [JETP Lett. **77**, 577 (2003)].
6. I. V. Kukushkin, M. Yu. Akimov, J. H. Smet, *et al.*, Phys. Rev. Lett. **92**, 236803 (2004).
7. C. L. Yang, J. Zhang, R. R. Du, *et al.*, Phys. Rev. Lett. **89**, 076801 (2002).
8. A. C. Durst, S. Sachdev, N. Read, *et al.*, Phys. Rev. Lett. **91**, 086803 (2003).
9. A. V. Andreev, I. L. Aleiner, and A. J. Millis, Phys. Rev. Lett. **91**, 056803 (2003).
10. I. A. Dmitriev, A. D. Mirlin, and D. G. Polyakov, Phys. Rev. Lett. **91**, 226802 (2003).
11. V. Ryzhii, A. Chaplik, and R. Suris, Pis'ma Zh. Éksp. Teor. Fiz. **80**, 412 (2004) [JETP Lett. **80**, 363 (2004)].
12. J. P. Robinson, M. P. Kennett, N. R. Cooper, and V. I. Fal'ko, Phys. Rev. Lett. **93**, 036804 (2004).
13. M. G. Vavilov, I. A. Dmitriev, I. L. Aleiner, *et al.*, Phys. Rev. B **70**, 161306(R) (2004).
14. M. G. Vavilov and I. L. Aleiner, Phys. Rev. B **69**, 035303 (2004).
15. É. M. Baskin, L. I. Magarill, and M. V. Éntin, Zh. Éksp. Teor. Fiz. **75**, 723 (1978) [Sov. Phys. JETP **48**, 365 (1978)].
16. K.-J. Friedland, R. Hey, H. Kostial, *et al.*, Phys. Rev. Lett. **77**, 4616 (1996).

Translated by N. Wadhwa

Nonmonotonic Temperature Dependence of the Hall Resistance of a 2D Electron System in Silicon

A. Yu. Kuntsevich[1],*, D. A. Knyazev[1], V. I. Kozub[2], V. M. Pudalov[1], G. Brunthaler[3], and G. Bauer[3]

[1] *Lebedev Physical Institute, Russian Academy of Sciences, Moscow, 119991 Russia*
* e-mail: alexkun@lebedev.ru
[2] *Ioffe Physicotechnical Institute, Russian Academy of Sciences, St. Petersburg, 194021 Russia*
[3] *Institut für Halbleiterphysik, Johannes Kepler Universität, Linz, Austria*
Received March 24, 2005

For a 2D electron system in silicon, the temperature dependence of the Hall resistance $\rho_{xy}(T)$ is measured in a weak magnetic field in the range of temperatures (1–35 K) and carrier concentrations n where the diagonal resistance component exhibits a metallic-type behavior. The temperature dependences $\rho_{xy}(T)$ obtained for different n values are nonmonotonic and have a maximum at $T_{\max} \sim 0.16 T_{\mathrm{F}}$. At lower temperatures $T < T_{\max}$, the change $\delta\rho_{xy}(T)$ in the Hall resistance noticeably exceeds the interaction quantum correction and qualitatively agrees with the semiclassical model, where only the broadening of the Fermi distribution is taken into account. At higher temperatures $T > T_{\max}$, the dependence $\rho_{xy}(T)$ can be qualitatively explained by both the temperature dependence of the scattering time and the thermal activation of carriers from the band of localized states. © 2005 Pleiades Publishing, Inc.

PACS numbers: 71.30.+h, 73.40.Qv

The metallic-type conduction ($d\rho_{xx}/dT > 0$) observed in the high-mobility 2D electron system in silicon has been attracting the interest of researchers for more than ten years, in particular, in connection with the problem of metal–insulator transition in 2D. Several models had been proposed to explain the "metallic" behavior: the temperature-dependent screening of the impurity potential [1], the quantum corrections due to the electron–electron interaction [2], the macroscopic separation of the liquid and solid electron phases [3], etc. Although the aforementioned theories [1–3] differ from each other, all of them provide qualitative or even quantitative explanations for the behavior of $\rho_{xx}(T)$. Therefore, additional experimental data are required for testing these theoretical models. Such data can be obtained from Hall resistance measurements.

In weak magnetic fields, the Hall resistance ρ_{xy} of the 2D system was theoretically investigated in [4–8]. In [4], it was shown that, when $T \longrightarrow 0$, the Hall resistance in the Fermi liquid remains the same as that in the Fermi gas; i.e., the Hall resistance is not renormalized. Zala, Narozhny, and Aleiner [6] have calculated the quantum correction to the Hall resistance due to the electron–electron interaction, $\delta\rho_{xy}$, for arbitrary values of $T\tau$ (hereafter, we assume that $\hbar = 1$ and $k_{\mathrm{B}} = 1$):

$$\frac{\delta\rho_{xy}}{\rho_{xy}} = \frac{e^2(1 + n_t C(F_0^{\sigma}))}{\pi^2 \sigma_D} \ln\left(1 + \frac{11\pi}{192(T\tau)}\right). \quad (1)$$

Here, n_t is the number of the triplet terms $C(F_0^{\sigma})$ ($n_t = 15$ for a two-valley system), which depend on the Fermi-liquid coupling constant F_0^{σ}, and τ is the transport time. The correction is small in the ballistic regime ($T\tau \gg 1$). In the diffusive regime ($T\tau \ll 1$), it is proportional to $\ln(T\tau)$ and coincides with the Altshuler and Aronov result [7]:

$$\frac{\delta\rho_{xy}}{\rho_{xy}} = 2\frac{\delta\rho_{xx}}{\rho_{xx}}. \quad (2)$$

In the framework of the semiclassical screening theory, Das Sarma and Hwang [8] proposed another mechanism to explain the temperature dependence of ρ_{xy}:

$$\rho_{xy} = \frac{H}{nec}\frac{\langle\tau^2\rangle}{\langle\tau\rangle^2}, \quad (3)$$

where the transport time is mainly averaged over an interval of width T around the Fermi energy. To the lowest order in temperature, this ratio is solely determined by the temperature broadening of the Fermi distribution and is expressed as

$$\frac{\langle\tau^2\rangle}{\langle\tau\rangle^2} = 1 + \frac{\pi^2}{3}(T/T_{\mathrm{F}})^2. \quad (4)$$

As the temperature increases, the $\tau(T)$ dependence becomes dominant and gives rise to a nonmonotonic behavior of $\rho_{xy}(T)$. One can see that the temperature
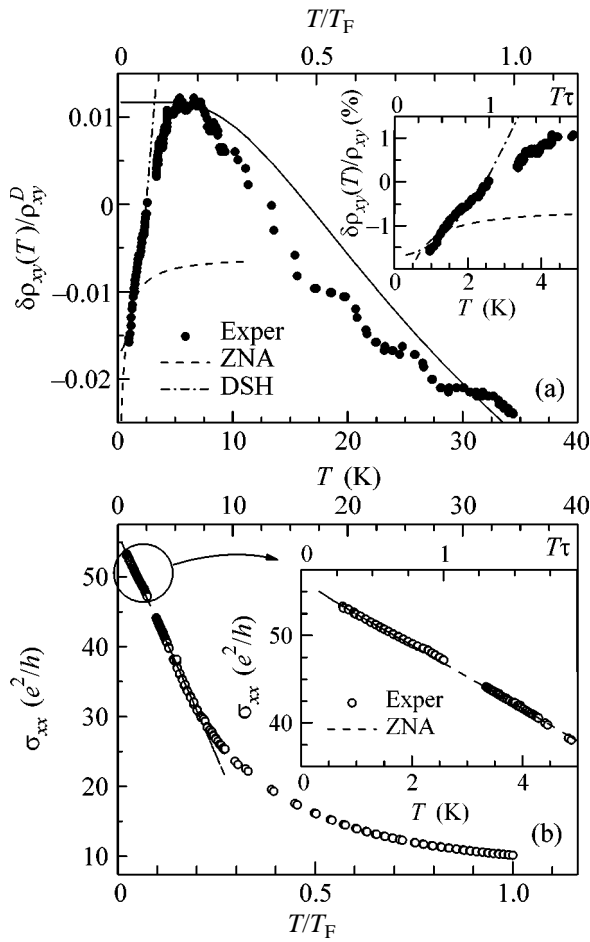
Fig. 1. Temperature dependence of (a) the deviation of the Hall resistance from its classical value and (b) the diagonal conductivity component for the electron concentration $n = 5.7 \times 10^{11}$ cm^{-2}. The insets show the low-temperature parts of the dependences. The dashed, dash–dotted, and solid lines represent the calculated quantum corrections [2], the semiclassical correction according to Eq. (4), and the thermal activation dependence calculated by Eq. (6), respectively.

dependences predicted by the two aforementioned theories [6, 8] for ρ_{xy} are qualitatively different, whereas the $\rho_{xx}(T)$ dependences predicted by these theories agree well with each other and with experimental data [9, 10]. It should be noted that the quantum and semiclassical contributions to the Hall resistance do not exclude each other and, presumably, should simultaneously be taken into account.

In this paper, we present the results of measuring the temperature dependence of the Hall resistance in a weak magnetic field and compare our experimental data with the two theories [6, 8]. The resistance tensor components were measured in the temperature range from 1 to 35 K. The sample was a Si-MOS structure of Hall bar geometry with the dimensions of 0.8×5 mm and with a peak electron mobility of $\approx 25\,000$ cm^2/(V s) at $T = 0.3$ K. The magnetic field $B = 0.1$ T oriented nor-

mally to the 2D plane was sufficiently high to measure the Hall voltage. On the other hand, this field was sufficiently low to satisfy the inequality $\omega_c\tau \ll 1$ (in our experiments, $\omega_c\tau \leq 0.05$ for all the measurements) required for the applicability of the theories under consideration [6, 8] and for the suppression of the Shubnikov–de Haas (SdH) oscillations.

The measurements were performed with an ac current $I_x = 20$ nA at a frequency of 7.6 Hz by using a lock-in amplifier detecting both real and imaginary components of the signal. The Hall voltage V_y was measured for two opposite field directions. The results were averaged to eliminate the admixture of ρ_{xx} to ρ_{xy}. At temperatures $T < 1$ K, the quantities $\rho_{xy}(B)$ and $|\rho_{xy}(-B)|$ became noticeably different and a noticeable imaginary component appeared in V_y. Therefore, we analyzed only the data for temperatures $T > 1$ K. The experiment was carried out as follows: for each of the field directions, the sample was slowly heated while the gate voltage V_g (and, hence, the electron concentration n) periodically varied in a stepwise manner. For each value of V_g, the voltages V_x and V_y were measured. Since the modulation frequency was low and the signal was small, a large signal averaging time was necessary. Therefore, the measurement cycle lasted approximately 16 h.

Figures 1 and 2 show the Hall resistance variation $\delta\rho_{xy}$ and the diagonal conductivity component as functions of temperature for electron concentrations of 5.7×10^{11} and 11.7×10^{11} cm^{-2}, respectively. The variation of the Hall resistance was calculated with respect to its classical value $H/n_{SdH}ec$, where n_{SdH} was determined from the SdH oscillation frequency in the temperature range $T = 0.5–2$ K. The temperature dependence of $\delta\rho_{xy}$ exhibits a pronounced maximum, which moves toward higher temperatures as the electron density increases. The maximum variation of ρ_{xy} is 1–3%. By contrast, σ_{xx} decreases monotonically by a factor of 5 in the same temperature range. The low-frequency part of the $\sigma_{xx}(T)$ curve quantitatively agrees with the quantum interaction corrections [2] without any adjustable parameters [10] (see the dashed lines in Figs. 1b and 2b). The calculations were performed with $m^*(n)$ and $F_0^\sigma(n)$ taken from [11].

Low-temperature region ($T \ll T_F$, $T\tau \lesssim 1$). The quantum correction to ρ_{xy} was calculated by Eq. (1) with the same values of m^* and F_0^σ (the dashed lines in Figs. 1a and 2a). It appears to be an order of magnitude smaller than the experimentally measured dependence; moreover, it disagrees qualitatively with the latter. At the same time, the semiclassical correction given by Eq. (4) and represented in Figs. 1a and 2a by the dash–dotted lines agrees well with the low-temperature part of the dependence $\delta\rho_{xy}(T)$. The latter agreement points to the predominance of semiclassical effects over the quantum ones in the behavior of $\rho_{xy}(T)$ at temperatures
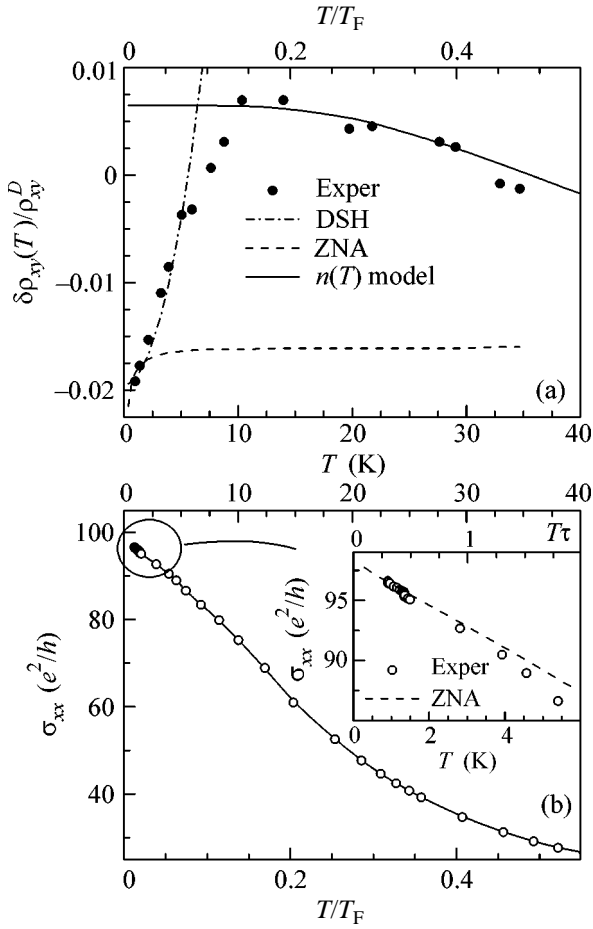
Fig. 2. Temperature dependence of (a) $\delta\rho_{xy}$ and (b) σ_{xx} for the electron concentration $n = 11.7 \times 10^{11}$ cm^{-2}. The inset shows the low-temperature parts of the dependences. The dashed, dash–dotted, and solid lines represent the calculated quantum corrections [2], the semiclassical correction according to Eq. (4), and the thermal activation dependence calculated by Eq. (6), respectively.
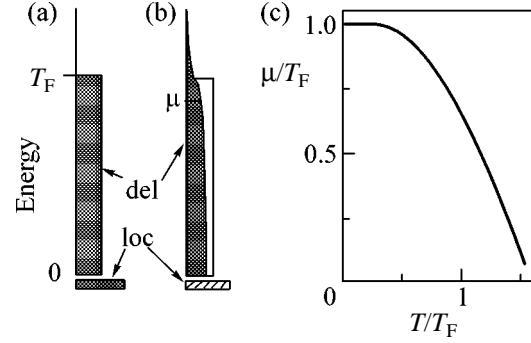

Fig. 3. Schematic representation of the thermal activation process for the model with (del) delocalized and (loc) localized bands. Energy distribution of electrons at (a) $T = 0$ and (b) $T \sim T_F$. The hatched area represents the partially filled band of localized states, and the shadowed areas represent the completely filled band. (c) Temperature dependence of the chemical potential.

$T > 1$ K. Note that, to achieve a better agreement with experimental data, both theoretical curves were arbitrarily shifted in the vertical direction. This is permissible, because the absolute value of the electron concentration was determined from the SdH oscillations with an accuracy of ~1–2%.

High-temperature region ($T \gtrsim 0.3T_F$, $T\tau \gg 1$). In the high-temperature region, the measured $\rho_{xy}(T)$ value decreases with increasing temperature. The quantum corrections [2] are negligibly small, which means that the observed effect is likely to be of semiclassical origin. A similar descending $\rho_{xy}(T)$ dependence was earlier observed for the 2D electron system in Si [12] and for the 2D hole system in GaAs [13, 14]. This effect was qualitatively explained in [8] on the basis of Eq. (3) by a numerical calculation of the temperature dependence of τ for a specific p-GaAs sample. It is possible that this mechanism also contributes to the $\rho_{xy}(T)$

observed for our 2D system. However, the corresponding calculation requires the use of the microscopic parameters of potential fluctuations, which are poorly known and, hence, should be used as adjustable parameters.

At high temperatures, $T \sim T_F$, another mechanism governing the dependence $\rho_{xy}(T)$ may come into play if the system contains localized electrons in addition to the delocalized ones. In such a "two-band" model, the total electron concentration n_{tot} in the system is only determined by the gate voltage and is temperature independent, while the concentration of delocalized carriers depends on temperature because of the thermal activation from the band of localized states. As the temperature increases, the number of free electrons grows and, hence, the Hall resistance decreases.

Let us consider a simple quantitative model of this phenomenon, which is schematically represented in Fig. 3. Let the electron system consist of the Fermi gas of delocalized electrons and a tail of localized states [15, 16]. The latter is characterized by the density of states $n_{loc}^0 \, \delta(\varepsilon)$ and is located near the bottom of the conduction band. The total number of electrons should be constant:

$$n_{tot} = \frac{n_{loc}^0}{1 + e^{-\mu/T}} + \frac{2m}{\pi}T\ln(1 + e^{\mu/T}), \qquad (5)$$

where μ is the chemical potential and the energy is measured with respect to the bottom of the conduction band. Only delocalized electrons contribute to the Hall resistance, and their concentration is expressed as

$$n_{del} = n_{tot} - \frac{n_{loc}^0}{1 + e^{-\mu/T}}. \qquad (6)$$

Thus, in the framework of the simple model under consideration, three parameters, namely, m, n_{tot}, and n_{loc}^0, determine the temperature dependence of μ and, hence, the dependence $\rho_{xy}(T) = H/n_{del}ec$. The first two parameters can be determined independently, and the third is an adjustable parameter. In the range of electron concentrations under study $n > 4 \times 10^{11}$ cm^{-2}, the renormalization of the effective mass is insignificant [11]. Therefore, the calculations were performed with the bare band mass $m = 0.205m_e$. Since the variations of ρ_{xy} are small (see Figs. 1a and 2a), we have $n_{tot} \approx n_{SdH}$ to a good accuracy. The single adjustable parameter n_{loc} was chosen to be concentration-independent for simplicity.

As a result of fitting, we found $n_{loc}^0 = 0.7 \times 10^{11}$ cm^{-2}, which provides a good agreement of the model with the high-temperature parts of the dependences $\rho_{xy}(T)$ obtained for different concentrations (see Figs. 1a and 2a). The calculated dependences shown in Figs. 1a and 2a are shifted vertically by 1–2% to achieve better agreement with the experiment, as in the case of the above comparison with the theories [2, 8]. It should be emphasized that, for our system, n_{loc}^0 is approximately equal to $0.5n_c$, where $n_c = 1 \times 10^{11}$ cm^{-2} is the carrier concentration at which the metal–insulator transition occurs at $B = 0$ [17]. This is in qualitative agreement with the model taking into account the contribution of the band of localized states [16] and with the "few electrons per ion scenario" of the metal–insulator transition [18]. Indeed, when the electron concentration in the 2D system increases, delocalized electrons can appear only after the nonlinear screening of the random potential by the electrons localized in the potential wells.

Thus, in our experiments, we observed a weak (~2%) nonmonotonic temperature dependence of the Hall resistance of the 2D electron system in silicon with a maximum at $T_{max} \approx (0.15–0.2)T_F$. In the same range of temperatures and concentrations, the diagonal conductivity component exhibits a strong monotonic temperature dependence of the metallic type. In the low-temperature region ($T < T_{max}$), the behavior of $\rho_{xy}(T)$ is in better agreement with the simple semiclassical dependence [8] (to the lowest order in temperature, ($\propto(T/T_F)^2$) than with the interaction quantum corrections [6]. This suggests that the temperatures in the range under study ($T\tau > 0.3$) too high to observe the quantum corrections. For the high-temperature region ($T > T_{max}$), the dependence $\rho_{xy}(T)$ can be explained by both the temperature-dependent screening of impurities [8] and the thermal activation of localized electrons to the conduction band. Generally speaking, all of the models considered above can simultaneously contrib-

ute to the Hall resistance. Finally, we note that, if the above-estimated number of localized states is retained down to low concentrations, the localized states can play a significant role in the metal–insulator transition.

REFERENCES

1. A. Gold and V. T. Dolgopolov, Phys. Rev. B **33**, 1076 (1986).
2. G. Zala, B. N. Narozhny, and I. L. Aleiner, Phys. Rev. B **64**, 214204 (2001).
3. B. Spivak, Phys. Rev. B **67**, 125205 (2003).
4. M. Khodas and A. M. Finkel'stein, Phys. Rev. B **68**, 155114 (2003).
5. I. V. Gornyi and A. D. Mirlin, Phys. Rev. B **69**, 045313 (2004).
6. G. Zala, B. N. Narozhny, and I. L. Aleiner, Phys. Rev. B **64**, 201201 (2001).
7. B. L. Altshuler, D. Khmel'nitzkii, A. I. Larkin, and P. A. Lee, Phys. Rev. B **22**, 5142 (1980).
8. S. Das Sarma and E. H. Hwang, cond-mat/0412670.
9. S. Das Sarma and E. H. Hwang, Phys. Rev. B **69**, 195305 (2004).
10. V. M. Pudalov, M. E. Gershenson, H. Kojima, *et al.*, Phys. Rev. Lett. **91**, 126403 (2003).
11. V. M. Pudalov, M. E. Gershenson, N. Butch, *et al.*, Phys. Rev. Lett. **88**, 196404 (2002).
12. V. M. Pudalov, G. Brunthaler, A. Prinz, and G. Bauer, Pis'ma Zh. Éksp. Teor. Fiz. **70**, 48 (1999) [JETP Lett. **70**, 48 (1999)].
13. X. P. A. Gao, G. S. Boebinger, A. P. Mills, Jr., *et al.*, Phys. Rev. Lett. **93**, 256402 (2004).
14. C. E. Yasin, T. L. Sobey, A. P. Micolich, *et al.*, cond-mat/0403411.
15. N. F. Mott, *Metal–Insulator Transitions* (Taylor and Fransic, London, 1974; Nauka, Moscow, 1979).
16. V. I. Kozub and N. V. Agrinskaya, Phys. Rev. B **64**, 245103 (2001).
17. S. V. Kravchenko, G. V. Kravchenko, J. E. Furneaux, *et al.*, Phys. Rev. B **50**, 8039 (1994).
18. T. M. Klapwijk and S. Das Sarma, Solid State Commun. B **110**, 581 (1999).

Translated by E. Golyamina

Erratum: "Refraction of Autowaves: Tangent Rule" [*JETP Lett*. 80, 721 (2004)]

O. A. Mornev

1. The correct zip code in the address is 142290.

2. On p. 723, left column, lines 33–37 from the top. The last two sentences before Eq. (7) should read as follows: "The angles φ_1 and φ_2 between the vectors $(\nabla u)_1$ and $(\nabla u)_2$, respectively, and the Ox axis are related to the angles ψ and ψ_2 between the vectors (∇u) and $(\nabla u)_2$, respectively, and the Oy axis as $\psi_i = \varphi_i - 3\pi/2$ ($i = 1, 2$). It is easily seen in Fig. 3 that."